

Optimally stiffened thin shell structures in 3D printing

ANZONG ZHENG

A thesis submitted in partial fulfilment of the requirements of
Bournemouth University for the degree of

Doctor of Philosophy



National Centre for Computer Animation
Bournemouth University

March, 2019

Copyright

This copy of the thesis has been supplied on condition that anyone who consults it is understood to recognise that its copyright rests with its author and due acknowledgement must always be made of the use of any material contained in, or derived from, this thesis.

Declaration

This thesis has been created by myself and has not been submitted in any previous application for any degree. The work in this thesis has been undertaken by myself except where otherwise stated.

Acknowledgement

I would like to first thank Professor Lihua You and Professor Jianjun Zhang for giving me their invaluable advices, time and kind support at every stage of this work. Completing the research is inseparable from their tireless instructions and help. I would also like to thank Bournemouth University and the National Centre for Computer Animation (NCCA) for providing me with a great research environment, Ms. Sunny Choi and Ms. Jan Lewis for their help with all non-academic matters. I would also like to thank all my colleagues for their help and company, which made my research at NCCA more memorable.

This research is supported by grants of Bournemouth University's match-funded PhD studentship. I have developed skills in optimization, mesh processing and 3D printing during a five month visiting research at Graphics & Geometric Computing Laboratory, University of Science and Technology of China and following three month Marie Curie IRSES supported secondment (Grand No. 612627) at the State Key Laboratory of Computer Science, Institute of Software, Chinese Academy of Sciences. I also gained the knowledge of PDE based geometric modelling and shape reconstruction from the secondment of two months at Faculty of Computing, University Technology Malaysia financially supported by the project of "Partial differential equation-based geometric modelling, image processing, and shape reconstruction (PDE-GIR)" which was funded by the European Commission.

This thesis is dedicated to my parents who have always supported and encouraged me to undertake my PhD research.

Abstract

Thin shell structures have been widely applied in crafts, art, industry, architecture, aerospace, etc. The dilemma in printing thin shell structures is the balance between material efficiency and structural soundness. The use of more material will produce a more solid and sound structure but it takes more time and material to fabricate. On the contrary, a thinner structure is more economical but the object tends to be more fragile or deformable. Therefore the problem of finding an optimal supporting structure is crucial to save printing material consumption while maintaining mechanical performance.

To solve the problem, some methods have been proposed such as inserting struts, local thickening, skin-frame structure, grid-shell structure and Voronoi structure. However, these techniques either use traditional finite elements or ignore shell contribution. The advantages of attaching stiffeners seamlessly to skin surface are:

- Stiffeners can alleviate interior space compared to insertion of struts or Voronoi structure;
- Stiffeners are less likely to cause stress concentration compared to skin-frame structure which connects frame to skin at nodes;
- The stiffened plate theory takes stiffeners and surface as a coupled system by adding stiffness contribution of stiffener elements to corresponding plate elements which yields more accurate solution;
- The strength or ability to resist bending can be further improved by improving shape of stiffeners.

Inspired by these good properties of stiffeners, the research presents three computational methods to automatically generate optimized layout and size of stiffeners:

First, the research discretizes the input geometry into a triangular mesh. The faces and edges of the mesh are taken as traditional plate and beam elements respectively. The contributions from stiffeners (beams) are assembled to corresponding plate elements and the coupled system is solved to obtain initial stress field. An optimization framework is proposed to use the initial stress field to guide the layout of stiffeners to follow the flow of stress, and to optimize the shape of stiffeners once the layout is fixed. The disadvantage of this approach is that stiffeners need to align with edges and in order to fulfil this requirement the input mesh has to update iteratively during flow process.

To maintain the geometry, the second approach is to formulate the stiffeners using same shape functions from plate elements. This method assembles stiffness contribution from any stiffener within a plate element without re-meshing the triangular mesh. An optimization framework to generate uni- and bi-directional stiffeners using this stiffened element is proposed to reinforce thin shell structures.

The intuitive way of distributing stiffeners equally in space is not the best way to create the supporting structure as it does not follow the stress field.

the third method is therefore presented to utilize stress field to guide the generation of stiffener layout and optimize the cross-sectional shape to achieve the purpose of material saving. 3D printed objects based on these three methods are manufactured to verify the effectiveness of these approaches.

The simulations of all three methods are presented and discussed in separate chapters. The optimized results are printed with 3D printers to verify these methods can be used to generate optimised minimum supporting structures under given conditions.

The research only implements Constant Strain Triangle element to simulate the inplane membrane behaviour which may not best reflect the flow of stress in the object, an improvement is to use Linear Strain Triangle element instead of CST element. During the optimisation of stiffened elements, the width and height of stiffened plate elements are assumed to be constant, which will cause some waste of materials since materials over lower stress areas are not fully used. To overcome this problem, the future work is to use varying cross-sections so that the size of cross-section will follow the flow of stress. Finally, the shape of the stiffened elements is not discussed. There are plenty of other shapes widely applied in Engineering which have good mechanical properties. Therefore a combination of multiple shapes of stiffeners under complex loads should be studied in the future.

Contents

Copyright	i
Declaration	ii
Acknowledgement	iii
Abstract	iv
List of Figures	v
List of Tables	v
References	v
1 Introduction	2
1.1 3D printing	2
1.2 Stiffened shell structures	3
1.3 Motivation	4
1.4 Contribution	5
1.5 Outline	8
2 Related Work	10
2.1 Stiffened plate structure analysis	10
2.1.1 Edge aligned stiffeners	10
2.1.2 Arbitrary-oriented stiffener	13
2.1.3 Rib-shell structures in engineering	16
2.2 3D printing structural analysis	17
2.2.1 FEM based method	17
2.2.2 Geometry based method	26
2.3 Summary	30
3 Finite elements of rib-shell structure	32
3.1 Constant strain triangle element	33
3.1.1 Displacement and shape function	33
3.1.2 Element strain	35

3.1.3	Element stress	36
3.1.4	Element stiffness	36
3.2	Discrete Kirchhoff triangle element	36
3.2.1	Displacement model	37
3.2.2	Stiffness matrix	40
3.2.3	Gauss quadrature	41
3.2.4	Transformation matrix	41
3.2.5	Global element stiffness matrix	44
3.3	Drilling degree	44
3.4	Beam element	45
3.4.1	Displacement model	45
3.4.2	Strain and stress	47
3.4.3	Stiffness matrix	48
3.5	Assembly of Plate and Beam elements	48
3.6	Stress	49
3.6.1	Strength terms	50
3.6.2	Hooke's Law	52
3.6.3	Stiffness Tensor for continuous media	53
3.6.4	Principal stresses	54
3.6.5	Von Mises stress	57
3.7	Failure theories	57
3.7.1	Maximum Shear Stress:	58
3.7.2	Von Mises or Distortion Energy Theory	58
3.8	Common 3D printing material properties	61
3.9	Summary	63
4	Edge stiffened structures	64
4.1	Overview	64
4.2	Pipeline of the edge stiffened optimisation	65
4.3	Rib-shell Structure	66
4.3.1	Rib-shell Structure	66
4.3.2	Rib Network	66
4.3.3	Rib Cross-section	66
4.4	Rib Network Generation	68
4.4.1	Principal Stress Calculation	68
4.4.2	Quad-mesh Extraction	68
4.5	Rib Network Initialization	70
4.6	Rib Network Simplification	71
4.7	Rib Network Optimization	73
4.7.1	Rib Flow Optimization	73
4.8	Cross-Section Optimization	75
4.8.1	Size Optimization	76
4.9	Results	78
4.10	Summary	83

5	Unidirectional and bidirectional stiffened structure	84
5.1	Overview	84
5.2	Stiffener element formulation	85
5.2.1	Stiffness matrix of the stiffener element	85
5.3	Pipeline of the uni- and bi-stiffened optimisation	89
5.3.1	Unidirectional and bidirectional slicing	91
5.3.2	Optimization formulation	91
5.4	Numerical examples and experimental results	92
5.5	3D printed uni- and bi-directional stiffened objects	93
5.6	Summary	97
6	Stress guided stiffened structures	98
6.1	Overview	98
6.2	Pipeline of stress guided stiffener optimisation	99
6.3	Seed generation	100
6.4	Parametrization	101
6.4.1	Conformal Maps	101
6.4.2	Conformality in a Triangulation	101
6.5	Voronoi diagram	102
6.6	Stiffener Extraction	103
6.7	Size optimization	105
6.8	Monte-Carlo simulation	105
6.9	Results	106
6.9.1	Parameter setting	106
6.9.2	Different probability thresholds	106
6.9.3	Monte-Carlo simulations	106
6.10	3D printed stress-guided stiffened objects	107
6.11	Summary	111
7	Conclusion and Future Work	113
7.1	Overview	113
7.2	Edge stiffened structures	113
7.3	Uni- and bi-directional stiffened structures	114
7.4	Stress guided stiffened structures	115

List of Figures

1.1	Rib-skin structures in architecture.	4
1.2	Different types of stiffened structures: unidirectional stiffeners (a), bidirectional stiffeners (b), and arbitrary stiffeners (c)	5
1.3	Rib-skin structures in plant leaf, wing and human body	6
1.4	Single- and double-sided stiffened structures (a) single sided (b) double sided	6
2.1	Three modes of representation	11
2.2	Overview of the steps of the algorithm to find worst-case force distribution by Zhou et al. (2013) (Figure from Zhou et al. (2013))	18
2.3	To reduce the stress in the object (a), Stava et al. (2012) identifies the linear chains of the medial axis with an excessive stress (b). The part of the component that must be thickened is determined by the value of the stress and by the distance of individual vertices from the medial points of the component (c). The thickness of the component together with the stress is used to compute a thickening correction (d) (Figure from Stava et al. (2012)).	20
2.4	The most effective strut to reduce the stress of the object (a). The geodesic curve connecting the strut end points is marked in green and the stress is significantly reduced across the model (c). A strut that prefers the visual impact over efficiency (b) transfers a portion of the stress from the left to the right; however, it accumulates stress at the strut end points (d). (Figure from Stava et al. (2012))	21
2.5	To create a hollowing correction, a distance field on the object's interior using Laplace's equation bounded by the medial points of the hollowed component and the vertices of the mesh (a). March- ing tetrahedrons creates a new triangular mesh that represents the hole (b), and the mesh is simplified and applied to the object (c). (Figure from Stava et al. (2012))	22
2.6	Common frame structures used in architecture. (Figure from Wang et al. (2013))	22

2.7	Overview of the algorithm proposed in Wang et al. (2013). Given an input model (a), an initial frame structure (b) is generated. The algorithm runs alternatively the topology optimization (c) and the geometry optimization (d). The struts in (b), (c), and (d) are shown with colour visualizations of their radii. Note that the frame in (c) is much sparser than that in (b). The frame volumes of (b) and (d) are 3.79×10^4 and $2.875 \times 10^4 mm^3$ respectively. The saving ratio of the frame volume is about 24%. In this example, an external force of $5N$ is loaded vertically downside on top of the model. (Figure from Wang et al. (2013))	23
2.8	Given a 3D shape of a shark and external forces Lu et al. (2014) compute an initial stress map (a) and generate a corresponding interior point distribution (b). The lightest interior can sustain the given stress computed through an optimization process. Two steps of the optimization are shown in (c-d) and an optimal strength-to-weight ratio structure is illustrated in (e). (Figure from Lu et al. (2014))	23
2.9	A segmentation result on bunny model. (a) is the von Mises stress under the external force applied on the head and the bottom is fixed. (b) is the segmentation result. Note that the regions with high stress value (indicated in red) are usually concave and covered by the transitional regions. (Figure from Zhao et al. (2016))	24
2.10	Types of optimal regions in Michell trusses. Blue solid lines and red broken lines represent tension and compression bars, respectively. (Figure from Kwok et al. (2016))	25
2.11	The idea of PSLs based truss structure. (Figure from Kwok et al. (2016))	25
2.12	The flowchart of the PSLs based STO algorithm. (Figure from Kwok et al. (2016))	26
2.13	Overview of the algorithm by Umetani & Schmidt (2013)	27
2.14	(Left) The support polygon for standing models (orange) is chosen as the set of the lowest vertices relative to the gravity direction. The horizontal component of the target centre of mass \mathbf{c}^* , for which we optimize, is the projection of \mathbf{c} onto the “safe region” (green) of the support polygon, defined by the toppling angle γ . We assume that the height of \mathbf{c}^* is equal to that of \mathbf{c} when we define the safe region. (Right) For suspended models the target centre of mass is the selected suspension point. (Figure from Prévost et al. (2013))	28
2.15	The stability optimization alternates between two phases: inner carving and shape deformation. The output is two meshes representing the deformed outer surface \mathcal{M}_O and the inner surface (the boundary of interior voids) \mathcal{M}_I , respectively. (Figure from Prévost et al. (2013))	29

2.16	Multi-layer constructions based on the geometric support structure defined by two parallel meshes \mathcal{M} , \mathcal{M}' at approximately constant distance. On the left, the lower layer of the glass roof is suspended from the upper layer which has a structural function. The right-hand side image shows a rudimentary construction of a glass facade where the closed space between layers has an insulating function. (Figure from Pottmann et al. (2007))	30
2.17	A FEM static analysis of the input surface is performed to obtain a stress tensor field, which is decomposed into a double orthogonal line field (a), an anisotropy scalar field (b) and a density scalar field (c). Then an Anisotropic Centroidal Voronoi Tessellation is built with its elements sized and aligned according to the stress tensor field; this tessellation is optimized for symmetry and regularity of faces. The resulting grid-shell is hex-dominant and it is designed to fulfil the required static properties. (Figure from Pietroni et al. (2014))	31
3.1	In-plane and transverse loads in a plane	33
3.2	Triangular membrane element	34
3.3	Degrees of freedom of triangle element	37
3.4	Transformation matrix in 3D	43
3.5	Unit vectors describing xyz system.	43
3.6	Beam element	45
3.7	Stiffness matrix assembling for a coupled structure.	49
3.8	Basic static response of a specimen under tension	50
3.9	A material being loaded in a) tension, b) compression, c) shear	51
3.10	Hooke's law of spring	52
3.11	Plane stress element in 2D	55
3.12	Principal plane stress	56
3.13	Yield point in uniaxial test	60
4.1	System overview: Given an input surface (a), a dense rib network (b) is generated, followed by a simplification process to remove the ribs with little contributions (c). Then a rib flow optimization is performed to adjust the layout of ribs (d). Finally, the cross-section of ribs is optimized using hyperelliptic T-section (e).	64
4.2	The pipeline of edge stiffened structure optimization	65
4.3	Illustration of the rib-shell structure.	66
4.4	From left to right: curved, circular and tree-like rib elements. The right tree-like rib element consists of eight curved ribs.	67
4.5	Hyperelliptic (a) and right-angled (b) T-section. Colour encodes the von Mises stress. The stress of right-angled T-section in the back is much higher than that of hyperelliptic T-section.	68
4.6	Left: principal stress directions. Right: principal stress directions after smoothing.	69

4.7	Rib network simplification of Guscio. The histogram on the left illustrates the contribution of each rib element. The resultant simplified rib network is coloured in blue. Light orange rib elements are dropped.	73
4.8	Moving directions for rib point with degree 4.	74
4.9	Rib network before (blue) and after (red) rib flow optimization for Guscio (left) and Botanic (right).	75
4.10	Hyperelliptic T-Section attached to a shell with thickness t	77
4.11	Area (blue) and second area moments (red) about orders of right-angled and hyperelliptic T-sections.	79
4.12	Top: distributed loads (gravity). Bottom: concentrated loads (load nodes are marked as red).	79
4.13	Results of Lilium. From (a) to (c): Our result, Voronoi grid-shell (Pietroni et al. 2015) and self-support quad shell (Vouga et al. 2012).	80
4.14	Rib-shell structures generated by our system, including Snail, Neumunster, Aquadom, and Bridge.	81
4.15	Rib-reinforced shell structure (c) generated from input mesh (a). And (b) and (d) are colouring visualizations of von Mises stress for pure shell and rib-reinforced shell, respectively, which cost the same volume of material.	81
4.16	The fabricated shell (a-1) and rib-reinforced shell (b-1) cost about the same amount of materials (19.26g for the former and 19.25g for the latter). When imposing loads at the centre, the pure shell has a displacement of 5.6mm under a 30N load (a-3), while the displacement is 1.2mm for the rib-reinforced shell under a 33N load (b-3). And (a-2) and (b-2) are initial states without load for reference.	82
4.17	Rib-shell structures for kite (b) and leaf (d) models generated by our system, which imitate the things (a and c) in real world to some extent.	83
5.1	System overview. From left to right (a) the stress field on input surface, (b) the geometry is sliced equally, (c) after number and cross-section optimization of stiffeners, the final stress field on the same surface and (d) a cut-away show of the underlying stiffener structure.	84
5.2	Local axis system of the stiffener, placed within the shell element	86
5.3	A stiffened plate showing the reference axis of the stiffener	86
5.4	The pipeline of the uni- and bi-stiffened structure optimization	89
5.5	Unidirectional (a) and bidirectional (b) slicing of geometries	91
5.6	Optimized unidirectional stiffeners from the algorithm	92
5.7	Optimized bidirectional stiffeners from the algorithm	93
5.8	All prints	94
5.9	Unidirectionally stiffened flat Plate.	94
5.10	Bidirectionally stiffened Square.	94

5.11	Unidirectionally stiffened Snail.	95
5.12	Bidirectionally stiffened Botanic.	95
5.13	Unidirectionally stiffened Bridge.	96
5.14	Bidirectionally stiffened Dome.	96
5.15	Bidirectionally stiffened Hemisphere.	96
6.1	Algorithm overview. From left to right: (a) the initial stress field of a pure plate shell structure (b) seeds dispersed randomly on dangerous areas (c) Voronoi diagram in parametric space (d) stiffeners created in 3D space based on 2D Voronoi diagram and (e) final stress field after size optimization of stiffeners	98
6.2	The pipeline of the stress guided stiffener optimization	99
6.3	In a conformal map, the tangent vectors to the iso-u and to the iso-v curves are orthogonal and have the same length. (Figure from Lévy et al. (2002))	101
6.4	Overflow of the generation of Voronoi stiffeners.	102
6.5	Example of cancellous bone. Cancellous bone has fully interconnected porous structure. (Figure from Ishikawa (2010))	103
6.6	Stiffener extraction	104
6.7	Effect of different probability thresholds p^* on the distribution of seeds. From left to right, $p^* = 0$, $p^* = 0.3$ and $p^* = 0.5$	106
6.8	Monte-Carlo simulations of Guscio. The random number generator seeds r_s for each column are: 10, 20 and 30 respectively.	107
6.9	All prints	108
6.10	Stress-guided stiffened Plate.	108
6.11	Stress-guided stiffened Botanic.	108
6.12	Stress-guided stiffened Snail.	109
6.13	Stress-guided stiffened Dome.	109
6.14	Stress-guided stiffened Bridge.	110
6.15	Stress-guided stiffened Hemisphere.	110
6.16	Stress-guided stiffened Guscio.	110
6.17	Stress-guided stiffened Lilium.	111
6.18	Stress-guided stiffened Leaf.	111

List of Tables

3.1	2D Gauss points and weights	42
3.2	Common 3D printing material properties	62
5.1	1D Gauss points and weights	90

Chapter 1

Introduction

1.1 3D printing

Unlike traditional machining techniques, which remove materials by subtractive methods such as cutting or drilling, 3D printing is an additive process of making 3D objects of any shape from a digital model. It was predicted there will be 182 million people involved with 3D printing products in 2019 [Burton et al. \(2017\)](#). 3D food printing, with the benefits of convenience, customization, and cost savings, has been used by food production companies and could come to consumers' kitchens in near future. It will be possible for people to print high-fashion dresses in their homes. Apart from applications in our daily life, 3D printing is widely used for both prototyping and distributed manufacturing with a wide range of applications in architecture, construction, industrial design, automotive, aerospace, military, fashion, footwear, jewellery, eye-wear, education, geographic information systems, food, and many other fields. 3D printers have been used to make many parts for air-planes and jet engines by Boeing and General Electric.

As the 3D printing technology continues to improve and prices continue to fall, desktop 3D printers are becoming more affordable and accessible for personal consumers. It is now possible to produce 3D printed objects with exceptionally high fidelity and precision. However, although the quality of 3D printing has improved, both the time to print and the material costs have remained high. To reduce time and save material consumption, the general approach is to print hollowed objects.

The problem of saving time and material is formulated as a cost minimization. Typical methods for this cost minimization problem can be divided into: hollowing, wall thickness minimization, skin-frame structure and honeycomb-like structure. The hollowing and wall thickness minimization methods can release the internal space of 3D printed objects. However, such pure shell structures are not strong which may break during transportation and use. Although skin-frame and honeycomb-like structures are strong, they occupy the internal space of 3D

printing objects which will be used in many situations. Therefore, how to print 3D objects with minimum cost but good strengths and non-occupied internal space is an unsolved problem.

1.2 Stiffened shell structures

Shell structures, such as aircraft fuselages, boat hulls, and large-span roofs, are lightweight constructions by assembling shell elements. The use of shell elements can achieve high degree of reserved strength and structural integrity, but also greatly release the internal space (Ventsel & Krauthammer 2001). However, the accompanying dilemma of such structures is weakened stiffness and strength when a shell has a large span and/or thin thickness. To overcome the problem, additional supporting structures or stiffeners like pillars (Esterhuizen et al. 2010), scaffoldings (Davis & Block 2011), frames (Wang et al. 2013), or ribs (Lam & Santhikumar 2003), are introduced to improve mechanical performance and reinforce the structural soundness.

Stiffened structures also called rib-skin structures including stiffened shells and stiffened plates(plates and shells are interchangeable in this thesis since the shell structure here refers to large span thin shell structure which will be modelled as plate elements) can be more frequently found in nature and engineering structures. A lot of engineering structures are stiffened to raise strength and rigidity and to reduce material costs. These rib-skin structures include barrels (Figure 1.1a), train station (Figure 1.1b), boat (Figure 1.1c) and architecture (Figure 1.1d).

The use of stiffeners introduces mechanical performances and geometrical properties in several aspects:

- stiffeners don't occupy too much internal space compared with pillars, scaffoldings and frames.
- stiffeners attach to the surface entirely so all parts contribute to supporting the object and while also increasing its stability (Arashmehr et al. 2012, Kang & Chang 2013). While pillars, scaffoldings and frames may cause buckling under different loads, stiffeners are connected to the surface in a face-to-face way instead of a point-to-face way and therefore avoid stress concentrations at nodes.
- stiffeners can have variable cross-sectional shapes which can meet different performance goals (Lam & Santhikumar 2003).

Motivated by excellent performance of stiffening structures in supporting skin, they are introduced to enhance 3D printed objects. However, the design of supporting structures is a complicated and difficult problem even for experienced artists or architectures. The common problems for creating an optimised supporting structure include:

- how many ribs to use,



(a) “Wine barrels at the storage room at Tonelería Nacional, Chile” by Gerard Prins / CC BY-SA 3.0



(b) “Helensburgh Railway station bus stop” by Abesty / CC BY-SA 3.0 / Transformed.



(c) “Thompson canoe with half-ribs and stringers” by Squirrelwhisperer / CC BY-SA 4.0



(d) “Raspberry Island Bandshell” by Bobammertiopsis / CC0 / Transformed.

Figure 1.1: Rib-skin structures in architecture.

- where to place, and
- what’s the optimal cross-section?

To solve above questions, various factors need to be taken into consideration simultaneously like boundary conditions, external loads, material properties, and manufacturing capabilities, which requires knowledge of engineering and structural optimization. All these difficulties form barriers for ordinary users without special knowledge to apply stiffened structures to their own 3D printed objects.

1.3 Motivation

According to the distribution of stiffeners, rib-skin structures can be divided into three categories: unidirectional, bidirectional, and arbitrary. Unidirectional structures are stiffened with stiffeners in one direction (Figure 1.2a). Bidirectional structures are stiffened with stiffeners in two different directions (Figure 1.2b).

Arbitrary structures are stiffened in any directions and stiffeners can be straight or curved (Figure 1.2c).



(a) Interior of Igloo-Shaped Church by Adam Jones / CC BY-SA 3.0



(b) "Glass Tunnel" by George Hodan / CC0



(c) "Ceiling In Church" by Vera Kratochvil / CC0

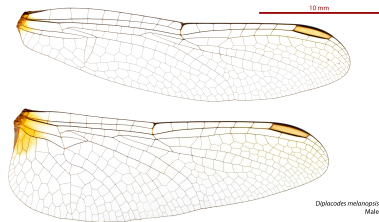
Figure 1.2: Different types of stiffened structures: unidirectional stiffeners (a), bidirectional stiffeners (b), and arbitrary stiffeners (c)

Inspired by biomorphic structures of distributing more material to support critical areas like plant leaf (Figure 1.3a), wing (Figure 1.3b) and human body (Figure 1.3c), the research proposes an automatic way to generate stress guided stiffeners and optimize shapes.

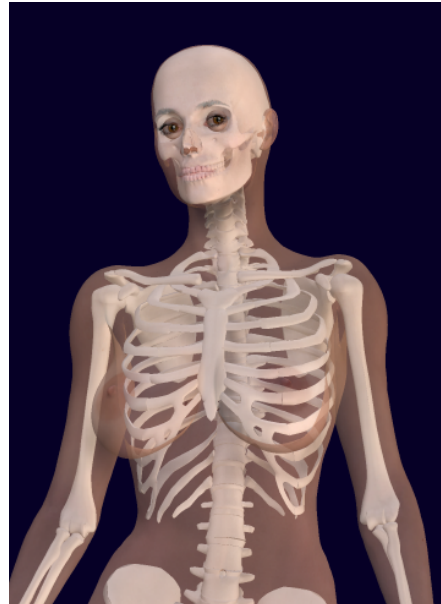
According to whether the skin is stiffened on one side or on both sides, stiffened structures can be divided into single- and double-sided ones. The single-sided (see Figure 1.4a) stiffened structures have all the stiffeners on one side of the skin surfaces. The double-sided (see Figure 1.4b) stiffened structures have the stiffeners on both sides of skin surfaces. Due to the requirement for aesthetics, most 3D printed objects are stiffened on one side. Therefore, only single sided stiffened structures are investigated in the research.



(a) “Victoria cruziana Blattunterseite” by Jojona / CC BY-SA 3.0

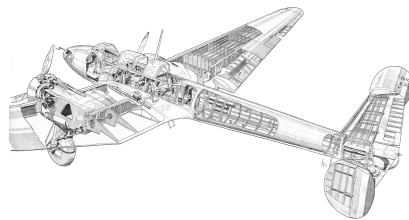


(b) “Diplacodes melanopsis male wings” by John Tann / CC BY 2.0

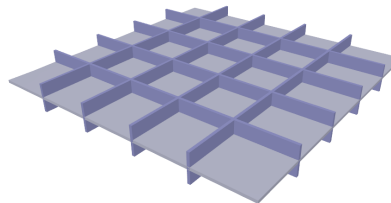


(c) “3D Female Skeleton Anatomy” by Bernhard Ungerer / CC BY-SA 3.0 / Transformed.

Figure 1.3: Rib-skin structures in plant leaf, wing and human body



(a) “Cutaway of the Potez 630” by J. Godefroy / Public Domain



(b)

Figure 1.4: Single- and double-sided stiffened structures (a) single sided (b) double sided

1.4 Contribution

In engineering, most work focuses on the analysis of rib-shell structures, namely the mechanical property of a given layout of ribs (Prusty & Satsangi 2001, Arashmehr et al. 2012). Only a small number of works study the location of ribs on simple surfaces like plates, cylinders, etc (Lam & Santhikumar 2003, Ding et al. 2013). In computer graphics, there are extensive works on the generation and

optimization of triangle-based, quad-based or hex-dominant grid-shell structures (Liu et al. 2011, Cutler & Whiting 2007, Li et al. 2015). They primarily take geometry into account, and only a few consider the static performance (Pietroni et al. 2015, Schiffner & Balzer 2010).

Although there are many existing related works, there is no computational method which construct and optimize rib layout simultaneously on shell structures with arbitrary shape.

Edge stiffener based method

To address the cost minimization problem with structural optimization, a computational pipeline is proposed to design and optimize rib layout on arbitrary surface. The basic idea is to place ribs along the principal stress lines which can maximally reinforce the stiffness of shell (Kwok et al. 2016, Tam, Mueller, Coleman & Fine 2016). The system first generates a dense rib network, followed by a simplification procedure which removes redundant ribs with little contribution. Later a rib flow optimization is introduced to re-adjust the distribution of ribs and a size optimization to achieve certain stiffness requirements with the least amount of material. Finally, the cross-sectional shape of ribs is optimized by using T-section to further reduce material usage while maintaining overall physical properties.

The contributions of this method are summarized as follows.

- a computational pipeline is provided to automatically generate and optimize rib network to reinforce the stiffness and physical performance of shells.
- a rib flow optimization is proposed which takes each rib as a whole and allows ribs flowing on surface, to adjust rib layout and achieve better mechanical performance.

Unidirectional and bidirectional stiffeners based method

In order to maximize the effect of such an introduction, finite element analysis is used to determine stress distribution in stiffened 3D printed objects, and an optimization is formulated to obtain optimized stiffened structures.

This research will lead to the following main contributions.

- A new approach to automatically create optimized stiffened structures of 3D printed objects with maximum strength and minimum material costs;
- Introduction of finite element analysis of stiffened structures into unidirectional, bidirectional and arbitrary stiffened 3D printed objects;
- Integration of finite element calculations into optimization design to formulate the optimal distribution of stiffeners as a min-max problem to minimize material cost and maximize strength of 3D printed objects.

Stress guided stiffener based method

The spatially equally distributed uni-directional and bi-directional stiffeners are straightforward, simple and easy to generate according to geometry dimensions. The disadvantage of the intuitive method is the generated stiffeners may not best follow the flow of the stress field. Additionally, materials distributed over low stresses areas are not efficient since stress in these locations lie far below material strength causing a waste of materials.

To address the above problem, the idea is to spread printing materials precisely at the places need to be strengthened, i.e. critical areas with high stresses.

To generate stress guided stiffeners, a stress field of the input geometry is calculated by finite element analysis. Based on the stress map, seeds are placed randomly on the surface according to the stress map. The input mesh along with 3D seeds are then parametrized to 2D space so that a Voronoi diagram of projected seeds can be computed. The Voronoi diagram is projected back to 3D space and the result is a representation of stiffeners following stress field. Since the initialization of seeds is a random process based on probability, the distribution of seeds might not be the optimal solution. To solve this problem, Monte-Carlo simulation is introduced and iterated a given number of times to cover possible situations and avoid local minimum.

The contributions of this method are summarized as follows.

- Use stress field to guide the distribution of seeds over surface;
- Convert a 3D stiffener generation problem to a problem of finding 2D Voronoi diagram of some seeds;
- Introduce Monte-Carlo simulation to avoid local minimum.

1.5 Outline

Chapter 2 gives a through review of the development of stiffened plate element and up-to-date techniques / methods used in 3D printing to optimise the supporting structures for thin shell objects.

Chapter 3 explains in detail the formulation of classical FEM elements including CST, DKT and Beam elements. All necessary equations to form these elements are given in this chapter including transform matrix, shape function, strain-displacement matrix, stress-strain matrix etc. In order to compensate the rank deficiency of plate element, drilling degree is also introduced. The failure theory which contains the von Mises stress along with 3D printing material properties are also explained in detail to introduce the stress criteria used throughout the dissertation.

Chapter 4 demonstrates the first method proposed in this dissertation to stiffening shell structures using edge aligned stiffeners. The method is based on traditional elements and a technique of rib network flowing is presented in order to distribute materials over critical areas.

Chapter 5 presents the second approach proposed in this thesis to solve the same problem but using a well developed stiffened plate element. Unlike the first approach, this method first calculates the bounding box of the input geometry and then automatically slice the bounding box into different slices to generate stiffeners. After the generation of stiffeners, the cross-section size optimization is formulated as a constrained minimization problem to obtain the optimised supporting structure.

Chapter 6 presents the third method which uses the same element in Chapter 5 but takes into account the stress field, so the generation of stiffeners is guided by the stress. This method first distributes seeds over the surface domain based on the stress map. Then the geometry along with the seeds is parametrized and a Voronoi diagram of the seeds is therefore created. The diagram is then re-projected back to 3D using barycentric coordinates to create the stiffener. The optimisation of stiffener structure is solved in a similar way as proposed in Chapter 5. In order to avoid local minima, Monte-Carlo simulation is introduced and the simulations are repeated a few times to obtain the best optimisation results.

Chapter 7 contains the conclusions of this research and recommendations for future work.

Chapter 2

Related Work

The aim of this research is to strengthen 3D shell objects with minimum printing material under given external conditions. To carry out this research, a thorough literature review on stiffened plate theory and 3D printed structural analysis is studied. The stiffened plate theory section presents a review of the development of the theory over time and the 3D printed structural analysis section is divided into FEM based and geometry based methods.

2.1 Stiffened plate structure analysis

Stiffened plate structures are very common in daily engineering, and are indispensable in aerospace and ship-building disciplines. The wings or fuselage of an aircraft consists of a skin with an array of stiffening stiffeners. The hull of a ship, its deck and super-structure, a road bridge and the launching pedestal of a rocket are only a few examples of stiffened plate structures.

2.1.1 Edge aligned stiffeners

Lumped model

In the lumped model method (Figure 2.1(a)), stiffeners placed within a plate element are shifted to the nodal lines of the plate, i.e. stiffeners are assumed to be concentrated along the nodes of the plate element as bar elements. This model introduces certain inconsistencies. The lumped model is theoretically inaccurate, as the lumped stiffener indicates a coupling along the nodes to which it is connected whereas a stiffener placed within plate element indicates coupling of all the nodes of the element. Secondly, the stiffener inside a plate element is shifted to a new position in the lumped model. It introduces an uncertainty in the accurate evaluation of stiffener stresses and it might also affect the plate stresses. This becomes more evident when analysis is carried out using higher order elements, for which mesh division is coarser and as such greater spacing of stiffeners is required.

Orthotropic plate model

Turner (1956) considered the orthotropic plate model (Figure 2.1(b)) in which the stiffened plate is replaced by a bare plate with orthotropic properties. This model is used efficiently if the stiffeners are small and placed uniformly at close intervals. Equal spacing of stiffeners imposes a limitation on the use of this model and further, the evaluation of the stresses of plate and stiffeners creates additional difficulties.

Fine model

The fine model (Figure 2.1(c)) with exact representation of stiffeners represents stiffeners by bar or beam elements. On the occasions where great accuracy is required the stiffener may itself be modelled using plate or shell elements. In this model the layout of the stiffeners dictates the layout of the finite element mesh. This may be wasteful and inefficient leading to excessively fine meshes in areas of structure not of prime importance. It may also lead to topological difficulties in mesh generation, where the pattern stiffeners are irregular or complex. Clearly, in general the optimal mesh layout may not coincide with the actual pattern of stiffeners.

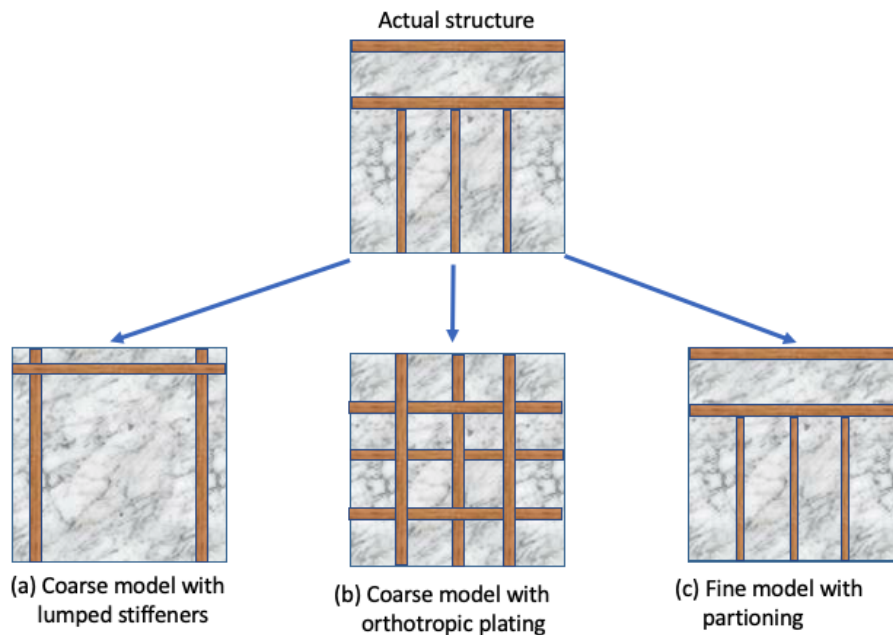


Figure 2.1: Three modes of representation

Grillage model

Another approach is to consider the stiffened plate as a grillage. The comparatively complicated theories for plated grillages, as put forward by [Fraeijs de Veubeke \(1963\)](#) have indicated that good results may be obtained for design work by an unplated grillage calculation, which includes an effective breadth of plating (varying from 50 to 100% of the stiffener spacing) as the flange of the beam. This method of analysis gives deflection normally within 5% and occasionally within 10% and the beam stresses vary generally within 10 to 20% of the experimental values.

Isoparametric quadratic stiffened plate bending element

To improve over existing lumped stiffener and orthotropic plate models, [Mukhopadhyay & Satsangi \(1984\)](#) presented an isoparametric quadratic stiffened plate bending element. Similarly, [Thompson et al. \(1988\)](#) and [Thompson & Bettess \(1991\)](#) presented an 8 noded, eccentrically stiffened plate bending element. The advantage of the element is that the formulation of the element is based in a general manner without disturbing the position or properties of the stiffeners. As the derivation has been based on the isoparametric quadratic element, irregular boundaries and also the transverse shear deformations of the plates and the stiffeners can be very conveniently taken into account. A comparison between this approach and the lumped model verifies the extent of inaccuracy inherent in the latter approach. Many rectangular stiffened plates have been studied and the results were compared with those either theoretically or experimentally available.

High-order four-noded stiffened-plate bending element

The isoparametric element has been the most successful among available elements because of its ability to model a curved boundary successfully. However, the shear-locking problem inherent in the isoparametric element makes it unsuitable for analysing thin plates of arbitrary shapes. To overcome this problem, [Barik & Mukhopadhyay \(2002\)](#) developed a four-noded stiffened-plate bending element for the analysis of bare as well as stiffened plates. This is derived by combining the four-noded rectangular plane-stress element having 8 degrees of freedom with the simplest rectangular plate-bending element having 12 degrees of freedom (commonly known as the ACM Element, after [Adini & Clough \(1960\)](#), [Melosh \(1963\)](#)). The new element has all the advantages of the isoparametric element in modelling an arbitrary plate shape, but without the disadvantage of the shear-locking problem.

Skew stiffener element

To study the large deflection behaviour of stiffened plates, [Srinivasan & Ramachandran \(1977\)](#) presented an analysis for the large deflection of clamped laterally loaded skew plates with stiffeners parallel to the skew directions. The

eccentricity of the stiffeners is taken into account when deriving the governing non-linear differential equations. The solution of the problem is solved by a numerical procedure involving the use of integral equations of beams and the Newton-Raphson method. The impact of variation of skew angle and size of stiffener on the behaviour of the stiffened skew plate has been studied as well.

The stiffened plate is idealized as an equivalent anisotropic bare plate in the formulation. Drawbacks with the idealization are the requirement such as that the stiffeners should be identical, light and equally spaced.

Super-element

Koko & Olson (1991b) used a super-element approach for the large deflection and elastoplastic analysis of orthogonally stiffened plates. The super-elements are designed to contain all the basic modes of deformation so that only one plate element per bay and one beam element per span are needed to analyse a stiffened structure, therefore reducing the storage requirement and solution times. The authors further extended the proposed approach for the non-linear modal and transient analysis of stiffened plates (Koko & Olson 1991a, 1992). The proposed method was limited to the study of isotropic rectangular plates and shells, stiffened in mutually perpendicular directions. Hence the super-element approach is restricted by the condition that the stiffeners must pass through the edges of the super-element.

The limitation of the method is that the formulation is made for rectangular plates only where the stiffeners must pass through nodal lines. The results have indicated overestimation of deflections and underestimation of stresses.

Beam-plate model

An optimal beam-plate model should involve, as explained in Barut et al. (2000), the placement of the beam element within the plate or shell element at an arbitrary orientation. This requires the definition of the displacement fields at any point within a slave element (beam element) in terms of the field variables of a master element (plate or shell element). Since the beam kinematic field is described by the shell kinematic field, only the master plates or shells are needed to discretize the entire stiffened shell structure, thus eliminating the modelling difficulties attributed to the conventional beam-plate and beam-shell models. This approach is referred to as the arbitrary-orientated stiffener approach and has been widely applied for more than two decades to the linear analysis of stiffened plates (Mukhopadhyay & Satsangi 1984, Satsangi & Ray 1998) and stiffened shells (Samanta & Mukhopadhyay 1998, Prusty 2003).

2.1.2 Arbitrary-oriented stiffener

Rao et al. (1993) presented an efficient and accurate finite element static analysis of the large deflection response of isotropic stiffened plates using the isoparametric quadratic stiffened plate bending element. The stiffened element was a

development of the linear formulation presented in [Mukhopadhyay & Satsangi \(1984\)](#). The authors excluded the contribution of the stiffener non-linearities in the formulation. This was later introduced in [Chattopadhyay et al. \(1995\)](#). In this later work, the large deflections of laminated composite stiffened plates were analysed using an eight noded isoparametric element. The element formulation was based on Reissner–Mindlin’s hypothesis with a total Lagrangian description of motion. In both works the arbitrary orientated stiffener approach was applied so that the stiffener may lay within the element, with the limitation that the stiffener ends had to pass through two opposite edges of the element. The presented formulation was not capable of modelling stiffeners of arbitrary cross-section.

The arbitrary-orientated stiffener approach was applied to the geometrically non-linear analysis of stiffened shells in [Goswami & Mukhopadhyay \(1995\)](#). Geometrically non-linear finite element static, modal and transient analyses of laminated composite stiffened shells were carried out using a nine noded Lagrangian curved shear flexible isoparametric stiffened element with five degrees of freedom per node. Again the formulation accounts for arbitrarily orientated stiffeners with the limitation that stiffeners have to pass through two opposite edges of the element. Hence, it is not possible to model stiffeners that are required to pass through two adjacent edges of the shell element.

[Barut et al. \(2000\)](#) recently presented a stiffened shell element formulation for the geometric non-linear analysis of composite laminated stiffened shells. It is a four node, triangular, C_0 anisoparametric element with five degrees of freedom at the corner nodes and two degrees of freedom at the centre node. The formulation accounts for transverse shear deformation and material anisotropy in both the shell and stiffener. The laminated stiffeners may be arbitrary in orientation and cross-section. Although the study discusses the incorporation of arbitrarily shaped and arbitrarily orientated stiffeners, only one example for laminated cross-ply stiffened shell with rectangular stiffeners was covered.

In view of this restriction, [Samanta & Mukhopadhyay \(1999\)](#) presented a formulation for the large deflections of deep isotropic stiffened shells. The analysis was conducted using a combination of Allman’s plane stress triangle and the discrete Kirchhoff triangle plate bending element which was previously used by the authors to solve linear examples of stiffened shells ([Samanta & Mukhopadhyay 1998](#)). The element initially had 24 degrees of freedom which were later reduced to 18 using appropriated constraint equations. The proposed formulation was limited to thin, isotropic plates and shells reinforced with stiffeners of rectangular cross-section only. The element, being faceted, differs slightly from the actual shell and hence the coupling of stretching and bending is excluded from the element due to the absence of element curvature.

For the geometrically non-linear analysis of isotropic and laminated arbitrary orientated stiffened panels, [Ojeda et al. \(2007\)](#) presented an 8 node isoparametric plate element combined with 3 node beam element, using the concept of equal displacements at the plate-stiffener interface. The non-linear formulation has been based on the linear, arbitrarily oriented, stiffener formulation of [Prusty \(2003\)](#) for the analysis of stiffened plates and shells. Arbitrary orientation, eccentricity, and

diverse cross-sectional shapes of the stiffener are taken into account to generate the stiffness matrix of the stiffened element in the geometrically non-linear range.

The modelling of stiffened elements and the mesh generation of 3D curved surfaces are the major difficulties in the adaptive analysis of stiffened shells. The conventional finite element models for the stiffened shells have the shell elements arranged such that the stiffeners are restricted to shell element nodal lines. This restriction causes difficulty in the automatic mesh generation for the adaptive analysis which results in either excessive mesh refinement or severe mesh distortion in order to keep the element mesh layout coincident with the actual pattern of stiffeners.

To overcome this difficulty, [Thompson et al. \(1988\)](#), [Thompson & Bettess \(1991\)](#) developed an integrally stiffened Ahmad shell element which combines a shell element with the stiffener beam elements distributed in the shell element. Because the effects of the stiffener and the associated generalized strains are expressed by using the shell element shape functions and their derivatives, the stiffness contribution of the stiffener is reflected at all the nodes of the shell element, while the stiffener positions and properties remain undisturbed. This allows arbitrary orientation of any number of stiffeners within a shell element.

With advantages of the integrally stiffened shell finite elements, [Li et al. \(1997\)](#) presented an automatic mesh generation of 3D quadrilateral elements. The method for the generation of a quadrilateral element mesh for stiffened shells is combined with a sophisticated error estimate and an effective mesh refinement strategy established at an element level in order to complete the adaptive analysis. The stiffeners in the presented study may be either discrete stiffeners, dense stiffeners or a combination of both discrete and dense stiffeners.

The buckling and vibration characteristics of stiffened plates and shells subjected to initial or dead loads are of considerable importance to mechanical and structural engineers.

[Samanta & Mukhopadhyay \(2004\)](#) developed a general three noded triangular shell element for the analysis of dynamic characteristics of the stiffened structures. The basic shell element employed is a combination of Discrete Kirchhoff's Triangle (DKT) plate bending element ([Gunderson et al. 1969](#)) and Allman's plane stress triangle ([Allman 1984](#)).

Using the technique where stiffeners are modelled by beam finite elements, [Jirousek \(1981\)](#) formulated a 4-node isoparametric beam element including transverse shear and Saint-Venant torsion effects.

Similarly, [Srivastava et al. \(2003\)](#) modelled the plate and the stiffeners as separate elements where the compatibility between these two types of elements is maintained.

In order to attain displacement continuity, a rigid fictitious link is applied to connect one node in the plate element to the beam node sharing the same section. This approach neglects the out-of-plane warping displacements of the beam section and, in such cases, the usual formulation overestimates the stiffener torsional rigidity. To eliminate this problem [Baker & Pavlovic \(1982\)](#) introduced a torsion correction factor. This is analogous to the shear correction factor commonly introduced in the shear deformation beam theory.

Vörös (2007) proposed an efficient procedure modelling the connection between the plate/shell and the stiffener, and as part of it the constraint torsion effect in the stiffener. In structural modelling, the plate and stiffener are treated as separate finite elements where the displacement compatibility transformation takes into account the torsion-flexural coupling in the stiffener and the eccentricity of internal (contact) forces between the beam-plate/shell parts. The development of the stiffener is based on a general beam theory, which includes the constraint torsional warping effect and the second order terms of finite rotations.

Nguyen-Thoi et al. (2013) presented a new method to analyse eccentrically stiffened plates by the cell based smoothed discrete shear gap method (CS-FEM-DSG3) using triangular elements. In the method, the original plate element CS-DSG3 is combined with a membrane element and stiffened by a thick beam element. The eccentricity between the plate and the beam is included in the formulation of the beam. And the compatibility of deflection and rotations of stiffeners and plate is assumed at the contact positions.

As a potential aerospace structural concept, hierarchical stiffened plates under axial compression are characterized by multiple local features. To demonstrate the higher lightweight potential of hierarchical stiffened shells compared to traditional ones, Hao et al. (2014) presented a hybrid minimum-weight optimization formulation for the hierarchical stiffened shells based on Smearred Stiffener Method. The hybrid optimization framework of hierarchical stiffened shells includes imperfection sensitivity analysis, and has the advantage of combining the efficiency of SSM with the accuracy of FEM. Unlike Hao’s approach, Wang et al. (2015) takes the skin and minor stiffeners as an unstiffened anisotropic plate based on a novel numerical implementation of asymptotic homogenization method. Then the equivalent plate together with major stiffeners are treated as a hybrid model which can be calculated by FEM.

To guide the practical design method for stiffening thin steel plate shear walls, Alinia & Shirazi (2009) presented a numerical investigation on one-sided transverse and longitudinal flat stiffeners located in various arrangements on shear plates which effectively divide the plate into sub-panels. The results obtained from several non-linear static analyses providing applicable and empirical relationships for evaluating optimal dimensions of stiffeners.

Unlike the conventional topology optimization methods characterized by “subtraction mode”, Li et al. (2013) presented a simple and practical multi-discipline topology optimization method to produce the stiffener layout for plate/shell structures based on the observation of the natural morphogenesis of leaf veins. The “addition mode” method simulates the emergence of complex branching patterns copying the self-optimization of leaf veins which always try to grow into a configuration with global optimal performances.

2.1.3 Rib-shell structures in engineering

There are lots of researches on rib-stiffened shell structures in engineering. Most works focus on the analysis of a given rib-shell structure Johannes (1958), Prusty & Satsangi (2001), Arashmehr et al. (2012), Kang & Chang (2013), namely

investigating the stiffening effect of ribs on a certain surface under given external loads. Others consider the optimization of size, shape or location of ribs on surface to enhance the performance of total structure [Liu & Shimoda \(2014\)](#), [Wang et al. \(2017\)](#), [Ansola et al. \(2004\)](#). And only a few works study the design of ribs on given shells. [Lam & Santhikumar \(2003\)](#) introduced an automatic method to place ribs on surface by optimizing the thickness of shell first, then put ribs on the surface where the thickness is smaller than a given threshold value. Another method to design ribs is the so-called adaptive growth technique. Stiffeners start from the seed points, grow and branch off towards direction with the maximal effectiveness of the global mechanical performance, which is dependent on the design sensitivity of the current structure ([Ding et al. 2013](#), [Ji et al. 2014](#)). [Szczepanik & Burczyński \(2012\)](#) proposed to use particle swarm algorithm to optimize rib locations. Almost all of these works only discussed some very simple surfaces. For an arbitrary 3D freeform surface, the design of rib-shell structure is still a tough job.

2.2 3D printing structural analysis

2.2.1 FEM based method

The 3D printing has rapidly expanded in the past couple of years. Now, it is possible to produce 3D printed objects with high fidelity and precision. In spite of improved quality, there is no guarantee of the structural soundness of 3D printed objects.

There are a number of reasons why a 3D model cannot be manufactured or is likely to fail:

- the dimensions of thin features (walls, cylinder-like features, etc) are too small for the printing process, resulting in shape fragmentation at the printing stage;
- the strength of the shape is not high enough to withstand gravity, at one of the stages of the printing process;
- the printed shape is likely to be damaged during routine handling during the printing process or shipment;
- the shape breaks during routine use.

The first automatic method devised to detect structural issues of printed objects was proposed in [Telea & Jalba \(2011\)](#). The method detects thin and thick parts and then uses a set of basic geometric rules to determine whether a given thin part can support its attached parts. Although the method detects some problematic cases, it lacks the structural analysis component necessary to accurately approximate stress in more complex topological forms. Furthermore, this work does not address the fundamental goal of correcting the detected

structural issues. Even in the presence of perfect analysis, it may not be obvious or easy for the user to know where to start making corrections.

For the problem of determining the easiest (in terms of minimal applied force) ways to break it or severely deform it with given shape of an object and its material properties, Zhou et al. (2013) presented a framework (shown in Figure 2.2) approximating the solution that would identify structural problems without specific assumptions on loads and manual load set-up.

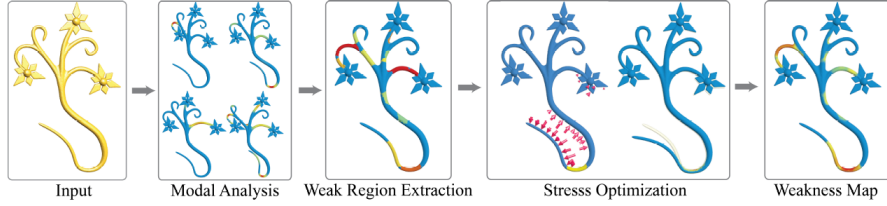


Figure 2.2: Overview of the steps of the algorithm to find worst-case force distribution by Zhou et al. (2013) (Figure from Zhou et al. (2013))

The problem is formulated as finding the worst-case force distribution satisfying the constraints of the model and optimizing this objective function, which has the form of

$$\begin{aligned}
 & \max_{\Omega} \max_{i=1,2,3} |\sigma_i| \rightarrow \max; \\
 & Lu = 0 \text{ on } \Omega, C : (\nabla u + \nabla u^T) n = pn \text{ on } \partial\Omega \\
 & \int_{\partial\Omega} p n dA = 0, \int_{\partial\Omega} p n \times (x - x_c) dA = 0, \\
 & \int_{\Omega} u dV = 0, \int_{\Omega} u \times (x - x_c) dV = 0, \\
 & 0 \leq p \leq p_{max} \text{ on } \partial\Omega, \int_{\partial\Omega} p dA = F_{tot}
 \end{aligned} \tag{2.2.1}$$

where maximal principal stress $\max_{\Omega} \max_{i=1,2,3} |\sigma_i|$ is a commonly used measure of interest, with σ_i eigenvalues of the stress tensor.

The solution of the problem in Equation 2.2.1 can be obtained by solving a sequence of problems in which the objective function $\max |\sigma_i|^2$ is maximized for every point and then taking the maximum of all results. Due to non-linearities and non-convexity, any optimization is likely to get stuck in local minima.

To efficiently approximate the algorithm, Zhou et al. (2013) incorporated modal analysis which they used to restrict the part of the object where they need to maximize the stress or another functional. Meanwhile, the problem in Equation 2.2.1 is replaced with a functional that can be optimized efficiently and that is minimized by a similar pressure distribution, p , to the original.

The final formulation is as follows:

$$\begin{aligned}
& \int w \operatorname{tr} \sigma dV \rightarrow \max \text{ w.r.t. } u \text{ and } p; \\
& Lu = 0 \text{ on } \Omega, C : (\nabla u + \nabla u^T) n = pn \text{ on } \partial\Omega \\
& \int_{\partial\Omega} = pndA = 0, \int_{\partial\Omega} pn \times (x - x_c) dA = 0, \\
& 0 \leq p \leq p_{\max} \text{ on } \partial\Omega, \int_{\partial\Omega} pdA = F_{tot}
\end{aligned} \tag{2.2.2}$$

Stava et al. (2012) proposed a first step in the direction of physically based automatic solutions for the detection and correction of major structural problems in 3D models before they are printed, while attempting to minimally alter their appearance. They first detect major printability issues of the input model through printability assessments. Then they correct the model by using three different approaches: local thickening, strut adding, and hollowing. Local thickening increases the strength of the object’s thin parts, and it preserves the form and the surface detail of the object. Struts can be inserted to prevent non-rigid deformations of the object, and they are automatically placed at locations that are least visible to the user. Hollowing eliminates material inside the object, reducing the weight of certain parts to alleviate the stress at other locations.

Local thickening The goal of local thickening is to identify and fix the problematic thin parts of the model. To determine which part of the mesh should be considered a thin component, the value of stress needs to be taken into account. When the stress is high, larger parts of model require thickening than when the stress is less. In Stava et al. (2012) they used combined information about stress and about the local thickness and topology that is stored on the computed interior medial axis.

The target thickness t_d is determined by

$$t_d = t_m \sqrt[3]{\sigma_m / \sigma_c} \tag{2.2.3}$$

and the threshold thickness t_t that separates the thin part from the thick parts is defined as $t_t = c_t t_d$, where c_t is a predefined constant, t_m is the local thickness associated with the medial point, σ_m is the maximal stress and σ_c is the allowed critical value.

Adding struts The local thickening can be effectively used to solve many of the structural problems of the printed objects, but in certain cases, the thin components that causes the printability issues are essential for the object’s visual style. When they are noticeably thicker, the objects might be visually altered too much.

For the purpose of reducing material cost in printing a given 3D object, Wang et al. (2013) presented an automatic solution to minimize material cost of the object in 3D fabrication. The key idea is to ‘hollow’ the object by creating a light weight frame structure (see Figure 2.6). The frame structures benefit from two aspects:

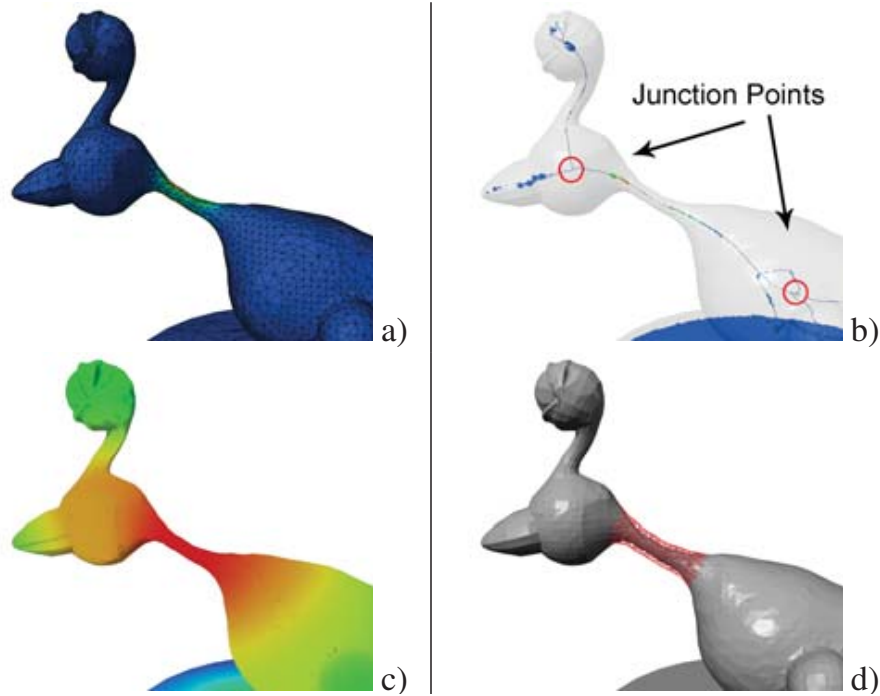


Figure 2.3: To reduce the stress in the object (a), [Stava et al. \(2012\)](#) identifies the linear chains of the medial axis with an excessive stress (b). The part of the component that must be thickened is determined by the value of the stress and by the distance of individual vertices from the medial points of the component (c). The thickness of the component together with the stress is used to compute a thickening correction (d) (Figure from [Stava et al. \(2012\)](#)).

- the mass of object could be significantly reduced through the use of frame structures while maintaining its strength and stiffness ([Gibson & Ashby 1999](#));
- frame structures provide sufficient flexibility and variability, which make them possible to meet a variety of constraints in 3D printing.

Two main factors are considered in the paper: frame volume and structure redundancy which makes the problem a multi-objective programming formulation. As it is very difficult to construct an appropriate weight to trade off the two objectives, the problem is formulated as a multi-objective programming (MOP) problem:

$$\min_{\mathbf{r}, \mathbf{V}_{int}, E_{int}} \text{Vol}(\mathbf{r}, \mathbf{V}, \mathbf{E}) \ \& \ \|E_{int}\| \quad (2.2.4)$$

where the frame volume $\text{Vol}(\mathbf{r}, \mathbf{V}, \mathbf{E})$ has higher priority over the number of internal struts $\|E_{int}\|$.

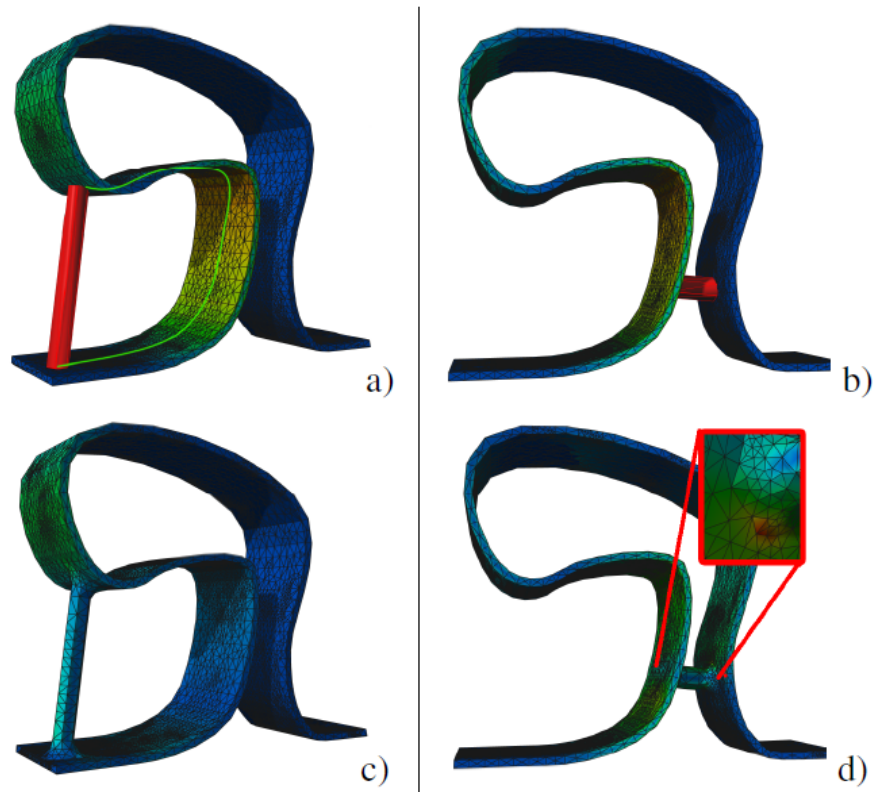


Figure 2.4: The most effective strut to reduce the stress of the object (a). The geodesic curve connecting the strut end points is marked in green and the stress is significantly reduced across the model (c). A strut that prefers the visual impact over efficiency (b) transfers a portion of the stress from the left to the right; however, it accumulates stress at the strut end points (d). (Figure from [Stava et al. \(2012\)](#))

The overview of the algorithm is shown in Figure 2.7. Given an input mesh, an initial frame with the radii of its struts is generated from the size optimization. Then the algorithm runs alternatively the topology optimization and geometry optimization until the frame volume does not decrease. The topology optimization eliminates the redundant struts by approximately solving an ℓ_0 sparsity optimization under the frame volume constraint. The geometry optimization refines the positions of internal nodes, the radii of struts, and, to some extent, the topology of a frame structure. Finally, an optimized frame structure with minimum volume is obtained as the final result.

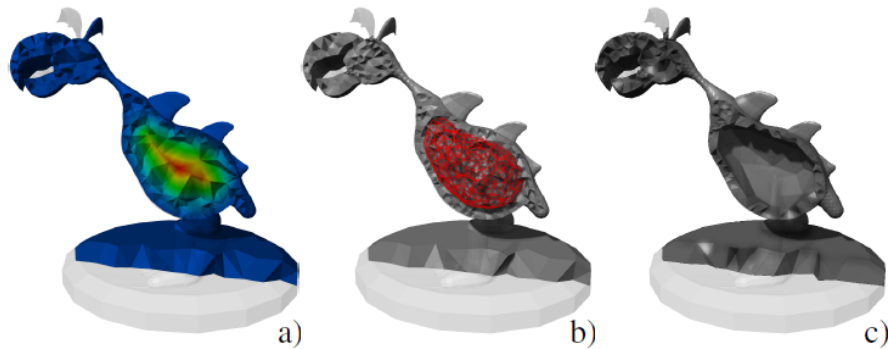


Figure 2.5: To create a hollowing correction, a distance field on the object's interior using Laplace's equation bounded by the medial points of the hollowed component and the vertices of the mesh (a). Marching tetrahedrons creates a new triangular mesh that represents the hole (b), and the mesh is simplified and applied to the object (c). (Figure from [Stava et al. \(2012\)](#))

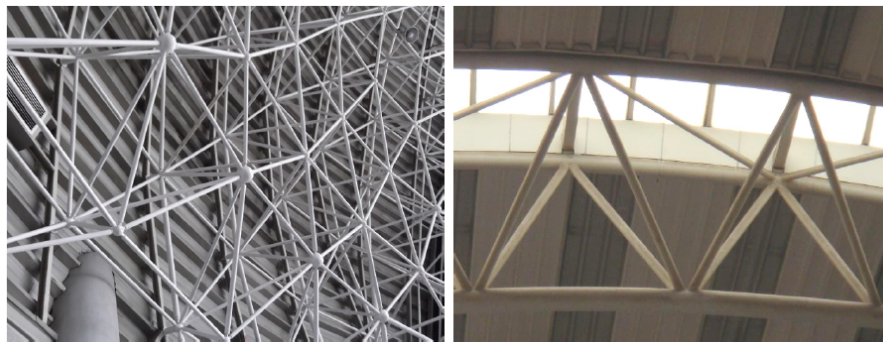


Figure 2.6: Common frame structures used in architecture. (Figure from [Wang et al. \(2013\)](#))

Honeycomb structures are known to be of minimal material cost while providing strength in tension. [Lu et al. \(2014\)](#) introduced a hollowing optimization algorithm based on the concept of honeycomb-cells structure. The honeycomb like cells which define the inner structure is generated by utilizing an adaptive centroidal Voronoi diagram. Given a set of sites, the Voronoi diagram defines a space partitioning into closed-cells of nearest regions with respect to the sites ([Voronoi 1908](#)). As the number of sites increases, Voronoi cells converge to hexagonal honeycomb-like shapes ([Bronstein et al. 2008](#)), producing a structure of high strength-to-weight ratio for any material ([Wilson 1990](#)).

From a given 3D geometry with exterior loads and gravity, the stress map representing stress at each internal point (Figure 2.8 (a)) is computed and treated

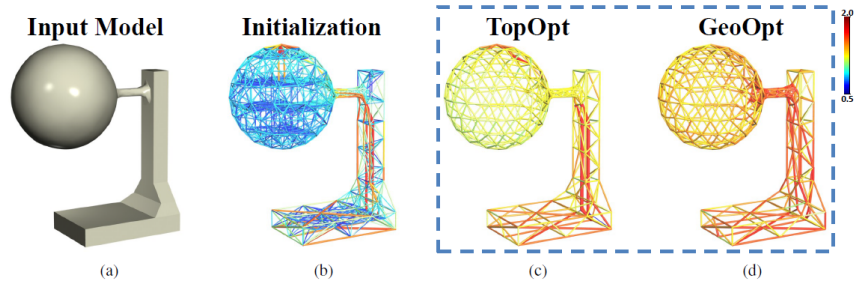


Figure 2.7: Overview of the algorithm proposed in Wang et al. (2013). Given an input model (a), an initial frame structure (b) is generated. The algorithm runs alternatively the topology optimization (c) and the geometry optimization (d). The struts in (b), (c), and (d) are shown with colour visualizations of their radii. Note that the frame in (c) is much sparser than that in (b). The frame volumes of (b) and (d) are 3.79×10^4 and $2.875 \times 10^4 mm^3$ respectively. The saving ratio of the frame volume is about 24%. In this example, an external force of $5N$ is loaded vertically downside on top of the model. (Figure from Wang et al. (2013))

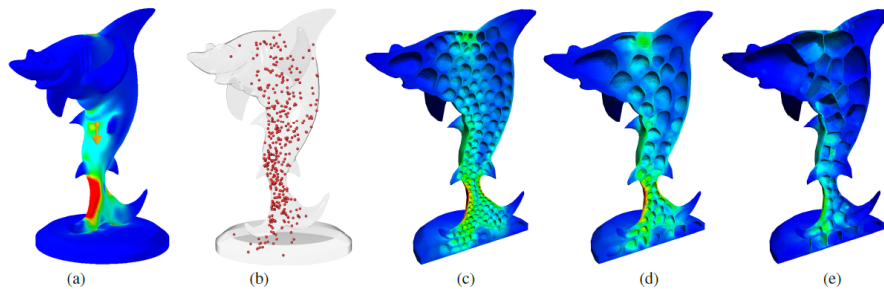


Figure 2.8: Given a 3D shape of a shark and external forces Lu et al. (2014) compute an initial stress map (a) and generate a corresponding interior point distribution (b). The lightest interior can sustain the given stress computed through an optimization process. Two steps of the optimization are shown in (c-d) and an optimal strength-to-weight ratio structure is illustrated in (e). (Figure from Lu et al. (2014))

as a continuous volumetric density map so a locally varying point distribution reflecting the underlying density map (Figure 2.8(b)) can be generated. The object's interior is then partitioned into a set of closed-cells by constructing an adaptive centroidal Voronoi tessellation. The pore is computed by explicitly extracting iso-surface inside a harmonic field within each Voronoi cell and carving out the inner volume (Figure 2.8(c)). Two parameters: the total number of inner cells α and hollowing amount β inside each cell are used to control the construction of the pore-based inner structure.

For geometries with non-closed surfaces, adding support structures, however,

would make the fabricated objects differ from their original designs either visually or functionally. The added support structures can be partially seen or affect how the objects are used. To maintain the user-specified structural stability without additional support structures, [Zhao et al. \(2016\)](#) introduced an approach to fabricate shell objects with optimized thickness parameters. The input surface is first segmented into a number of patches (see [Figure 2.9](#)), and each patch is assigned with a single parameter to significantly reduce the optimization variables so that the total number of design variables in the optimization can be decreased.

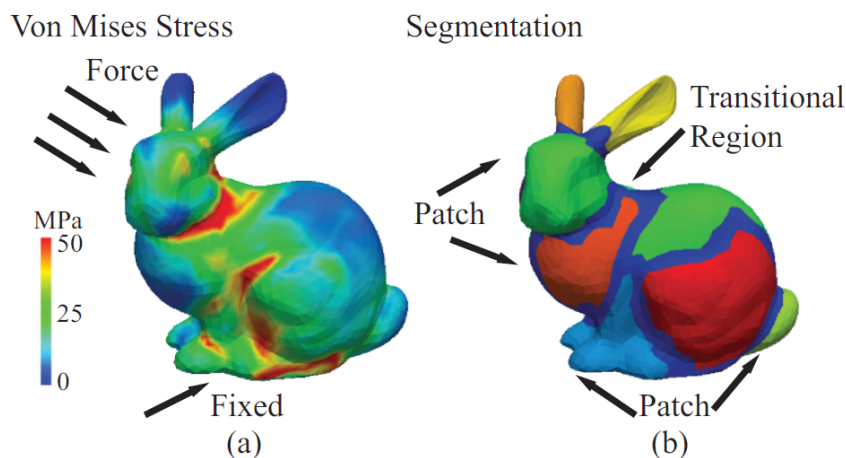


Figure 2.9: A segmentation result on bunny model. (a) is the von Mises stress under the external force applied on the head and the bottom is fixed. (b) is the segmentation result. Note that the regions with high stress value (indicated in red) are usually concave and covered by the transitional regions. (Figure from [Zhao et al. \(2016\)](#))

The Fuzzy cut method presented by [Katz & Tal \(2003\)](#) is adopted here to cut the surface at concave edges and extract convex regions. Another technique sensitivity analysis investigated by [Paris et al. \(2010\)](#), [Arnout et al. \(2012\)](#) is also introduced to compute the derivative of stress with respect to the thickness parameter, and convert the original non-linear optimization problem into sequential linear programming problem. The problem is then solved by an alternating algorithm (AOP) to optimize patch and transitional regional thickness.

Stress lines

Structural Topology Optimization (STO) has been applied to many structural design problems, such as the design of materials and mechanisms to obtain the optimal distribution of material that maximizes the stiffness of the structure (minimize the compliance). A classic problem of the optimum structural design

is due to Michell’s theorem (Michell 1904), in which the lightest frame structure \mathcal{S} of a bounded compliance is to be found to transmit a given load to given supports in a feasible domain Ω (Sokol 2011).

From Michell’s theorem, to find a virtual deformation within design domain, the minimum weight structure needs to satisfy two conditions: the displacements vanish on the supports and the strains distribute along the members of the structure. That means the minimum weight structure should follow the direction of principal stresses (tension or compression) so that no shear stress presents on the structure members (Kwok et al. (2016)).

Principal Stress Lines are pairs of orthogonal curves and are traced in the design domain along the direction of principle stresses, therefore PSLs provide a visualization of the natural force flow in a structure, which shows the lines of desirable material continuity for a given design domain (Adriaenssens et al. 2014). There are some works on structure optimization inspired by principal stress lines. Su et al. (2014) presented an algorithm to generate the grids that are concordant with the force flow. Tam, Mueller, Coleman & Fine (2016) introduced stress line additive manufacturing which can achieve better structural performance. Tam, Coleman, Fine & Mueller (2016) proposed to enhance structural performance by adding stress line to the surfaces. Wu et al. (2017) found that micro-structures of trabecular bone are aligned along the principle stress directions and proposed an approach to generate bone-like porous structures. Kwok et al. (2016) developed a novel structural topology design method to accordingly define the topology and shape of the structures. After the stress and related optimal region analysis, the structural pattern of the local region around the load and supports can be obtained. An example of the classic case of the single-load and two-supports cantilever is shown in Figure 2.10, where the loading point is a T-point and the two fixed supports are S^+ -point and S^- -point, respectively. Therefore, a pair of orthogonal compression and tension members meets at the point of loading, while a set of tension/compression members ends at the support points (see Figure 2.11 (a)). After knowing the local structural patterns, the next step is to trace the principal stress lines. As shown in Figure 2.11 (b), the blue and red PSLs correspond to the tension and compression members, respectively. Based on these PSLs, the connectivity of the truss structure can be defined where the intersection points of the PSLs are the joints, and the PSLs between the intersection points are the structure members (see Figure 2.11) (c)).

The overview of the STO algorithm is illustrated in Figure 2.12. Based on the given design domain with the specified loads and supports, the Finite Element Analysis (FEA) is used to compute the stress field in the design domain, and identify the candidates of joints. After that, the initial structure S_0 is generated by tracing PSLs to connect the load to the supports. The initial structure is then refined iteratively to reduce the total strain energy E in the structure. This topology updating process has two nested loops: the outer loop performs the topology and shape updates, and the inner loop optimizes the size once the topology is updated. The stop criteria is when the change of energy is smaller than a given threshold.

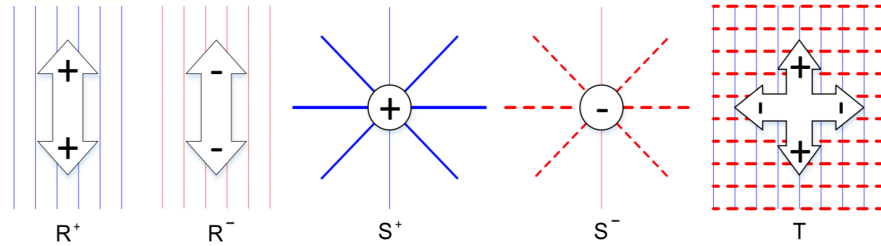


Figure 2.10: Types of optimal regions in Michell trusses. Blue solid lines and red broken lines represent tension and compression bars, respectively. (Figure from Kwok et al. (2016))

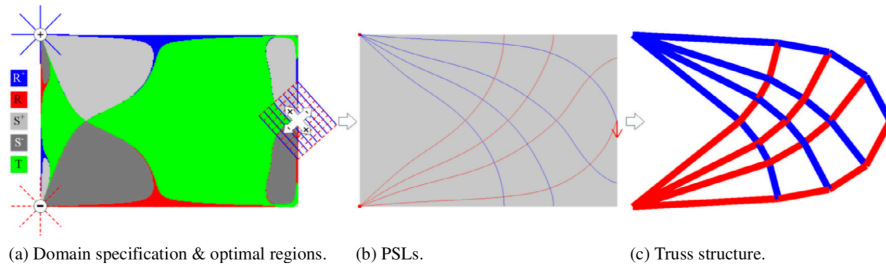


Figure 2.11: The idea of PSLs based truss structure. (Figure from Kwok et al. (2016))

2.2.2 Geometry based method

cross section analysis

Traditionally, structural validity of 3D objects was evaluated using the finite element method. However, FEM involves time-consuming 3D mesh generation and the solution of large linear systems. As a result, FEM is generally not integrated into the real-time visualizations of interactive tools, making it difficult for users to consider structural robustness during incremental trial-and-error design.

To achieve fast shape validation, Umetani & Schmidt (2013) proposed cross-sectional structural analysis. They computed a number of cross sections of an object and determined the forces on the sections. The well-known Euler-Bernoulli assumption (Timoshenko & Goodier 1970) is extended to greatly reduce the complexity of the problem.

Stability analysis

To maintain static equilibrium, the centre of mass of an object must either project along the gravity direction into the support polygon or at the suspension point. While positioning the centroid at the boundary of the support polygon

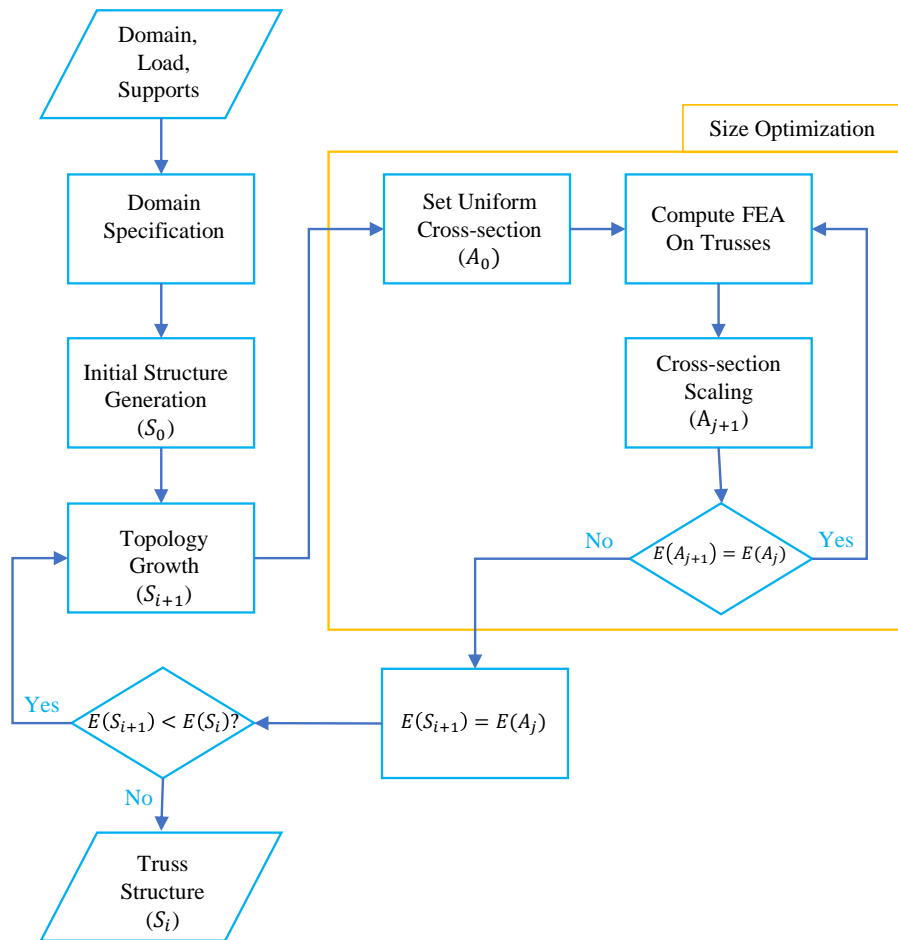


Figure 2.12: The flowchart of the PSLs based STO algorithm. (Figure from Kwok et al. (2016))

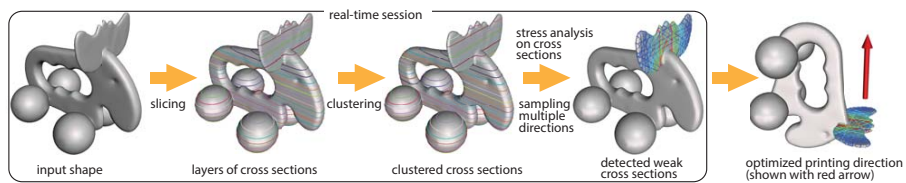


Figure 2.13: Overview of the algorithm by Umetani & Schmidt (2013)

is sufficient for feasibility, the stability is further optimized by setting the ideal centre of mass \mathbf{c}^* to project within a “safe region” of the base as shown in 2.14.

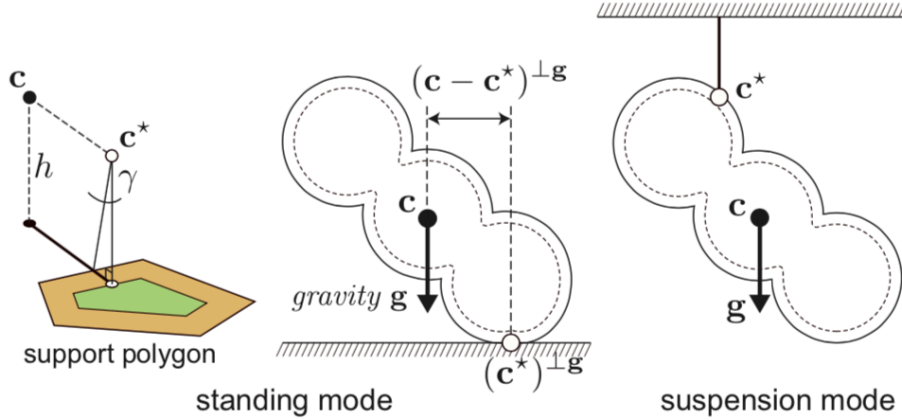


Figure 2.14: (Left) The support polygon for standing models (orange) is chosen as the set of the lowest vertices relative to the gravity direction. The horizontal component of the target centre of mass \mathbf{c}^* , for which we optimize, is the projection of \mathbf{c} onto the “safe region” (green) of the support polygon, defined by the toppling angle γ . We assume that the height of \mathbf{c}^* is equal to that of \mathbf{c} when we define the safe region. (Right) For suspended models the target centre of mass is the selected suspension point. (Figure from [Prévoist et al. \(2013\)](#))

To assist users in producing novel and properly balanced designs, [Prévoist et al. \(2013\)](#) proposed a pipeline by interactively deforming an existing model. The balance optimization problem is formulated as an energy minimization, improving stability by modifying the volume of the objects, while preserving its surface details.

The method takes an unstable triangle mesh \mathcal{M} representing the outer surface of the model as input. Then it finds an optimal mass distribution to carve the interior volume and simultaneously allows deformation of the original surface. To be more precise, given a target centre of mass \mathbf{c}^* , the optimization problem is formulated as:

$$\arg \min_{\mathcal{M}_O, \mathcal{M}_I} (1 - \mu) E_{CoM}(\mathcal{M}_I, \mathcal{M}_O) + \mu E_{\mathcal{M}}(\mathcal{M}_O) \quad (2.2.5)$$

where $E_{\mathcal{M}}(\mathcal{M}_O)$ is the shape-preserving term which measures the deviation of the outer shape \mathcal{M}_O from the input shape \mathcal{M} , and E_{CoM} measures the projected distance to the target centre of mass:

$$E_{CoM}(\mathcal{M}_I, \mathcal{M}_O) = \frac{1}{2} \|(\mathbf{c}(\mathcal{M}_I, \mathcal{M}_O) - \mathbf{c}^*)^{\perp \mathbf{g}}\|^2 \quad (2.2.6)$$

where the vector \mathbf{g} is the gravity direction ($\|\mathbf{g}\| = 1$) and $^{\perp \mathbf{g}}$ denotes the perpendicular projection onto the support plane along the gravity vector.

To carve mass, a voxel grid \mathcal{V} is computed as a discretized representation of the volume. Each voxel is then assigned a binary fill value α_i (1 means full

and 0 means empty), the whole set of these values is denoted by α . In order to reduce the unnecessarily large number of DOFs, the paper uses the simple linear blending skinning (LBS) deformation model with bounded biharmonic weights (Jacobson et al. 2011) for parametrizing the deformation of the solid shape, where users place a small number of handles \mathcal{H} within the shape’s volume.

The final energy formulation in terms of the voxel variables α and deformation handles \mathcal{H} is:

$$\arg \min_{\alpha, \mathcal{H}} (1 - \mu) \frac{1}{2} \|(\mathbf{c}(\mathcal{M}_I(\alpha, \mathcal{H}), \mathcal{M}_O(\mathcal{H})) - \mathbf{c}^*)^{\perp \mathbf{g}}\|^2 + \mu E_{\mathcal{M}}(\mathcal{M}_O(\mathcal{H})) \quad (2.2.7)$$

The objective 2.2.7 has a complex form: it mixes discrete (binary) variables α for the voxel fills with continuous variables \mathcal{H} for the transformations of the handles. The stability optimization therefore is approached with an iterative process that alternates between inner volume and object geometry optimization. The first phase assumes a fixed surface mesh \mathcal{M}_O and aims to find the optimal mass distribution inside the object. The second phase aims to deform the object to improve stability while preserving features. This can be seen as block coordinate descent method (see e.g. Ortega & Rheinboldt (1970)): the algorithm alternates between fixing \mathcal{H} and optimizing 2.2.7 by varying α , and vice versa aiming to decrease the energy in each step.

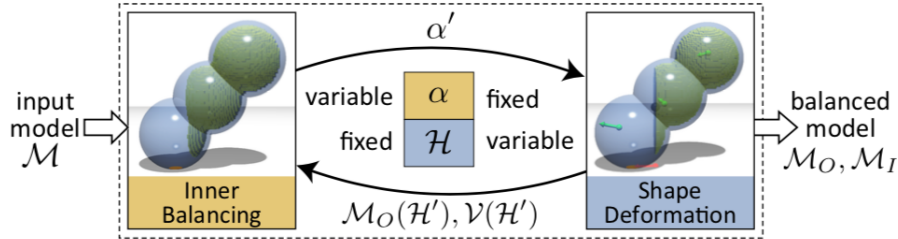


Figure 2.15: The stability optimization alternates between two phases: inner carving and shape deformation. The output is two meshes representing the deformed outer surface \mathcal{M}_O and the inner surface (the boundary of interior voids) \mathcal{M}_I , respectively. (Figure from Prévost et al. (2013))

Freeform structures

Freeform shapes in architecture is an area of great engineering challenges and novel design idea. Existing literature has been motivated by the problems in fabrication of steel/glass and other structures and mostly aims at the realizations of freeform shapes by meshes with planar faces (Glymph et al. 2004, Liu et al. 2006).

To deal with an important class of fabrication constraints of planar construction material such as glass or plywood, Cutler & Whiting (2007) presented

an iterative clustering method to remesh complex curved input surface into planar panels following a cost function. And edges are carefully arranged to form solid continuous ribs to carry the forces from the roof down to the foundation (Holgate 1997, Schober & Kuerschner 2005). To overcome the challenge in the architectural design of freeform shapes, Pottmann et al. (2007) presented a method using local structure of single- and multi-layer constructions along with mesh parallelism.

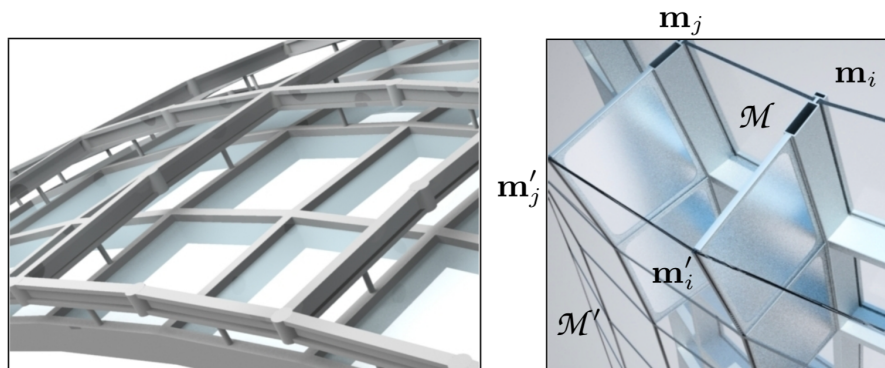


Figure 2.16: Multi-layer constructions based on the geometric support structure defined by two parallel meshes \mathcal{M} , \mathcal{M}' at approximately constant distance. On the left, the lower layer of the glass roof is suspended from the upper layer which has a structural function. The right-hand side image shows a rudimentary construction of a glass facade where the closed space between layers has an insulating function. (Figure from Pottmann et al. (2007))

Later Pottmann et al. (2008) presented a new concept of semi-discrete surface representation, which constitutes a link between smooth and discrete surfaces, to solve the problem of covering freeform surface by single curved panels, and also introduced another concept of a support structure of a polyhedral cell packing for quad meshes or hex-dominant meshes in Pottmann et al. (2015).

Grid-shell structures

Grid-shells, such as steel-glass structures, have been used for about 40 years in architecture (Frei & Rasch 1995). In the field of architectural geometry, most contributions are concerned with the optimization of geometric properties of polygonal meshes, mostly quadrilateral mesh to approximate a free-form surface. Many works address the planarity of faces, such the construction of PQ (planar quad) meshes (Liu et al. 2011, Yang et al. 2011, Zadavec et al. 2010), CP (cell packing) meshes (Schiftner et al. 2009, Pottmann et al. 2015), and polygonal hex-dominant meshes (Tang et al. 2014, Cutler & Whiting 2007, Li et al. 2015). Some works try to approximate surface by a union of patches, so-called panels (Pottmann et al. 2008, Eigensatz et al. 2010). Among these only a few works

take the statics of structures into account when designing the grid structure. Pirazzi et al. (2006) developed the software GEOS to generate the form and the design of the optimized grid to the final construction of lightweight space structures. By arranging ribs on the surface to geodesic lines, bending about the strong axis of the boards can be avoided. Schiffner & Balzer (2010) presented a simple but effective statics-aware initialization procedure for the layout of PQ meshes approximating a given freeform surface.

Driven by the statics of the input surface and aiming at improving the strength of the stiffened structure, Pietroni et al. (2014, 2015) introduced a framework for the generation of grid-shell structures that achieve excellent static performances based on Voronoi diagrams.

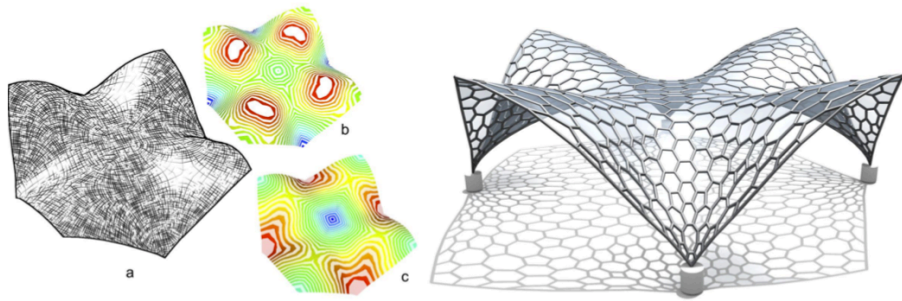


Figure 2.17: A FEM static analysis of the input surface is performed to obtain a stress tensor field, which is decomposed into a double orthogonal line field (a), an anisotropy scalar field (b) and a density scalar field (c). Then an Anisotropic Centroidal Voronoi Tessellation is built with its elements sized and aligned according to the stress tensor field; this tessellation is optimized for symmetry and regularity of faces. The resulting grid-shell is hex-dominant and it is designed to fulfil the required static properties. (Figure from Pietroni et al. (2014))

The initial input of the system is a surface and the system aims to produce a grid-shell that approximates the surface closely. A static analysis of the surface is performed to obtain an anisotropic, non-Euclidean metric described by the stress tensor. To transform this anisotropic metric into an Euclidean metric, the surface is deformed similar to Panozzo et al. (2014) on the deformed surface. The Centroidal Voronoi Tessellation of the deformed surface is built on sampled points by Poisson sampling. The diagram is mapped back to the original surface to obtain an Anisotropic Centroidal Voronoi Tessellation.

2.3 Summary

This chapter has studied the development of stiffened plate element methods. Various models have been proposed by researchers to study the behaviours of stiffened plates including lumped model, orthotropic model, isoparametric quadratic bending elements, arbitrary stiffening elements, etc. Among all these

models and elements, the arbitrary stiffening element has the advantage of keeping the geometry and topology of the object the same, but integrating the contribution of stiffeners to the attaching plate elements so that the positioning of the stiffeners can be arbitrary within the plate element. Hence, arbitrary stiffening element is adopted in this research to analyse the behaviour of the objects.

In the field of 3D printing structural analysis, a lot of research is focusing on using geometric based method to study the behaviour of objects under external loads. Although geometric based method is popular and fast, the disadvantage of this method is that only surface properties have been taken into consideration. To improve the accuracy of geometric based method, FEM based method has also been proposed and researched by researchers. In order to obtain the most accurate results as possible, the research in this thesis is based on FEM method and the well developed arbitrary stiffening element is adopted and applied to optimise the supporting structures for thin-shell geometries.

Chapter 3

Finite elements of rib-shell structure

The finite element method is a numerical technique originated as a method of stress analysis in the design of aircrafts. It started as an extension of matrix method of structural analysis. But the advance of the technology enables the method to approximate solutions while maintains all the complexities of the problems, like varying shape, boundary conditions and loads. Because of its diversity and flexibility as an analysis tool, FEM is receiving much attention in a wide range of research fields. Today FEM is applied not in solid mechanics analysis, but also in the analysis of fluid flow, heat transfer, electric and magnetic fields and many others. Civil engineers use this method extensively for the analysis of beams, spaceframes, plates, shells, folded plates, foundations, rock mechanics problems and seepage analysis of fluid through porous media.

When a flat plate is subjected to both in-plane and transverse or normal loads as shown in Figure 3.1 any point inside the plate can have displacement components u, v , and w parallel to x, y , and z axes, respectively. In the small deflection (or linear) theory of thin plates, the transverse deflection w is uncoupled from the in-plane deflections u and v . Consequently, the stiffness matrices for the in-plane and transverse deflections are also uncoupled and they can be calculated independently. Thus, if a plate is subjected to in-plane loads only, it will undergo deformation in its plane only. In this case, the plate is said to be under the action of “membrane” forces. Similarly, if the plate is subjected to transverse loads (and/or bending moments), any point inside the plate experiences essentially a lateral displacement w (in-plane displacements u and v are also experienced because of the rotation of the plate element). In this case. the plate is said to be under the action of bending forces. The in-plane and bending analysis of plates is considered in this chapter. If the plate elements are used for the analysis of three-dimensional structures, such as folded plate structures, both in-plane and bending actions have to be considered in the development of element properties.

In this chapter, basic finite elements including Constant Strain Triangle,

Discrete Kirchhoff Triangle and Beam elements are introduced and formulated. This aspect of coupling the membrane and bending actions of a plate element is also considered in this chapter.

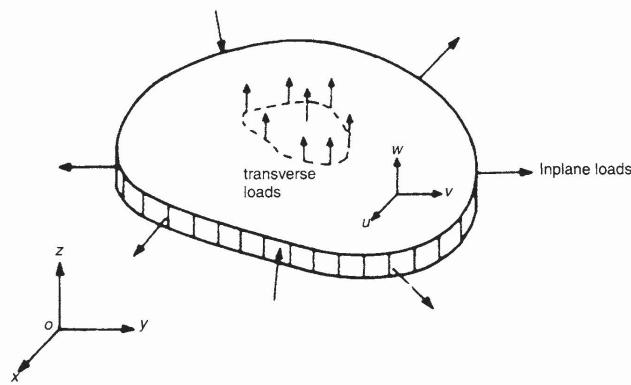


Figure 3.1: In-plane and transverse loads in a plane

3.1 Constant strain triangle element

The in-plane behaviour of thin shell structures is simulated using triangular membrane elements. In this section, the simple 2D constant strain triangle element is discussed and used to determine in-plane deformations and stresses within thin shell.

3.1.1 Displacement and shape function

The triangular membrane element is considered to lie in the xy plane of a local xy coordinate system as shown in Figure 3.2. The nodes are arranged as i, j and m in anti-clockwise. Each node includes 2 degrees of freedom. The displacement components can be expressed as:

$$\mathbf{q}^e = [u_i \ v_i \ u_j \ v_j \ u_m \ v_m]^T \quad (3.1.1)$$

By assuming a linear displacement variation inside the element and introducing a set of area coordinates, the displacement model can be expressed as:

$$\begin{aligned} u &= \alpha_1 + \alpha_2 x + \alpha_3 y \\ v &= \alpha_4 + \alpha_5 x + \alpha_6 y \end{aligned} \quad (3.1.2)$$

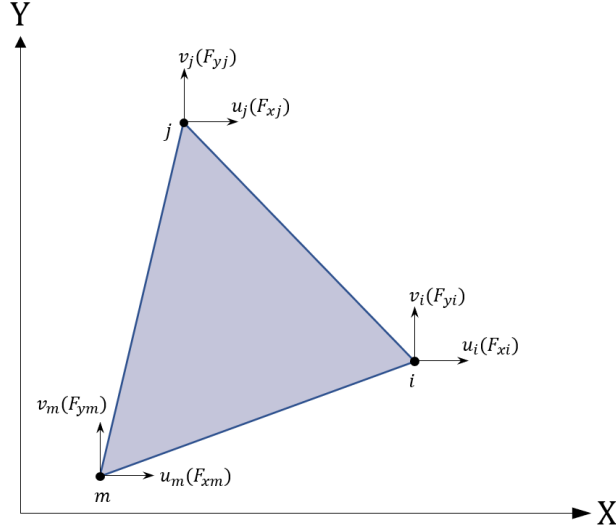


Figure 3.2: Triangular membrane element

By considering the displacements u_i and v_i as the local degrees of freedom of node i, j, m , the constants a_1, \dots, a_6 can be evaluated. Thus, by using the conditions

$$\begin{aligned}
 u_i &= \alpha_1 + \alpha_2 x_i + \alpha_3 y_i \\
 v_i &= \alpha_4 + \alpha_5 x_i + \alpha_6 y_i \\
 u_j &= \alpha_1 + \alpha_2 x_j + \alpha_3 y_j \\
 v_j &= \alpha_4 + \alpha_5 x_j + \alpha_6 y_j \\
 u_m &= \alpha_1 + \alpha_2 x_m + \alpha_3 y_m \\
 v_m &= \alpha_4 + \alpha_5 x_m + \alpha_6 y_m
 \end{aligned}$$

The constants $\alpha_1, \dots, \alpha_6$ can be expressed in terms of the nodal degrees of freedom:

$$\alpha_1 = \frac{1}{2\Delta} \begin{vmatrix} u_i & x_i & y_i \\ u_j & x_j & y_j \\ u_m & x_m & y_m \end{vmatrix} \quad \alpha_2 = \frac{1}{2\Delta} \begin{vmatrix} 1 & u_i & y_i \\ 1 & u_j & y_j \\ 1 & u_m & y_m \end{vmatrix} \quad \alpha_3 = \frac{1}{2\Delta} \begin{vmatrix} 1 & x_i & u_i \\ 1 & x_j & u_j \\ 1 & x_m & u_m \end{vmatrix} \quad (3.1.3)$$

$$\alpha_4 = \frac{1}{2\Delta} \begin{vmatrix} v_i & x_i & y_i \\ v_j & x_j & y_j \\ v_m & x_m & y_m \end{vmatrix} \quad \alpha_5 = \frac{1}{2\Delta} \begin{vmatrix} 1 & v_i & y_i \\ 1 & v_j & y_j \\ 1 & v_m & y_m \end{vmatrix} \quad \alpha_6 = \frac{1}{2\Delta} \begin{vmatrix} 1 & x_i & v_i \\ 1 & x_j & v_j \\ 1 & x_m & v_m \end{vmatrix} \quad (3.1.4)$$

where

$$2\Delta = \begin{vmatrix} 1 & x_i & y_i \\ 1 & x_j & y_j \\ 1 & x_m & y_m \end{vmatrix}$$

Substituting Equation 3.1.3 into Equation 3.1.2:

$$\begin{aligned} u &= \frac{1}{2\delta} [(a_i + b_i x + c_i y)u_i + (a_j + b_j x + c_j y)u_j + (a_m + b_m x + c_m y)u_m] \\ v &= \frac{1}{2\delta} [(a_i + b_i x + c_i y)v_i + (a_j + b_j x + c_j y)v_j + (a_m + b_m x + c_m y)v_m] \end{aligned} \quad (3.1.5)$$

where

$$\begin{aligned} a_i &= x_j y_m - x_m y_j \\ b_i &= y_j - y_m \quad (i, j, m) \\ c_i &= x_m - x_j \end{aligned} \quad (3.1.6)$$

Let

$$N_i = \frac{(a_i + b_i x + c_i y)}{2\Delta} \quad (i, j, m) \quad (3.1.7)$$

This leads to the displacement model:

$$\begin{aligned} \mathbf{U} &= \begin{bmatrix} u(x, y) \\ v(x, y) \end{bmatrix} = \mathbf{N} \mathbf{q}^e \\ &= \begin{bmatrix} N_i(x, y) & 0 & N_j(x, y) & 0 & N_m(x, y) & 0 \\ 0 & N_i(x, y) & 0 & N_j(x, y) & 0 & N_m(x, y) \end{bmatrix} \begin{bmatrix} u_i \\ v_i \\ u_j \\ v_j \\ u_m \\ v_m \end{bmatrix} \end{aligned}$$

3.1.2 Element strain

By using the relations:

$$\boldsymbol{\varepsilon} = \begin{bmatrix} \varepsilon_{xx} \\ \varepsilon_{yy} \\ \varepsilon_{xy} \end{bmatrix} = \begin{bmatrix} \frac{\partial u}{\partial x} \\ \frac{\partial v}{\partial y} \\ \frac{\partial u}{\partial y} + \frac{\partial v}{\partial x} \end{bmatrix} \quad (3.1.8)$$

the components of strain can be expressed in terms of nodal displacements as:

$$\boldsymbol{\varepsilon} = \mathbf{B} \mathbf{q}^e \quad (3.1.9)$$

where

$$\mathbf{B} = \frac{1}{2\Delta} \begin{bmatrix} b_1 & 0 & b_2 & 0 & b_3 & 0 \\ 0 & c_1 & 0 & c_2 & 0 & c_3 \\ c_1 & b_1 & c_2 & b_2 & c_3 & b_3 \end{bmatrix} \quad (3.1.10)$$

3.1.3 Element stress

The stress-strain relations are given by:

$$\boldsymbol{\sigma} = \mathbf{D}\boldsymbol{\varepsilon} \quad (3.1.11)$$

where

$$\boldsymbol{\sigma} = \begin{bmatrix} \sigma_{xx} \\ \sigma_{yy} \\ \sigma_{xy} \end{bmatrix} \quad (3.1.12)$$

and the stress-strain matrix \mathbf{D} is defined as:

$$\mathbf{D} = \frac{E}{1-\nu^2} \begin{bmatrix} 1 & \nu & 0 \\ \nu & 1 & 0 \\ 0 & 0 & \frac{1-\nu}{2} \end{bmatrix} \quad (3.1.13)$$

where E is Young's modulus, and ν is Poisson's ratio.

3.1.4 Element stiffness

The stiffness matrix of the element \mathbf{K}^e can be found by using:

$$\mathbf{K}^e = \iiint_{\Omega} \mathbf{B}^m \text{at} h s f T \mathbf{D} \mathbf{B} d\Omega = \iint_{\Delta} \mathbf{B}^m \text{at} h s f T \mathbf{D} \mathbf{B} h d\Delta \quad (3.1.14)$$

where Ω denotes the volume of the element.

If the plate thickness is taken as a constant h , the evaluation of the integral in Equation 3.1.14 presents no difficulty since the elements of the matrices \mathbf{B} and \mathbf{D} are all constants (not functions of x and y). Hence, Equation 3.1.14 can be rewritten as:

$$\mathbf{K}^e = \mathbf{B}^m \text{at} h s f T \mathbf{D} \mathbf{B} h \iint_{\Delta} d\Delta = h\Delta \mathbf{B}^m \text{at} h s f T \mathbf{D} \mathbf{B} \quad (3.1.15)$$

3.2 Discrete Kirchhoff triangle element

Apart from in-plane behaviours, thin shell structures also undergo bending deflections. The bending deformations and stresses can be effectively calculated with plate bending elements.

A large number of plate bending elements have been developed and reported. In the classical theory of thin plates discussed in this section, certain simplifying

approximations are made. One of the important assumptions made is that shear deformation is negligible. Some elements have been developed by including the effect of transverse shear deformation also.

According to thin plate theory, the deformation is completely described by the transverse deflection of the middle surface of the plate (w) only. Thus, if a displacement model is assumed for w , the continuity of not only w but also its derivatives has to be maintained between adjacent elements.

3.2.1 Displacement model

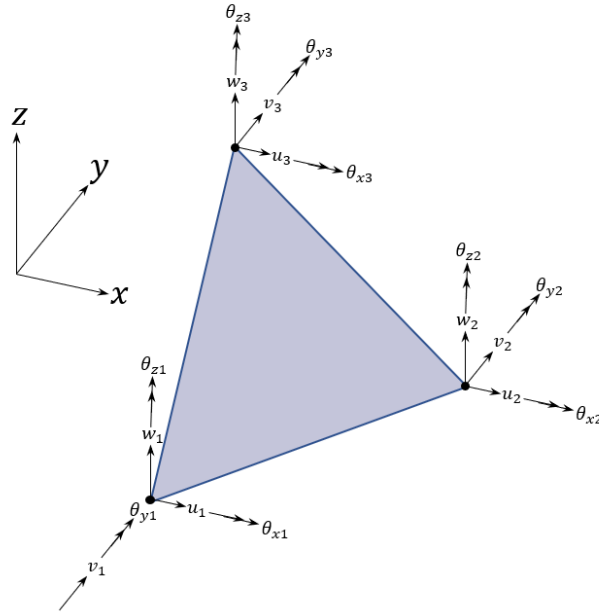


Figure 3.3: Degrees of freedom of triangle element

At each node of a triangular plate element shown in Figure 3.3. The transverse displacement w and rotations about the x and y axes are taken as the degrees of freedom. Since there are nine displacement degrees of freedom in the element, the assumed polynomial for $w(x, y)$ must also contain nine constant terms. To maintain geometric isotropy, the displacement model is taken as:

$$\begin{aligned}
 w = & a_1 L_1 + a_2 L_2 + a_3 L_3 + a_4 L_2 L_3 + a_5 L_3 L_1 + a_6 L_1 L_2 + \\
 & a_7 (L_2 L_3^2 - L_3 L_2^2) + a_8 (L_3 L_1^2 - L_1 L_3^2) + a_9 (L_1 L_2^2 - L_2 L_1^2)
 \end{aligned} \tag{3.2.1}$$

The first three terms represent rigid displacements and terms 3 ~ 6 correspond to constant strain. The constants (a_1, a_2, \dots, a_9) have to be determined from the nodal conditions:

Substituting area coordinates of each node into Equation 3.2.1 will derive:

$$\begin{aligned} a_1 &= w_1 \\ a_2 &= w_2 \\ a_3 &= w_3 \end{aligned} \quad (3.2.2)$$

The derivatives of deflection w with respect to area coordinates are determined by:

$$\begin{aligned} \frac{\partial w}{\partial L_1} &= w_1 - w_3 - a_4 L_2 + a_5 (L_3 - L_1) + a_6 L_2 + \\ &\quad a_7 (L_2^2 - 2L_2 L_3) + a_8 (4L_1 L_3 - L_1^2 - L_3^2) + a_9 (L_2^2 - 2L_1 L_2) \\ \frac{\partial w}{\partial L_2} &= w_2 - w_3 + a_4 (L_3 - L_2) - a_5 L_1 + a_6 L_1 + \\ &\quad a_7 (L_3^2 + L_2^2 - 4L_2 L_3) + a_8 (2L_1 L_3 - L_1^2) + a_9 (2L_1 L_2 - L_1^2) \end{aligned} \quad (3.2.3)$$

Note L_3 is not an independent variable, it should be regarded as $L_3 = 1 - L_1 - L_2$. The constants a_4, \dots, a_9 can be obtained by:

$$\begin{aligned} a_4 &= \frac{w_{,L_{23}} - w_{,L_{22}}}{2} \\ a_5 &= \frac{w_{,L_{13}} - w_{,L_{11}}}{2} \\ a_6 &= \frac{w_{,L_{12}} + w_{,L_{21}} - w_{,L_{11}} - w_{,L_{22}}}{2} \\ a_7 &= w_3 - w_2 + \frac{w_{,L_{23}} + w_{,L_{22}}}{2} \\ a_8 &= w_1 - w_3 - \frac{w_{,L_{11}} + w_{,L_{13}}}{2} \\ a_9 &= w_2 - w_1 + \frac{w_{,L_{11}} + w_{,L_{12}} - w_{,L_{21}} - w_{,L_{22}}}{2} \end{aligned} \quad (3.2.4)$$

In Equation 3.2.4, $w_{,L_{ij}}$ means derivative of deflection w to area coordinate L_i at node j .

Substituting area coordinates of three nodes into equation 3.2.3 will give:

$$\begin{aligned} w_{,L_{11}} &= w_1 - w_3 - a_5 - a_8 \\ w_{,L_{12}} &= w_1 - w_3 - a_4 + a_6 + a_7 + a_9 \\ w_{,L_{13}} &= w_1 - w_3 + a_5 - a_8 \\ w_{,L_{21}} &= w_2 - w_3 - a_5 + a_6 - a_8 - a_9 \\ w_{,L_{22}} &= w_2 - w_3 - a_4 + a_7 \\ w_{,L_{23}} &= w_2 - w_3 + a_4 + a_7 \end{aligned}$$

Substituting Equations 3.2.2 and 3.2.4 into Equation 3.2.1 will give:

$$w = [\bar{N}_i \quad \bar{N}_j \quad \bar{N}_m] \begin{bmatrix} \bar{\delta}_i \\ \bar{\delta}_j \\ \bar{\delta}_m \end{bmatrix} \quad (3.2.5)$$

where:

$$\begin{aligned} \bar{\delta}_1 &= [w_1 \quad w_{,L_{11}} \quad w_{,L_{21}}] \\ \bar{\delta}_2 &= [w_2 \quad w_{,L_{12}} \quad w_{,L_{21}}] \\ \bar{\delta}_3 &= [w_3 \quad w_{,L_{13}} \quad w_{,L_{23}}] \\ \bar{N}_1 &= [N_1 \quad N_{,L_{11}} \quad N_{,L_{21}}] \\ \bar{N}_2 &= [N_2 \quad N_{,L_{12}} \quad N_{,L_{21}}] \\ \bar{N}_3 &= [N_3 \quad N_{,L_{13}} \quad N_{,L_{23}}] \end{aligned}$$

and the components of the shape function are:

$$\begin{aligned} N_1 &= L_1 - (L_1L_2^2 - L_2L_1^2) + (L_3L_1^2 - L_1L_3^2) \\ N_{L_{11}} &= \frac{-L_1L_2 - L_3L_1 + (L_1L_2^2 - L_2L_1^2) - (L_3L_1^2 - L_1L_3^2)}{2} \\ N_{L_{21}} &= \frac{L_1L_2 + (L_2L_1^2 - L_1L_2^2)}{2} \\ N_2 &= L_2 - (L_2L_3^2 - L_3L_2^2) + (L_1L_2^2 - L_2L_1^2) \\ N_{L_{12}} &= \frac{L_1L_2 + (L_1L_2^2 - L_2L_1^2)}{2} \\ N_{L_{22}} &= \frac{-L_2L_3 - L_1L_2 + (L_2L_3^2 - L_3L_2^2) - (L_1L_2^2 - L_2L_1^2)}{2} \\ N_3 &= L_3 - (L_3L_1^2 - L_1L_3^2) + (L_2L_3^2 - L_3L_2^2) \\ N_{L_{13}} &= \frac{L_1L_3 + (L_1L_3^2 - L_3L_1^2)}{2} \\ N_{L_{23}} &= \frac{L_2L_3 + (L_2L_3^2 - L_3L_2^2)}{2} \end{aligned}$$

The relationship between Cartesian coordinates and area coordinates is:

$$\begin{aligned} \frac{\partial x}{\partial L_1} &= x_1 - x_3 = c_1 \\ \frac{\partial y}{\partial L_1} &= y_1 - y_3 = -b_1 \\ \frac{\partial x}{\partial L_2} &= x_2 - x_3 = -c_1 \\ \frac{\partial y}{\partial L_2} &= x_2 - x_3 = b_1 \end{aligned} \quad (3.2.6)$$

which leads to

$$\begin{aligned}\frac{\partial w}{\partial L_1} &= c_2 \frac{\partial w}{\partial x} - b_2 \frac{\partial w}{\partial y} = -b_2 \theta_x - c_2 \theta_y \\ \frac{\partial w}{\partial L_2} &= -c_2 \frac{\partial w}{\partial x} + b_2 \frac{\partial w}{\partial y} = b_2 \theta_x + c_2 \theta_y\end{aligned}\quad (3.2.7)$$

The relation of nodal displacements between Cartesian system and area system is:

$$\bar{\delta}_i = \begin{bmatrix} w_i \\ w_{,L_{11}} \\ w_{,L_{21}} \end{bmatrix} = \begin{bmatrix} 1 & 0 & 0 \\ 0 & -b_2 & -c_2 \\ 0 & b_1 & c_1 \end{bmatrix} \begin{bmatrix} w_i \\ \theta_{xi} \\ \theta_{yi} \end{bmatrix} = \mathbf{P} \delta_i \quad (3.2.8)$$

Using Equation 3.2.8, the Equation 3.2.5 can be rewritten as:

$$w = [\bar{\mathbf{N}}_1 \quad \bar{\mathbf{N}}_2 \quad \bar{\mathbf{N}}_3] \begin{bmatrix} \mathbf{P} & \mathbf{0} & \mathbf{0} \\ \mathbf{0} & \mathbf{P} & \mathbf{0} \\ \mathbf{0} & \mathbf{0} & \mathbf{P} \end{bmatrix} \begin{bmatrix} \delta_1 \\ \delta_2 \\ \delta_3 \end{bmatrix} = [\mathbf{N}_1 \quad \mathbf{N}_2 \quad \mathbf{N}_3] \begin{bmatrix} \delta_1 \\ \delta_2 \\ \delta_3 \end{bmatrix} \quad (3.2.9)$$

where

$$\begin{aligned}\mathbf{N}_i &= \bar{\mathbf{N}}_i \mathbf{P} = [N_i \quad N_{xi} \quad N_{yi}] \\ N_i &= L_i + L_i^2 L_j + L_i^2 L_m - L_i L_j^2 - L_i L_m^2 \quad (i = 1, 2, 3) \\ N_{xi} &= b_j L_i^2 L_m - b_m L_i^2 L_j + \frac{(b_j - b_m)}{2} L_i L_j L_m \\ N_{yi} &= c_j L_i^2 L_m - c_m L_i^2 L_j + \frac{c_j - c_m}{2} L_i L_j L_m\end{aligned}$$

3.2.2 Stiffness matrix

The shape function uses L_1 and L_2 as independent variables. To obtain stiffness matrix in global space, transformation matrix \mathbf{T} is introduced:

$$\begin{bmatrix} \partial/\partial x \\ \partial/\partial y \end{bmatrix} = \frac{1}{2\Delta} \begin{bmatrix} b_1 & b_2 \\ c_1 & c_2 \end{bmatrix} \begin{bmatrix} \partial/\partial L_1 \\ \partial/\partial L_2 \end{bmatrix} \quad (3.2.10)$$

From the first derivatives given in the above equation, the second derivatives are obtained as

$$\begin{bmatrix} \partial^2/\partial x^2 \\ \partial^2/\partial y^2 \\ 2\partial^2/\partial x\partial y \end{bmatrix} = \frac{1}{4\Delta^2} \mathbf{T} \begin{bmatrix} \partial^2/\partial L_1^2 \\ \partial^2/\partial L_2^2 \\ \partial^2/\partial L_1\partial L_2 \end{bmatrix} \quad (3.2.11)$$

where

$$\mathbf{T} = \begin{bmatrix} b_1^2 & b_2^2 & 2b_1b_2 \\ c_1^2 & c_2^2 & 2c_1c_2 \\ 2b_1c_1 & 2b_2c_2 & 2(b_1c_2 + b_2c_1) \end{bmatrix} \quad (3.2.12)$$

The element strain matrix becomes:

$$\boldsymbol{\epsilon} = \mathbf{B}\boldsymbol{\delta}^e = z [\mathbf{B}_i \quad \mathbf{B}_j \quad \mathbf{B}_m] \begin{bmatrix} \boldsymbol{\delta}_i \\ \boldsymbol{\delta}_j \\ \boldsymbol{\delta}_m \end{bmatrix} \quad (3.2.13)$$

where

$$\mathbf{B}_k = - \begin{bmatrix} \mathbf{N}_{k,xx} \\ \mathbf{N}_{k,yy} \\ \mathbf{N}_{k,xy} \end{bmatrix} = -\frac{1}{4\Delta^2} \mathbf{T} \begin{bmatrix} \mathbf{N}_{k,11} \\ \mathbf{N}_{k,22} \\ \mathbf{N}_{k,12} \end{bmatrix} \quad (k = 1, 2, 3) \quad (3.2.14)$$

The element stiffness matrix in global space is obtained as:

$$\mathbf{K}^e = \frac{h^3}{12} \iint_{\Omega} \mathbf{B}^T \mathbf{D} \mathbf{B} dx dy \quad (3.2.15)$$

3.2.3 Gauss quadrature

To simplify computation, Gauss quadrature is used to obtain the integral involved in Equation 3.2.17 as discussed below.

Firstly, the integral over the triangular domain Ω is converted into:

$$\iint_{\Omega} f(L_1, L_2, L_3) dx dy = 2\Delta \int_0^1 \int_0^{1-L_1} f(L_1, L_2, L_3) dL_1 dL_2 \quad (3.2.16)$$

The right-hand side term can be calculated using:

$$\int_0^1 \int_0^{1-L_1} f(L_1, L_2, L_3) dL_1 dL_2 = \sum_{i=1}^n W_i f(L_{i1}, L_{i2}, L_{i3}) \quad (3.2.17)$$

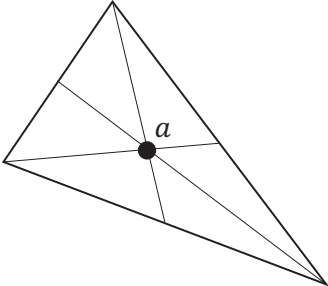
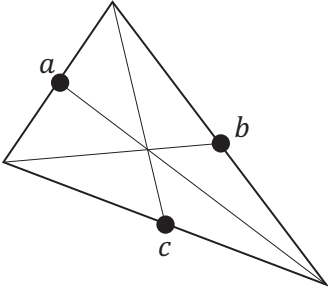
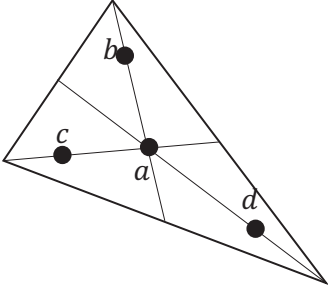
In Equation 3.2.17, n is the number of Gauss points, W_i is weight, and $(L_{i1}, L_{i2}, L_{i3}), i = 1, 2, 3$ are the integration points.

3.2.4 Transformation matrix

Since the shape functions are defined in the plane of the triangle, the z-coordinates for the nodes in the plane are equal to zero.

Assuming that the triangular element under consideration is an interior element of a large structure. Let the node numbers 1, 2, and 3 of the element correspond to the node numbers i, j , and k , respectively, of the global system. Then place the origin of the local xy system at node 1 (node i), and take the

Table 3.1: 2D Gauss points and weights

Figure	Points	Weights
	$a = (1/3, 1/3, 1/3)$	0.5
	$a = (0.5, 0.5, 0.0)$ $b = (0.0, 0.5, 0.5)$ $c = (0.5, 0.0, 0.5)$	1/6 1/6 1/6
	$a = (1/3, 1/3, 1/3)$ $b = (0.6, 0.2, 0.2)$ $c = (0.2, 0.6, 0.2)$ $d = (0.2, 0.2, 0.6)$	-27/96 25/96 25/96 25/96

y axis along the edge 12 (edge ij) and the x axis perpendicular to the y axis directed toward node 3 (node k) as shown in Figure 3.5.

The directions are defined as:

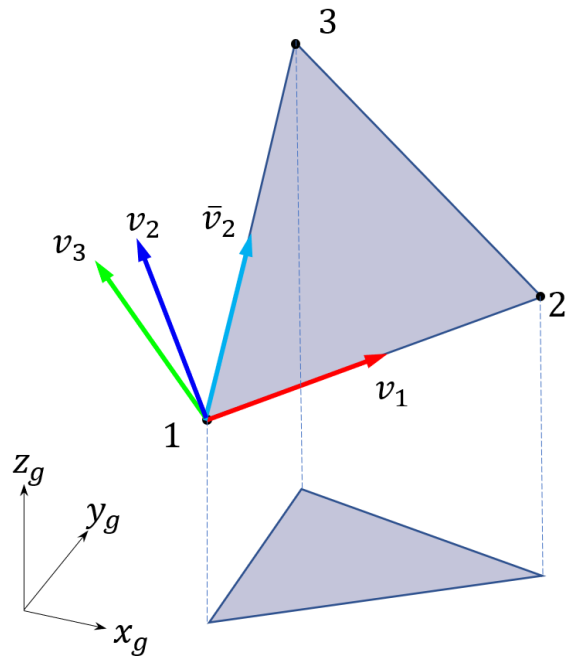


Figure 3.4: Transformation matrix in 3D

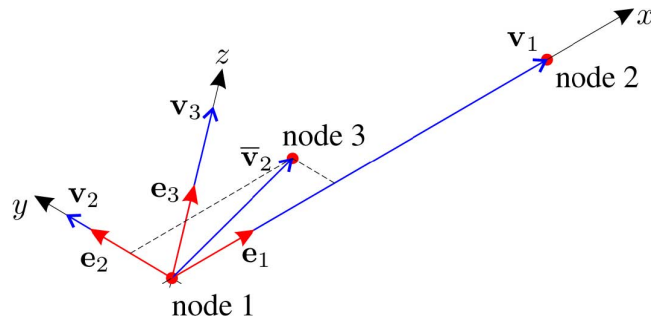


Figure 3.5: Unit vectors describing xyz system.

$$\mathbf{v}_1 = \begin{bmatrix} x_2 - x_1 \\ y_2 - y_1 \\ z_2 - z_1 \end{bmatrix}$$

$$\bar{\mathbf{v}}_2 = \begin{bmatrix} x_3 - x_1 \\ y_3 - y_1 \\ z_3 - z_1 \end{bmatrix}$$

$$\mathbf{v}_3 = \mathbf{v}_1 \times \bar{\mathbf{v}}_2$$

$$\mathbf{v}_2 = \mathbf{v}_3 \times \mathbf{v}_1$$

Since the unit vectors can be expressed as:

$$\begin{aligned} \mathbf{e}_1 &= \frac{\mathbf{v}_1}{|\mathbf{v}_1|} \\ \mathbf{e}_2 &= \frac{\mathbf{v}_2}{|\mathbf{v}_2|} \\ \mathbf{e}_3 &= \frac{\mathbf{v}_3}{|\mathbf{v}_3|} \end{aligned}$$

the transformation matrix is:

$$\mathbf{T} = [\mathbf{e}_1 \quad \mathbf{e}_2 \quad \mathbf{e}_3] \quad (3.2.18)$$

With the obtained transformation matrix, the nodal coordinates in the local coordinate system are related to the nodal coordinates in the global coordinate system by

$$\begin{bmatrix} x_l \\ y_l \\ z_l \end{bmatrix} = \mathbf{T}^T \begin{bmatrix} x_g \\ y_g \\ z_g \end{bmatrix} \quad (3.2.19)$$

3.2.5 Global element stiffness matrix

The full transformation matrix \mathbf{T}_g (12×12) can be obtained from \mathbf{T} (3×3) through the following equation

$$\mathbf{T}_g = \begin{bmatrix} \mathbf{T} & \mathbf{0} & \mathbf{0} \\ \mathbf{0} & \mathbf{T} & \mathbf{0} \\ \mathbf{0} & \mathbf{0} & \mathbf{T} \end{bmatrix} \quad (3.2.20)$$

and the global element stiffness matrix below is obtained by multiplying the local element stiffness matrix with the full transformation matrix and its transpose

$$\mathbf{K}_g^e = \mathbf{T}_g \mathbf{K}^e \mathbf{T}_g^T \quad (3.2.21)$$

3.3 Drilling degree

It is well known that when all elements connected to a node are coplanar, zero stiffness appears in the direction normal to the plane rotation (θ_z). This causes the assembly stiffness matrix at a global level to be singular (Zienkiewicz & Taylor 1991). The normal approach to deal with the stiffness of the drilling degrees of freedom is to approximate the stiffness for the drilling degrees of freedom. Bathe & Ho (1981) developed a flat shell triangular element by combining the CST element for membrane stiffness and the plate bending element using the Mindlin theory of plates for the bending stiffness. They introduced a fictitious stiffness to approximate the drilling degrees of freedom in the development of the element

stiffness matrix for the triangular flat shell element. Knight (1997) suggested that a very small value be specified for the stiffness of the drilling degrees of freedom so that the contribution to the strain energy equation from this term will be zero. Zienkiewicz & Taylor (1991) developed the addition of a 3×3 artificial rotational stiffness matrix \mathbf{K}_θ^e for triangular flat shell elements. This stabilization stiffness matrix which also appears in a more recent formulation (Cook 1993, Zengjie & Wanji 2003) is given by:

$$\begin{bmatrix} M_{z1} \\ M_{z2} \\ M_{z3} \end{bmatrix} = \alpha EA \begin{bmatrix} 1 & -0.5 & -0.5 \\ -0.5 & 1 & -0.5 \\ -0.5 & -0.5 & 1 \end{bmatrix} \begin{bmatrix} \theta_{z1} \\ \theta_{z2} \\ \theta_{z3} \end{bmatrix} = \mathbf{K}_\theta^e \begin{bmatrix} \theta_{z1} \\ \theta_{z2} \\ \theta_{z3} \end{bmatrix} \quad (3.3.1)$$

where $\theta_{zi} (i = 1, 2, 3)$ is the drilling DOF at the node of the flat element, A is the area of the element, E is the elastic modulus, α is a small constant as $\alpha = t \times 10^{-4}$, and t is the thickness of the element. Equation 3.3.1 is a penalty function and provides a fictitious stiffness for θ_z .

3.4 Beam element

To simulate the behaviour of stiffeners, they are discretized into and treated as beam elements. In this section, beam elements are discussed and formulated to calculate the strain and stress tensors and stiffness matrix of stiffeners.

3.4.1 Displacement model

Each node of beam element has 6 degrees of freedom, corresponding to 6 nodal forces. A beam element with nodes i and j is shown in Figure 3.6. In a right-hand coordinate system, x axis is taken as element axis then y and z axes become main moment axes of cross-section.

The nodal displacements are:

$$\begin{aligned} \boldsymbol{\delta}_i &= [u_i \quad v_i \quad w_i \quad \theta_{xi} \quad \theta_{yi} \quad \theta_{zi}]^T \\ \boldsymbol{\delta}_j &= [u_j \quad v_j \quad w_j \quad \theta_{xj} \quad \theta_{yj} \quad \theta_{zj}]^T \end{aligned} \quad (3.4.1)$$

or in a more simple form:

$$\boldsymbol{\delta}^e = [\boldsymbol{\delta}_i^T \quad \boldsymbol{\delta}_j^T]^T \quad (3.4.2)$$

By assuming a linear change for axial displacement u and angular rotation θ_x , and a cubic variation for deflection v and w , these terms can be represented as:

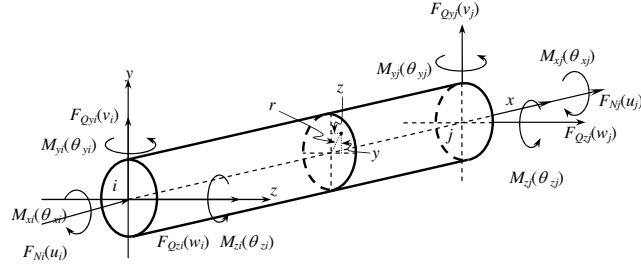


Figure 3.6: Beam element

$$\begin{aligned}
 u &= a_0 + a_1 x \\
 v &= b_0 + b_1 x + b_2 x^2 + b_3 x^3 \\
 w &= c_0 + c_1 x + c_2 x^2 + c_3 x^3 \\
 \theta_x &= e_0 + e_1 x
 \end{aligned} \tag{3.4.3}$$

The axial nodal displacements, deflections and rotations can also be written in a vector form:

$$\begin{aligned}
 \delta_u &= [u_i \quad u_j]^T \\
 \delta_v &= [v_i \quad \theta_{zj} \quad v_j \quad \theta_{zj}]^T \\
 \delta_w &= [w_i \quad \theta_{yj} \quad w_j \quad \theta_{wj}]^T \\
 \delta_\theta &= [\theta_{xi} \quad \theta_{xj}]^T
 \end{aligned} \tag{3.4.4}$$

Equation 3.4.3 becomes:

$$\begin{aligned}
 u &= \mathbf{N}_u \delta_u \\
 \theta_x &= \mathbf{N}_\theta \delta_\theta \\
 v &= \mathbf{N}_v \delta_v \\
 w &= \mathbf{N}_w \delta_w
 \end{aligned} \tag{3.4.5}$$

Any displacement inside the element is expressed as:

$$\mathbf{u} = \begin{bmatrix} u \\ v \\ w \\ \theta_x \end{bmatrix} = \begin{bmatrix} \mathbf{H}_u \\ \mathbf{H}_v \\ \mathbf{H}_w \\ \mathbf{H}_\theta \end{bmatrix} \mathbf{A}^{-1} \boldsymbol{\delta}^e = \mathbf{N} \boldsymbol{\delta}^e \quad (3.4.6)$$

where:

$$\mathbf{H}_u(x) = [1 \ 0 \ 0 \ 0 \ 0 \ 0 \ x \ 0 \ 0 \ 0 \ 0 \ 0] \quad (3.4.7)$$

$$\mathbf{H}_v(x) = [0 \ 1 \ 0 \ 0 \ 0 \ x \ 0 \ x^2 \ 0 \ 0 \ 0 \ x^3] \quad (3.4.8)$$

$$\mathbf{H}_w(x) = [0 \ 0 \ 1 \ 0 \ x \ 0 \ 0 \ 0 \ x^2 \ 0 \ x^3 \ 0] \quad (3.4.9)$$

$$\mathbf{H}_\theta(x) = [0 \ 0 \ 0 \ 1 \ 0 \ 0 \ 0 \ 0 \ 0 \ 0 \ x \ 0] \quad (3.4.10)$$

and

$$\mathbf{A} = \begin{bmatrix} 1 & 0 & 0 & 0 & 0 & 0 & 0 & 0 & 0 & 0 & 0 & 0 \\ 0 & 1 & 0 & 0 & 0 & 0 & 0 & 0 & 0 & 0 & 0 & 0 \\ 0 & 0 & 1 & 0 & 0 & 0 & 0 & 0 & 0 & 0 & 0 & 0 \\ 0 & 0 & 0 & 1 & 0 & 0 & 0 & 0 & 0 & 0 & 0 & 0 \\ 0 & 0 & 0 & 0 & -1 & 0 & 0 & 0 & 0 & 0 & 0 & 0 \\ 0 & 0 & 0 & 0 & 0 & 1 & 0 & 0 & 0 & 0 & 0 & 0 \\ 1 & 0 & 0 & 0 & 0 & 0 & l & 0 & 0 & 0 & 0 & 0 \\ 0 & 1 & 0 & 0 & 0 & l & 0 & l^2 & 0 & 0 & 0 & l^3 \\ 0 & 0 & 1 & 0 & l & 0 & 0 & 0 & l^2 & 0 & l^3 & 0 \\ 0 & 0 & 0 & 1 & 0 & 0 & 0 & 0 & 0 & l & 0 & 0 \\ 0 & 0 & 0 & 0 & -1 & 0 & 0 & 0 & -2l & 0 & -3l^2 & 0 \\ 0 & 0 & 0 & 0 & 0 & 1 & 0 & 2l & 0 & 0 & 0 & 3l^2 \end{bmatrix} \quad (3.4.11)$$

3.4.2 Strain and stress

When a beam undergoes tensile, compressional, bending and torsional deformation, its axial strain is composed of three parts: tensile or compressional strain ϵ_0 , bending strain ϵ_{by} and ϵ_{bz} and shear strain where the shear strain caused by torsion is γ . Hence,

$$\boldsymbol{\epsilon} = \begin{bmatrix} \epsilon_0 \\ \epsilon_{by} \\ \epsilon_{bz} \\ \gamma \end{bmatrix} = \begin{bmatrix} u' \\ -yv'' \\ -zw'' \\ r\theta'_x \end{bmatrix} = \begin{bmatrix} \mathbf{H}'_u \\ -y\mathbf{H}''_v \\ -z\mathbf{H}''_w \\ r\mathbf{H}'_\theta \end{bmatrix} \mathbf{A}^{-1} \boldsymbol{\delta}^e = \mathbf{B} \boldsymbol{\delta}^e \quad (3.4.12)$$

where y and z are the coordinate values of the point in the cross-section, and r is the distance to x axis.

By using Hooke's law, the stress can be expressed as:

$$\boldsymbol{\sigma} = \begin{bmatrix} \sigma_0 \\ \sigma_{by} \\ \sigma_{bz} \\ \tau \end{bmatrix} = \begin{bmatrix} E\mathbf{H}'_u \\ -Ey\mathbf{H}''_v \\ -Ez\mathbf{H}''_w \\ Gr\mathbf{H}'_\theta \end{bmatrix} \mathbf{A}^{-1}\boldsymbol{\delta}^e = \mathbf{D}\mathbf{B}\boldsymbol{\delta}^e \quad (3.4.13)$$

where

$$\mathbf{D} = \text{diag}(E, E, E, G) \quad (3.4.14)$$

3.4.3 Stiffness matrix

The stiffness matrix now can be integrated expressively:

$$\mathbf{K}^e = \iint dA \int_0^l \mathbf{B}^\top \mathbf{D} \mathbf{B} dx$$

$$= \begin{bmatrix} \frac{EA}{l} & 0 & 0 & 0 & 0 & 0 & -\frac{EA}{l} & 0 & 0 & 0 & 0 & 0 \\ 0 & \frac{12EI_z}{l^3} & 0 & 0 & 0 & \frac{6EI_z}{l^2} & 0 & -\frac{12EI_z}{l^3} & 0 & 0 & 0 & \frac{6EI_z}{l^2} \\ 0 & 0 & \frac{12EI_y}{l^3} & 0 & -\frac{6EI_y}{l^2} & 0 & 0 & 0 & -\frac{12EI_y}{l^3} & 0 & -\frac{6EI_y}{l^2} & 0 \\ 0 & 0 & 0 & \frac{GJ_k}{l} & 0 & 0 & 0 & 0 & 0 & -\frac{GJ_k}{l} & 0 & 0 \\ 0 & 0 & -\frac{6EI_y}{l^2} & 0 & \frac{4EI_y}{l} & 0 & 0 & 0 & \frac{6EI_y}{l^2} & 0 & \frac{2EI_y}{l} & 0 \\ 0 & \frac{6EI_z}{l^2} & 0 & 0 & 0 & \frac{4EI_z}{l} & 0 & -\frac{6EI_z}{l^2} & 0 & 0 & 0 & \frac{2EI_z}{l} \\ -\frac{EA}{l} & 0 & 0 & 0 & 0 & 0 & \frac{EA}{l} & 0 & 0 & 0 & 0 & 0 \\ 0 & -\frac{12EI_z}{l^3} & 0 & 0 & 0 & -\frac{6EI_z}{l^2} & 0 & \frac{12EI_z}{l^3} & 0 & 0 & 0 & -\frac{6EI_z}{l^2} \\ 0 & 0 & -\frac{12EI_y}{l^3} & 0 & \frac{6EI_y}{l^2} & 0 & 0 & 0 & \frac{12EI_y}{l^3} & 0 & \frac{6EI_y}{l^2} & 0 \\ 0 & 0 & 0 & -\frac{GJ_k}{l} & 0 & 0 & 0 & 0 & 0 & \frac{GJ_k}{l} & 0 & 0 \\ 0 & 0 & -\frac{6EI_y}{l^2} & 0 & \frac{2EI_y}{l} & 0 & 0 & 0 & \frac{6EI_y}{l^2} & 0 & \frac{4EI_y}{l} & 0 \\ 0 & \frac{6EI_z}{l^2} & 0 & 0 & 0 & \frac{2EI_z}{l} & 0 & -\frac{6EI_z}{l^2} & 0 & 0 & 0 & \frac{4EI_z}{l} \end{bmatrix} \quad (3.4.15)$$

In Equation 3.4.15, $I_y = \iint z^2 dA$ and $I_z = \iint y^2 dA$ are main moments of beam cross-section with respect to y and z axes respectively, J_k is the second area moments about x axis.

3.5 Assembly of Plate and Beam elements

To simulate stiffened structures, stiffness contributions from both plate elements and beam elements are assembled at corresponding nodes in a coupled way to consider the influence of shell and rib network simultaneously.

Figure 3.7 demonstrates how a plate element is reinforced by a beam element. The three nodes of a triangular plate element are denoted as i , j and k . The two nodes of a beam element are connecting to the plate element at nodes j and k respectively. Once elemental stiffness matrices of plate \mathbf{K}_p^e and beam \mathbf{K}_r^e are obtained, they are assembled to the global stiffness matrix. The assembling process is taking block entries from each element and accumulate to corresponding place in the global stiffness matrix. For example, the block entries $\mathbf{K}_{p(ij)}^e$ that

lie in 1st row and 2nd column of plate elemental stiffness \mathbf{K}_p^e are assembled to the block of i th row and j th column of the global stiffness matrix \mathbf{K}^g .

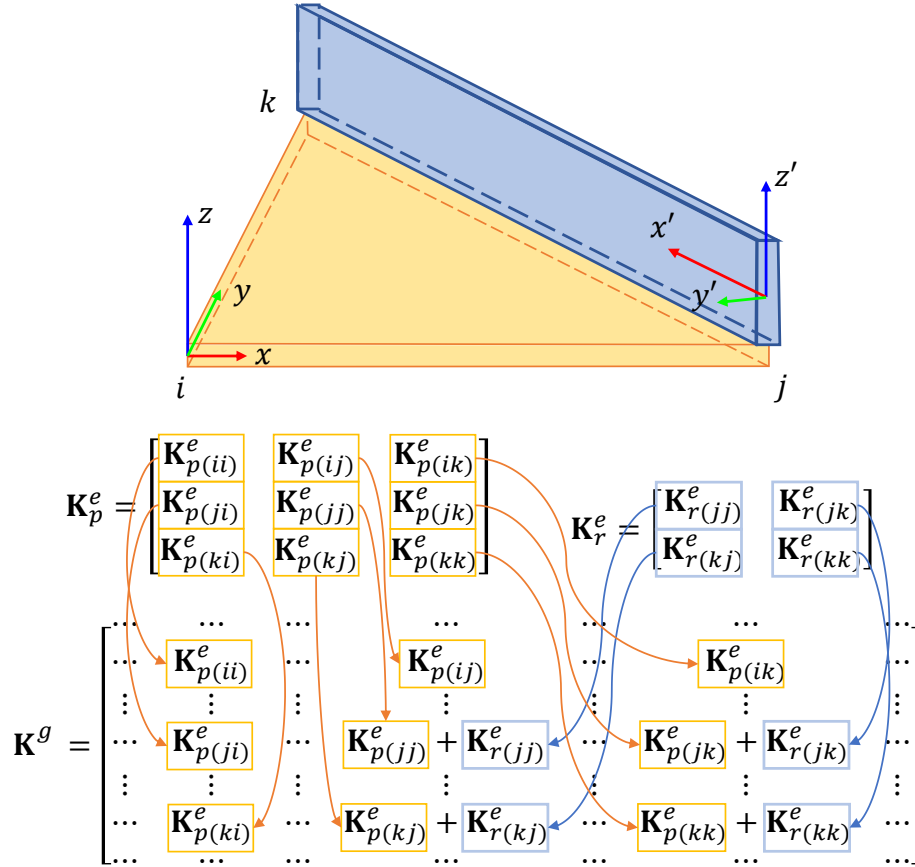


Figure 3.7: Stiffness matrix assembling for a coupled structure.

The assembled stiffness matrix is written as:

$$\mathbf{K}^g = \mathbf{K}_p^e + \mathbf{K}_r^e \quad (3.5.1)$$

3.6 Stress

In materials science, the strength of a material is its ability to withstand an applied load without failure or plastic deformation. The field of strength of materials deals with forces and deformations that result from external forces acting on a material. A load applied to a mechanical member will induce internal forces within the member called stresses which are defined as the force per unit area. The stresses acting on the material cause deformation of the material in various manners. Deformation of the material is called strain defined as extension per unit length. The applied loads may be axial (tensile or compressive), or rotational (torsion or shear). The stresses and strains that develop within a mechanical member must be calculated in order to assess the load capacity of that member. This requires a complete description of the geometry of the member, its constraints, the loads applied to the member and the properties of the material of which the member is composed. With a complete description of the loading and the geometry of the member, the state of stress and the state of strain at any point within the member can be calculated. Once the state of stress and strain within the member is known, the strength (load carrying capacity) of that member, its deformations (any changes in the shape or size of an object due to external actions), and its stability (the ability of the structure to support a specified load without undergoing unacceptable (or sudden) deformations) can be calculated. The calculated stresses may then be compared to some measure of the strength of the member such as its material yield or ultimate strength. The calculated deflection of the member may be compared to a deflection criteria that is based on the member's use. The calculated buckling load of the member may be compared to the applied load. The calculated stiffness and mass distribution of the member may be used to calculate the member's dynamic response.

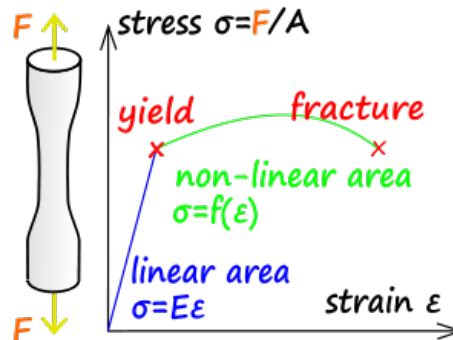


Figure 3.8: Basic static response of a specimen under tension

Material strength is the ability to withstand an applied load without failure or plastic deformation. Yield strength refers to the point on the engineering stress-strain curve (yield stress) beyond which the material experiences deformations that will not be completely reversed upon removal of the loading and as a

result the member will have a permanent deflection. The ultimate strength refers to the maximum stress that a material can withstand while being stretched or pulled before breaking.

3.6.1 Strength terms

Uniaxial stress is determined by

$$\sigma = \frac{F}{A} \quad (3.6.1)$$

where F is the *force*[N] acting on an area A [m²]. The area can be the undeformed area or the deformed area, depending on whether engineering stress or true stress is of interest.

Mechanical properties of materials include the yield strength, tensile strength, fatigue strength, crack resistance, and other characteristics.

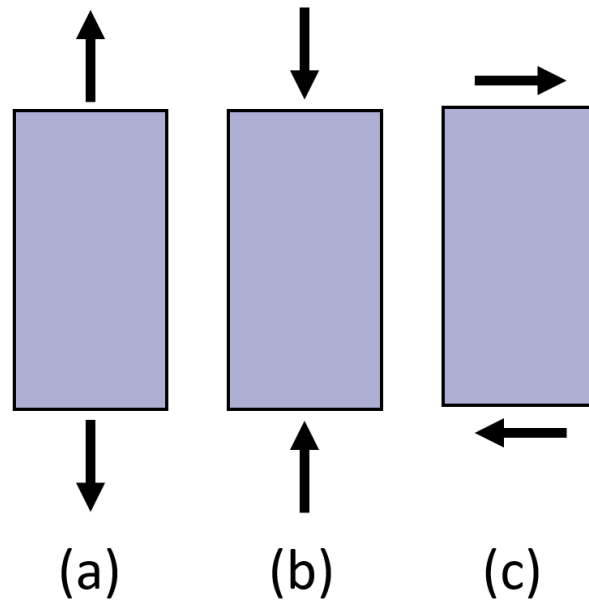


Figure 3.9: A material being loaded in a) tension, b) compression, c) shear

- Yield strength is the lowest stress that produces a permanent deformation in a material. In some materials, like aluminium alloys, the point of yielding is difficult to identify, thus it is usually defined as the stress required to cause 0.2% plastic strain. This is called a 0.2% proof stress.

- Compressive strength is a limit state of compressive stress that leads to failure in a material in the manner of ductile failure (infinite theoretical yield) or brittle failure (rupture as the result of crack propagation, or sliding along a weak plane - see shear strength).
- Tensile strength or ultimate tensile strength is a limit state of tensile stress that leads to tensile failure in the manner of ductile failure (yield as the first stage of that failure, some hardening in the second stage and breakage after a possible “neck” formation) or brittle failure (sudden breaking in two or more pieces at a low stress state).
- Fatigue strength is a measure of the strength of a material or a component under cyclic loading, and is usually more difficult to assess than the static strength measures. Fatigue strength is quoted as stress amplitude or stress range ($\Delta\sigma = \sigma_{\max} - \sigma_{\min}$), usually at zero mean stress, along with the number of cycles to failure under that condition of stress.
- Impact strength, is the capability of the material to withstand a suddenly applied load and is expressed in terms of energy. Often measured with the Izod impact strength test or Charpy impact test, both of which measure the impact energy required to fracture a sample. Volume, modulus of elasticity, distribution of forces, and yield strength affect the impact strength of a material. In order for a material or object to have a high impact strength the stresses must be distributed evenly throughout the object. It also must have a large volume with a low modulus of elasticity and a high material yield strength.

3.6.2 Hooke’s Law

Hooke’s law is a principle of physics that states that the force F needed to extend or compress a spring by some distance X is proportional to that distance. That is: $F = kX$, where k is a constant factor characteristic of the spring: its stiffness, and X is small compared to the total possible deformation of the spring.

Hooke’s law is only a first-order linear approximation to the real response of springs and other elastic bodies subjected to applied forces. It must eventually fail once the forces exceed some limit, since no material can be compressed beyond a certain minimum size, or stretched beyond a maximum size, without some permanent deformation or change of state. Many materials will noticeably deviate from Hooke’s law well before those elastic limits are reached.

On the other hand, Hooke’s law is an accurate approximation for most solid bodies, as long as the forces and deformations are small enough. For this reason, Hooke’s law is extensively used in all branches of science and engineering, and is the foundation of many disciplines such as seismology, molecular mechanics and acoustics. It is also the fundamental principle behind the spring scale, the manometer, and the balance wheel of the mechanical clock.

The modern theory of elasticity generalizes Hooke’s law to say that the strain (deformation) of an elastic object or material is proportional to the stress applied

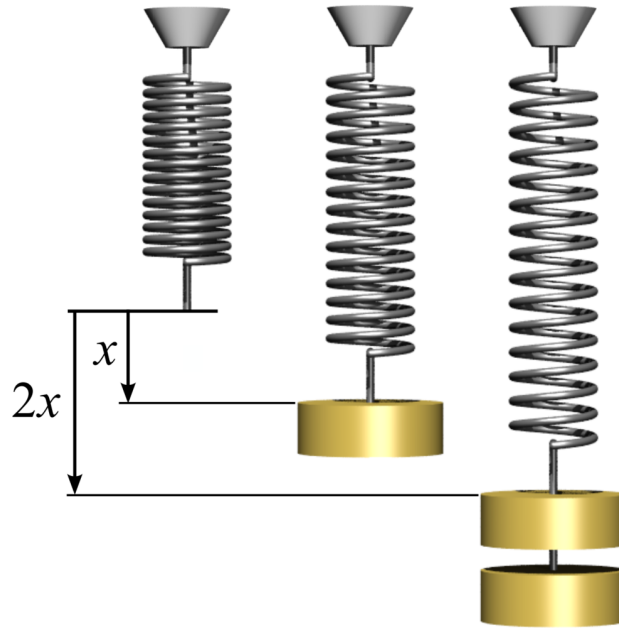


Figure 3.10: Hooke's law of spring

to it. However, since general stresses and strains may have multiple independent components, the “proportionality factor” may no longer be just a single real number, but rather a linear map (a tensor) that can be represented by a matrix of real numbers.

In this general form, Hooke's law makes it possible to deduce the relation between strain and stress for complex objects in terms of intrinsic properties of the material it is made of. For example, one can deduce that a homogeneous rod with uniform cross section will behave like a simple spring when stretched, with a stiffness k directly proportional to its cross-section area and inversely proportional to its length.

3.6.3 Stiffness Tensor for continuous media

The stresses and strains of the material inside a continuous elastic material (such as a block of rubber, the wall of a boiler, or a steel bar) are connected by a linear relationship that is mathematically similar to Hooke's spring law, and is often referred to by that name.

However, the strain state in a solid medium around some point cannot be described by a single vector. The same parcel of material, no matter how small, can be compressed, stretched, and sheared at the same time, along different directions. Likewise, the stresses in that parcel can be at once pushing, pulling

and shearing.

In order to capture this complexity, the relevant state of the medium around a point must be represented by two second-order tensors, the strain tensor ε (in lieu of the displacement X) and the stress tensor σ (replacing the restoring force F). The equation analogous to Hooke's spring law for continuous media is then

$$\boldsymbol{\sigma} = -\mathbf{C}\boldsymbol{\varepsilon} \quad (3.6.2)$$

The symmetry of the Cauchy stress tensor ($\sigma_{ij} = \sigma_{ji}$) and the generalized Hooke's laws:

$$\sigma_{ij} = c_{ijkl}\varepsilon_{kl} \quad (3.6.3)$$

imply that $c_{ijkl} = c_{jikl}$. Similarly, the symmetry of the infinitesimal strain tensor implies that $c_{ijkl} = c_{ijlk}$. These symmetries are called the minor symmetries of the stiffness tensor (\mathbf{C}). This reduces the number of elastic constants from 81 to 36.

Since the displacement gradient and the Cauchy stress are work conjugate, the stress-strain relation can be derived from a strain energy density function (U), thus

$$\sigma_{ij} = \frac{\partial U}{\partial \varepsilon_{ij}} \implies c_{ijkl} = \frac{\partial^2 U}{\partial \varepsilon_{ij} \partial \varepsilon_{kl}} \quad (3.6.4)$$

The arbitrariness of the order of differentiation implies that $c_{ijkl} = c_{klij}$. These are called the major symmetries of the stiffness tensor. This reduces the number of elastic constants to 21 from 36. The major and minor symmetries indicate that the stiffness tensor has only 21 independent components.

where \mathbf{C} is a fourth-order tensor (that is, a linear map between second-order tensors) called the stiffness tensor or elasticity tensor. The equation may also be written

$$\boldsymbol{\varepsilon} = -\mathbf{S}\boldsymbol{\sigma} \quad (3.6.5)$$

where the tensor \mathbf{S} , called the compliance tensor, represents the inverse of the linear map.

In a Cartesian coordinate system, the stress and strain tensors can be represented by 3×3 matrices

$$\boldsymbol{\varepsilon} = \begin{bmatrix} \varepsilon_{11} & \varepsilon_{12} & \varepsilon_{13} \\ \varepsilon_{21} & \varepsilon_{22} & \varepsilon_{23} \\ \varepsilon_{31} & \varepsilon_{32} & \varepsilon_{33} \end{bmatrix} \quad \boldsymbol{\sigma} = \begin{bmatrix} \sigma_{11} & \sigma_{12} & \sigma_{13} \\ \sigma_{21} & \sigma_{22} & \sigma_{23} \\ \sigma_{31} & \sigma_{32} & \sigma_{33} \end{bmatrix} \quad (3.6.6)$$

Being a linear mapping between the nine numbers σ_{ij} and the nine numbers ε_{kl} , the stiffness tensor \mathbf{C} is represented by a matrix of $3 \times 3 \times 3 \times 3 = 81$ real numbers C_{ijkl} . Hooke's law then says that

$$\sigma_{ij} = - \sum_{k=1}^3 \sum_{l=1}^3 C_{ijkl} \varepsilon_{kl} \quad (3.6.7)$$

where i and j are 1, 2, or 3.

All three tensors generally vary from point to point inside the medium, and may vary with time as well. The strain tensor ϵ merely specifies the displacement of the medium particles in the neighbourhood of the point, while the stress tensor σ specifies the forces that neighbouring parcels of the medium are exerting on each other. Therefore, they are independent of the composition and physical state of the material. The stiffness tensor \mathbf{C} , on the other hand, is a property of the material, and often depends on physical state variables such as temperature, pressure, and microstructure.

3.6.4 Principal stresses

Consider an infinitesimal element with its edges parallel to x , y and z axes, if only the x and y faces are subjected to stresses ($\sigma_z = 0$ and $\tau_{zx} = \tau_{xz} = \tau_{zy} = \tau_{yz} = 0$), it is called plane stress shown in Figure 3.11.

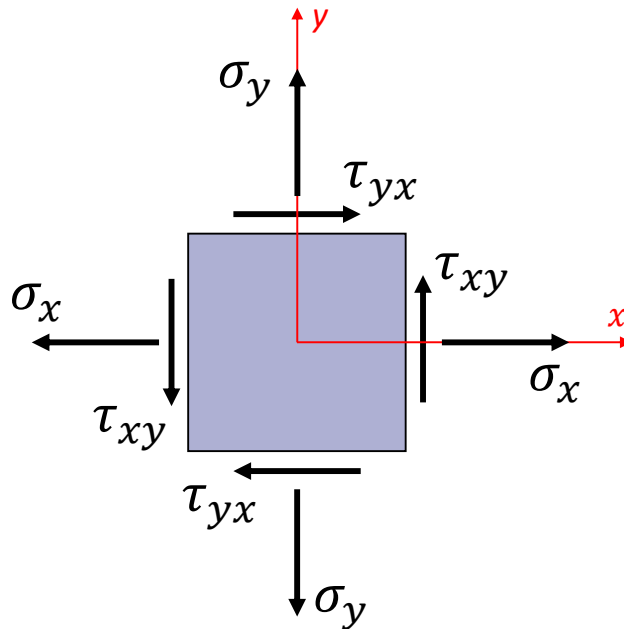


Figure 3.11: Plane stress element in 2D

Here, equal normal stresses act on opposite faces, shear stress τ has two subscripts, the first denotes the face on which the stress acts, and the second gives the direction of that face. τ_{xy} means acting on x face directed to y axis and τ_{yx} means acting on y face directed to x axis.

For design purpose, the largest positive and negative stresses are usually needed, the maximum and minimum normal stress are called the principal stresses.

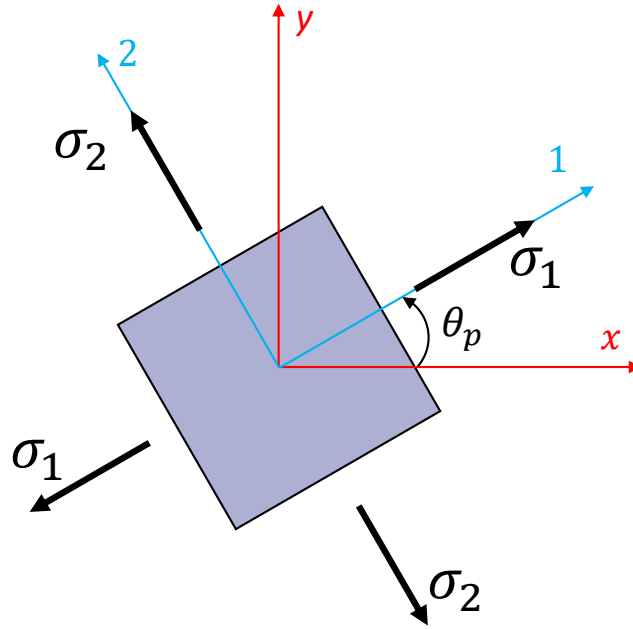


Figure 3.12: Principal plane stress

Consider the stress transformation equation

$$\sigma_{x1} = \frac{\sigma_x + \sigma_y}{2} + \frac{\sigma_x - \sigma_y}{2} \cos 2\theta + \tau_{xy} \sin 2\theta \quad (3.6.8)$$

to find the maximum normal stress, set $d\sigma_{x1}/d\theta = 0$:

$$\frac{d\sigma_{x1}}{d\theta} = -(\sigma_x - \sigma_y) \sin 2\theta + 2\tau_{xy} \cos 2\theta = 0 \quad (3.6.9)$$

which leads to:

$$\tan 2\theta_p = \frac{2\tau_{xy}}{\sigma_x - \sigma_y} \quad (3.6.10)$$

where θ_p (Figure 3.12) defines the orientation of the principal plane.

Equation (3.6.10) also leads to:

$$\begin{aligned} \cos 2\theta_p &= \frac{(\sigma_x - \sigma_y)}{2R} \\ \sin 2\theta_p &= \frac{\tau_{xy}}{R} \end{aligned} \quad (3.6.11)$$

where

$$R = \sqrt{\left(\frac{\sigma_x - \sigma_y}{2}\right)^2 + \tau_{xy}^2} \quad (3.6.12)$$

Substituting $\cos 2\theta_p$ and $\sin 2\theta_p$ into the Equation (3.6.8), the larger principal stress is obtained as

$$\sigma_1 = (\sigma_{x1})_{\max} = \frac{\sigma_x + \sigma_y}{2} + \sqrt{\left(\frac{\sigma_x - \sigma_y}{2}\right)^2 + \tau_{xy}^2} \quad (3.6.13)$$

and the smaller principal stress denoted by σ_2 is obtained as

$$\sigma_2 = \sigma_x + \sigma_y - \sigma_1 = \frac{\sigma_x + \sigma_y}{2} - \sqrt{\left(\frac{\sigma_x - \sigma_y}{2}\right)^2 + \tau_{xy}^2} \quad (3.6.14)$$

3.6.5 Von Mises stress

The von Mises stress is widely used to predict yielding of materials under any loading condition (Logan 2011). A material is said to start yielding when its von Mises stress reaches a critical value known as the yield strength. The von Mises stress is a scalar which can be deduced from the Cauchy stress tensor (Logan 2011)

$$\sigma_v^2 = \frac{(\sigma_{11} - \sigma_{22})^2 + (\sigma_{22} - \sigma_{33})^2 + (\sigma_{33} - \sigma_{11})^2 + 6(\sigma_{23}^2 + \sigma_{31}^2 + \sigma_{12}^2)}{2} \quad (3.6.15)$$

where the components $\sigma_{11}, \sigma_{22}, \sigma_{33}$ are orthogonal normal stresses, and $\tau_{12}, \tau_{23}, \tau_{13}$ the orthogonal shear stresses.

3.7 Failure theories

There are four failure theories: maximum shear stress theory, maximum normal stress theory, maximum strain energy theory, and maximum distortion energy theory. Out of these four theories of failure, the maximum normal stress theory is only applicable for brittle materials, and the remaining three theories are applicable for ductile materials. Of the latter three, the distortion energy theory provides most accurate results in majority of the stress conditions. The strain energy theory needs the value of Poisson's ratio of the part material, which is often not readily available. The maximum shear stress theory is conservative. For simple unidirectional normal stresses all theories are equivalent, which means all theories will give the same result.

- Maximum Shear stress Theory: This theory postulates that failure will occur if the magnitude of the maximum shear stress in the part exceeds the shear strength of the material determined from uniaxial testing.
- Maximum normal stress theory: This theory postulates that failure will occur if the maximum normal stress in the part exceeds the ultimate tensile

stress of the material as determined from uniaxial testing. This theory deals with brittle materials only. The maximum tensile stress should be less than or equal to ultimate tensile stress divided by factor of safety. The magnitude of the maximum compressive stress should be less than ultimate compressive stress divided by factor of safety.

- Maximum strain energy theory: This theory postulates that failure will occur when the strain energy per unit volume due to the applied stresses in a part equals the strain energy per unit volume at the yield point in uniaxial testing.
- Maximum distortion energy theory: This theory is also known as shear energy theory or von Mises-Hencky theory. This theory postulates that failure will occur when the distortion energy per unit volume due to the applied stresses in a part equals the distortion energy per unit volume at the yield point in uniaxial testing. The total elastic energy due to strain can be divided into two parts: one part causes change in volume, and the other part causes change in shape. Distortion energy is the amount of energy that is needed to change the shape.

For ductile materials there are two commonly used strength theories - the Maximum Shear Stress (MSS) or Tresca theory and the von Mises or Distortion Energy theory.

3.7.1 Maximum Shear Stress:

This states that failure occurs when the maximum shear stress in the component being designed equals the maximum shear stress in a uniaxial tensile test at the yield stress. The maximum shear stress is determined by

$$\tau_{\max} = \frac{S_y}{2n} \frac{\max(|\sigma_1 - \sigma_2|, |\sigma_2 - \sigma_3|, |\sigma_3 - \sigma_1|)}{2n} \quad (3.7.1)$$

where the yield strength S_y is reduced by the factor of safety n . Note for the plane stress state, σ_3 is zero.

3.7.2 Von Mises or Distortion Energy Theory

Distortion energy

For ductile metals and alloys materials, according to the Maximum Shear Stress failure theory (aka “Tresca”) the only factor that affects dislocation slip is the maximum shear stress in the material. This is really a 1-dimensional explanation; a single parameter (maximum shear stress) is the only thing that causes yielding. Therefore, the Tresca theory does work well in a 3D world. Nonetheless, a slight improvement upon Tresca’s theory has been made. That is, yielding (dislocation slip) is somewhat better explained (i.e. it is better supported by empirical data) by considering strain energy.

A material will deform if a load is applied. The units of energy are the products of forces and distances, so when a load is applied and the material deforms, energy is put into the material. The strain energy is the energy introduced into the material due to the loading. The strain energy density is normalized strain energy by unit volume. The area under a stress-strain curve is the energy per unit volume.

The strain energy is composed of two distinct forms – volume changes and distortion (angular change). Normal strains cause a change in volume, shear strains cause distortions. The total strain energy is the sum of distortion energy and volume energy:

$$U_{\text{total}} = U_{\text{distortion}} + U_{\text{volume}} \quad (3.7.2)$$

where U_{total} = total strain energy, $U_{\text{distortion}}$ = strain energy due to distortion, U_{volume} = strain energy due to volume change (aka hydrostatic strain energy).

The distortion energy are defined as:

$$U_{\text{distortion}} = U_{\text{total}} - U_{\text{volume}} \quad (3.7.3)$$

where U_{total} is total strain energy and U_{volume} is volume energy.

For general (3D) loading conditions, the total strain energy is given in terms of principal stresses and strains:

$$U_{\text{total}} = \frac{1}{2} (\epsilon_1 \sigma_1 + \epsilon_2 \sigma_2 + \epsilon_3 \sigma_3) \quad (3.7.4)$$

Using Hooke's law $\epsilon_1 = [\sigma_1 - \nu(\sigma_2 + \sigma_3)]/E$, $\epsilon_2 = [\sigma_2 - \nu(\sigma_3 + \sigma_1)]/E$, $\epsilon_3 = [\sigma_3 - \nu(\sigma_1 + \sigma_2)]/E$. The total strain energy equation 3.7.4 can be written in terms of stress only:

$$U_{\text{total}} = \frac{1}{2} E (\sigma_1^2 + \sigma_2^2 + \sigma_3^2 - 2\nu(\sigma_2\sigma_3 + \sigma_1\sigma_3 + \sigma_1\sigma_2)) \quad (3.7.5)$$

Remember that hydrostatic stress causes volume change and that it is invariant (hydrostatic stress is a scalar – it is not directionally dependent – therefore it does not vary depending upon axis orientation). The hydrostatic stress can be determined from the average magnitudes of the three principal stresses:

$$\sigma_{\text{hydrostatic}} = \sigma_{\text{ave}} = (\sigma_1 + \sigma_2 + \sigma_3) / 3 \quad (3.7.6)$$

$\sigma_{\text{hydrostatic}}$ is the stress condition that causes volume change. It is invariant. Let's consider a loading condition that was purely hydrostatic with magnitude of hydrostatic as calculated in equation 3.7.6. If the only stress in this material is $\sigma_{\text{hydrostatic}}$ then for this special loading condition the 3 principal stresses would be equal to $\sigma_{\text{hydrostatic}}$ ($\sigma_1 = \sigma_2 = \sigma_3 = \sigma_{\text{hydrostatic}}$). Equation 3.7.5 would become:

$$U = \frac{1 - 2\nu}{6E} (\sigma_{\text{hyd}}^2 + \sigma_{\text{hyd}}^2 + \sigma_{\text{hyd}}^2 + 2(\sigma_{\text{hyd}}^2 \sigma_{\text{hyd}}^2 + \sigma_{\text{hyd}}^2 \sigma_{\text{hyd}}^2 + \sigma_{\text{hyd}}^2 \sigma_{\text{hyd}}^2)) \quad (3.7.7)$$

For assumed purely hydrostatic loading condition in equation 3.7.7, there is no distortion energy ($U_{\text{distortion}} = 0$) so $U_{\text{total}} = U_{\text{volume}}$. Regardless of the existence of distortion energy or not, equation 3.7.7 – being based on the invariant hydrostatic stress – is the energy due to volume change, U_{volume} :

$$U = \frac{3(-2\nu)}{2E} \sigma_{\text{hyd}}^2 \quad (3.7.8)$$

Substituting equation 3.7.6 into 3.7.8 gives:

$$U_{\text{volume}} = \frac{1-2\nu}{6E} (\sigma_1^2 + \sigma_2^2 + \sigma_3^2 + 2\sigma_2\sigma_3 + 2\sigma_1\sigma_3 + 2\sigma_1\sigma_2) \quad (3.7.9)$$

To determine the strain energy due to distortion only (not volume change) Equation 3.7.9 is subtracted from Equation 3.7.5:

$$\begin{aligned} U_{\text{distortion}} &= U_{\text{total}} - U_{\text{volume}} \\ &= \frac{1}{2E} (\sigma_1^2 + \sigma_2^2 + \sigma_3^2 - 2\nu(\sigma_2\sigma_3 + \sigma_1\sigma_3 + \sigma_1\sigma_2)) \\ &\quad - \frac{1-2\nu}{6E} (\sigma_1^2 + \sigma_2^2 + \sigma_3^2 + 2\sigma_2\sigma_3 + 2\sigma_1\sigma_3 + 2\sigma_1\sigma_2) \\ &= \frac{1+\nu}{3E} \frac{(\sigma_1 - \sigma_2)^2 + (\sigma_2 - \sigma_3)^2 + (\sigma_3 - \sigma_1)^2}{2} \end{aligned} \quad (3.7.10)$$

The Maximum Shear Stress theory works well in predicting yielding of ductile materials since shear stress is the force that causes dislocation slip (aka plastic deformation). The shear stress caused by shear strains is: $\tau_{\text{max}} = (\sigma_1 - \sigma_3)/2$. It is the difference between principal stress divided by 2. Equation 3.7.10 combines the maximum shear stress in each of the 3 principal planes into a single equation.

The Distortion Energy failure theory is a bit more mathematically sophisticated than the Maximum Shear Stress failure theory, but is really very similar. Rather than considering only the maximum shear stress at a point, it combines the maximum shear stress at a point in the 3 principal planes. These two theories give very similar results, but Distortion Energy does match empirical data better.

Distortion energy failure theory

For uniaxial tensile loading (as is used to create a stress-strain curve), $\sigma_2 = \sigma_3 = 0$, and at the onset of yielding, $F/A = \sigma_1 = S_{\text{ys}}$ (at onset of yielding).

Therefore, for uniaxial loading substituting yield strength S_{ys} for σ_1 and $\sigma_2 = \sigma_3 = 0$ into equation 3.7.10

$$U_{\text{distortion}} = \frac{1+\nu}{3E} S_{\text{ys}}^2 \quad (3.7.11)$$

The Distortion Energy Theory states that when the distortion energy in a material equals or exceeds the distortion energy present at the onset of yielding in uniaxial loading tensile test for that material, the part will experience plastic

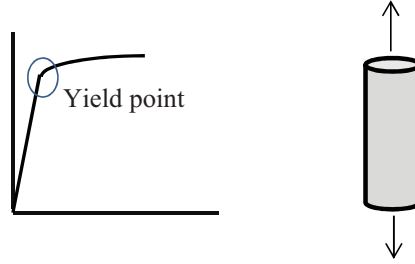


Figure 3.13: Yield point in uniaxial test

deformation (i.e. it will yield). In order to ensure plastic deformations do not occur, the following equation must be satisfied.

$$U_{\text{distortion,part}} \leq U_{\text{distortion,uniaxialtest}} \quad (3.7.12)$$

Letting the distortion energy in general 3D stress condition (Equation 3.7.10) equal to or less than the distortion energy in simple uniaxial loading (Equation 3.7.11) by substituting Equations 3.7.10 and 3.7.11 into Equation 3.7.12:

$$\frac{1 + \nu}{3E} \frac{(\sigma_1 - \sigma_2)^2 + (\sigma_2 - \sigma_3)^2 + (\sigma_3 - \sigma_1)^2}{2} \leq \frac{1 + \nu}{3E} S_{ys}^2 \quad (3.7.13)$$

$$\sigma_{\text{eff}} = \sqrt{\frac{(\sigma_1 - \sigma_2)^2 + (\sigma_2 - \sigma_3)^2 + (\sigma_3 - \sigma_1)^2}{2}} \leq S_{ys}$$

3.8 Common 3D printing material properties

There are an abundance of 3D printer filament materials available in the market, like the thermoplastics that comprise the common 3D printer filament types such as ABS and PLA and many other choices like nylon, polycarbonate, carbon fibre, polypropylene. The material properties of some of the common filaments are briefly introduced in the following:

1. Acrylonitrile butadiene styrene (ABS) is tough, non-toxic. It melts and becomes pliable at 220 degree Celsius. It's also water- and chemical-resistant. When heated, ABS will produce a slightly unpleasant smell, and the vapour can contain some nasty chemicals. ABS can be broken down by UV radiation, it isn't suitable for long-term outdoor use, as it loses its colour and becomes brittle. Because ABS is able to withstand high stress and temperature, items made of ABS can be frequently handled, dropped or heated. Examples include phone cases, high-wear toys, tool handles, automotive trim components, and electrical enclosures.

2. Polylactic acid (PLA) is a biodegradable thermoplastic, made from annually renewable resources like cornstarch or sugar-cane. PLA is a tough, resilient material with a matte, opaque quality and melts at between 180 and 200 degrees Celsius. It's generally considered an odourless filament though there is a slight smell when it is heated, but no toxic odours or vapour. PLA is generally the preferred option for low-cost 3D printers because it will stick well to a print base covered in white glue or blue painter's tape, which means that a heated print bed is not needed. PLA begins to deform at temperatures above 60 degrees Celsius, and it is not water or chemical resistant. PLA is usually for prints include models, low-wear toys, prototype parts and containers.
3. Nylon (a.k.a. Polyamide) is a tough material that has a very high tensile strength, therefore it can hold a lot of weight without breaking. It melts at 250 degrees Celsius which is hotter than many extruders can manage. And it is harder to get it to stick to the print bed than with ABS or PLA. Nylon generally requires both a heated print bed and white glue to stick while printing. Nylon is hygroscopic, meaning it absorbs moisture from the air causing a negative effect on printing. The general use of Nylon is to create tools, functional prototypes or mechanical parts like hinges, buckles or gears.
4. PETG is a Glycol Modified version of Polyethylene Terephthalate (PET), which is clearer, less brittle and easier to use than PET. It is a semi-rigid material with good impact resistance, but it has a slightly softer surface which makes it prone to scratch. It is sticky during printing, making it a poor choice for support structures but good for layer adhesion. Due to its flexibility, strength, temperature and impact resistance, PETG is an ideal filament for objects which might experience sustained or sudden stress, like mechanical parts, printer parts and protective components.
5. Polyvinyl alcohol (PVA) is soluble in water and is used to make supports that hold 3D prints in place. It melts at about 200 degrees Celsius, and can release some nasty chemicals if heated to higher temperatures. It can be used in a standard 3D printer extruder to form parts that support other objects, and it sticks to a heated, glass print bed well. Parts printed with PVA supports usually need to be placed in water for a few hours to dissolve PVA, leaving the rest of the insoluble print behind. This makes PVA filament a great choice to print complex models that require supports, or even models that include moving parts.

The density, ultimate strength and cost data come from [Simplify3D \(2019\)](#). The Young's modulus for PVA is given in [Yamaura et al. \(1986\)](#). The Young's modulus for Nylon is summarised in [Bainbridge \(2017\)](#).

In this thesis, all geometries are printed with ABS, therefore the material properties of ABS are used throughout all simulation, that is for Young's modulus $E = 2\text{GPa}$ and the ultimate strength $\sigma_s = 40\text{MPa}$.

Table 3.2: Common 3D printing material properties

Type	Young's Modulus GPa	Ultimate strength MPa	Density g/cm ³	Cost \$/kg
ABS	2.0	40	1.04	10 - 40
PLA	3.5	65	1.24	10 - 40
PVA	1.5 - 3.75	78	1.23	40 - 110
Nylon	3.3	40 - 85	1.3	20 - 60
PETG	2.2	53	1.23	20 - 60

3.9 Summary

In this chapter, the theory and formulation of CST, DKT and Beam elements have been introduced. The plate element is formed by assembling the CST and DKT elements together. In order to avoid the rank deficiency of plate element, drilling degree is also introduced here. Since von Mises stress (equivalent stress) is the criteria used to determine if the structural is sound / or if there exists any fracture in the object, this chapter also presents details of the theory of stress and failure analysis and also the formulation of von Mises stress. Finally, this chapter also includes an introduction of 3D printing materials where the ultimate material strength of ABS(40MPa) is chosen as the stress limit throughout this research.

Chapter 4

Edge stiffened structures

4.1 Overview

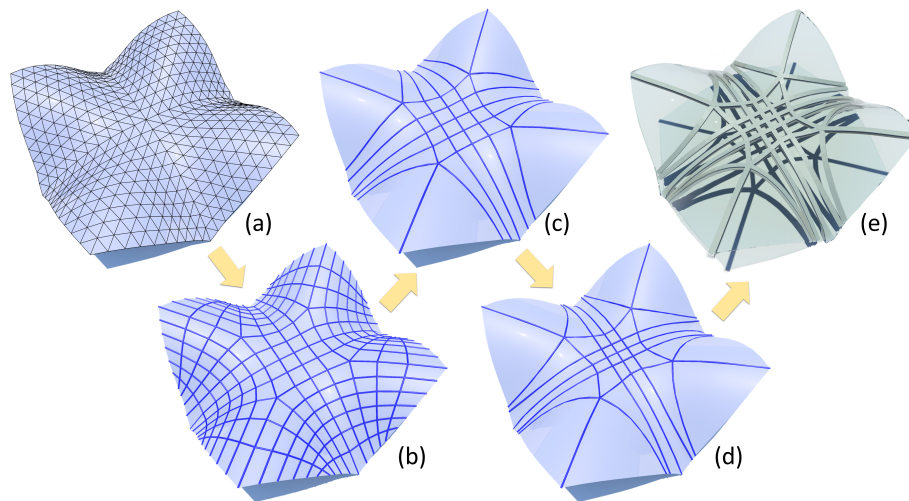


Figure 4.1: System overview: Given an input surface (a), a dense rib network (b) is generated, followed by a simplification process to remove the ribs with little contributions (c). Then a rib flow optimization is performed to adjust the layout of ribs (d). Finally, the cross-section of ribs is optimized using hyperelliptic T-section (e).

To enhance freeform surface with attached rib network, the first approach composed of four stages (see Figure 4.1) is proposed in this research: 1) rib network initialization, 2) rib network simplification, 3) rib flow optimization and 4) rib cross-section optimization.

4.2 Pipeline of the edge stiffened optimisation

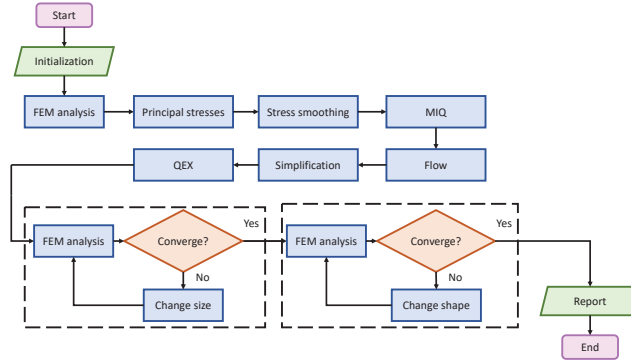


Figure 4.2: The pipeline of edge stiffened structure optimization

Rib Network Initialization Given a surface with specified thickness and boundary conditions, Finite Element Analysis (FEA) is used to determine the stress field. The stress field is then converted to principal stress field, which shows desirable material continuity and encodes the optimal topology. Using this principal stress field, a global parametrization is calculated, and then a quad-mesh whose edges align with orthogonal directions is extracted. Based on singular vertices and connectivity of the quad-mesh, the mesh is further represented as a rib network which consists of tree-like, circular and curved rib elements.

Rib Network Simplification Since the mesh extracted from stress analysis and parametrization is a dense mesh, some ribs may have little contributions to the overall shell. Therefore a simplification step is involved here by dropping some rib elements with less contributions to the overall strain energy further.

Rib Flow Optimization The removal of ribs of the previous step will alter the stress field of the initial dense rib network. Hence a further adjustment on the layout of remaining ribs is needed to flow ribs on the surface and reduce total strain energy.

Rib Cross-section Optimization The final step of the framework is to optimize the rib cross-section with the goal of satisfying material strength requirement with least material usage. The size of cross-section is first roughly determined by using rectangular section. The material usage is further improved by replacing rectangular section with hyperelliptic T-section, as it moves more materials away from the surface to make the hyperelliptic T-section have more capability to resist bending. The shape of hyperelliptic T cross-section is then optimized to find the optimal material distribution.

4.3 Rib-shell Structure

4.3.1 Rib-shell Structure

Given an input mesh \mathcal{M}^0 , the rib-shell structure \mathcal{H} consists of a thin shell \mathcal{S} and ribs \mathcal{R} , as shown in Figure 4.3. \mathcal{S} is a thin shell between \mathcal{M}^0 and its offset \mathcal{M}^1 with a thickness t . \mathcal{R} is composed of a set of ribs $\mathcal{R} = \{R_i, i = 1, 2, \dots, n\}$. Each rib is closely attached to one or both sides of \mathcal{S} and contains a set of consecutive rib points $R_i = \{R_{ij}, j = 1, 2, \dots, n_i\}$, where the subscript i indicates the i^{th} rib, and ij indicates the j^{th} node of the i^{th} rib.

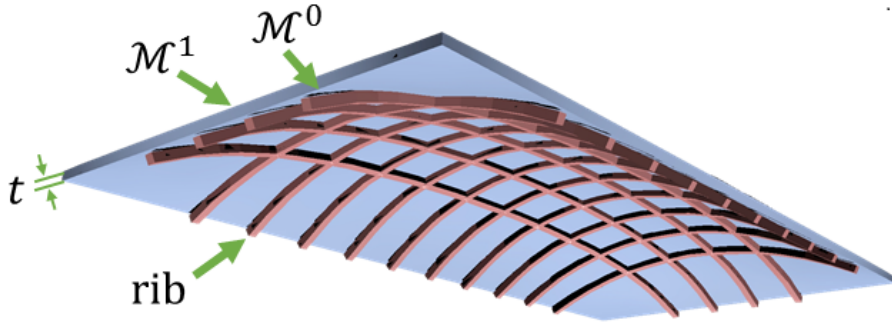


Figure 4.3: Illustration of the rib-shell structure.

4.3.2 Rib Network

All the ribs \mathcal{R} in a rib-shell structure compose a rib network \mathcal{N} which contains three fundamental element sets, i.e., *curved* \mathcal{R}^c , *circular* \mathcal{R}^o and *tree-like* \mathcal{R}^t rib element sets. A rib element consists of ribs and has semantic information. Usually the tree-like rib element plays a more important role in reinforcing a shell. And circular and curved rib elements enhance local stiffness and strength and assist to increase global performance of rib-shell structures. Figure 4.4 shows the three types of rib elements in a rib network. Note that curved rib element is the fundamental rib element which is also called rib for convenience. A tree-like rib element consists of several curved rib elements, and a circular rib element can be regarded as a curved rib element whose two ends meet at a same point.

4.3.3 Rib Cross-section

A wide range of profiles of cross-section for ribs have been applied in engineering. Among them, T-shaped cross-section is rather popular due to some practical advantages. T-section offers greater and significantly more resistance to bending. And the material is present where it should be and in the right quantities (Lam & Santhikumar 2003). This makes the rib more economical and lighter and in turn makes a rib-shell structure even more economical. However, the commonly

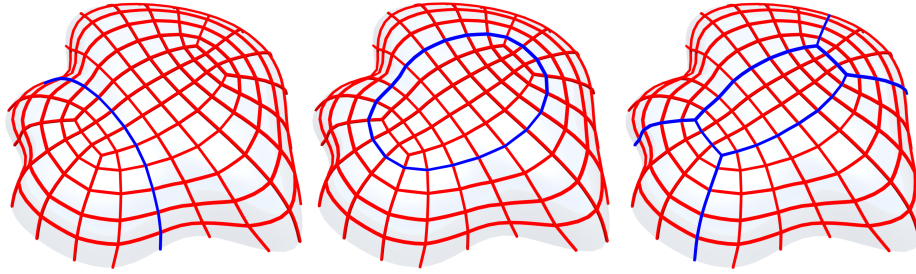
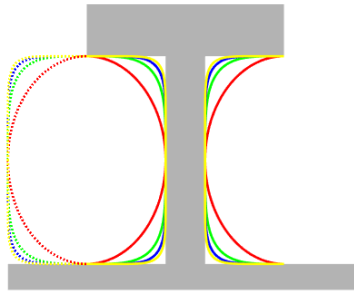


Figure 4.4: From left to right: curved, circular and tree-like rib elements. The right tree-like rib element consists of eight curved ribs.

used right-angled T-section has a stress concentration on the corner which results in a localized increase in stress and causes cracks or even catastrophic failure (Kokcharov & Burov 2013). To avoid potential stress concentration at sharp



corners, an improved hyperelliptic T-section is applied to rib section. The formulation of a hyperellipse with order $n(n > 2)$ can be formulated as follows

$$\left| \frac{x}{a} \right|^n + \left| \frac{y}{b} \right|^n = 1, \quad (4.3.1)$$

where a and b are the semi-major and semi-minor axes, respectively. As the order n increases, the hyperellipse converges to a rectangle and the cross-section of rib tends to be a standard right-angled T-section as shown in the inset.

Hyperelliptic T-section inherits the advantages of right-angled T-section and improves stress concentration at the same time. To show stress distribution improvement of hyperelliptic T-section over right-angled one, an FEA simulation of two types of ribs is performed. For the test case, both ends of the rib are fixed, and same loads are imposed on the middle of the mesh. The results in Figure 4.5 indicate hyperelliptic T-section has better performance and can prevent from stress concentration to some extent.

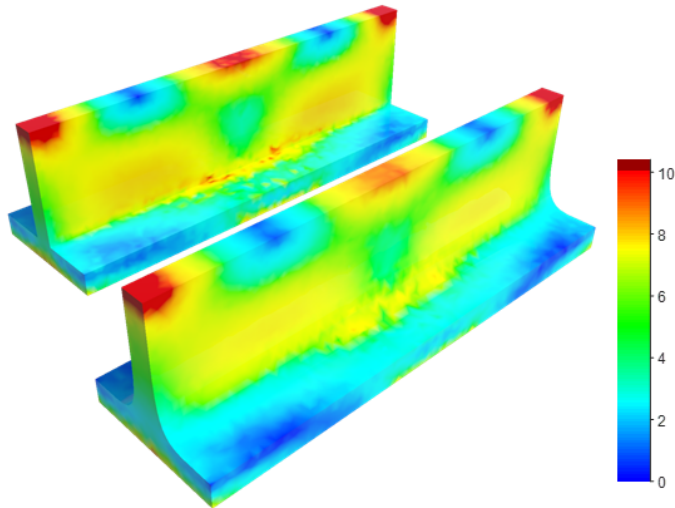


Figure 4.5: Hyperelliptic (a) and right-angled (b) T-section. Colour encodes the von Mises stress. The stress of right-angled T-section in the back is much higher than that of hyperelliptic T-section.

4.4 Rib Network Generation

4.4.1 Principal Stress Calculation

Principal stresses are the components of a stress tensor when the basis is changed in such a way that the shear stress components become zero. The rib network generation is based on principal stresses of the original shell structure, more precisely, placing ribs along principal stress directions. The stress tensor σ has three real eigenvalues $\lambda_1, \lambda_2, \lambda_3$ and three mutually orthogonal eigenvectors $\mathbf{e}_1, \mathbf{e}_2, \mathbf{e}_3$, satisfying $\sigma \mathbf{e}_i = \lambda_i \mathbf{e}_i (i = 1, 2, 3)$. Therefore, by multiplying a coordinate transformation matrix to transform the original coordinate system to the coordinate system with axes $\mathbf{e}_1, \mathbf{e}_2, \mathbf{e}_3$, the stress tensor now only has three normal components, i.e., principal stresses and three eigenvectors which are principal stress directions.

Principal stress directions are useful as they indicate the trajectories of internal forces and, therefore naturally encode the optimal topology for any structure for a given set of boundary conditions (Adriaenssens et al. 2014). Here, principal stress directions are used to guide the construction of rib layout and align ribs with these directions. By doing so, the ribs can best reinforce shells under external loads.

4.4.2 Quad-mesh Extraction

Based on the principal stress field defined on the surface of input mesh, a global parametrization of the surface is computed using the MIQ method (Bommes

et al. 2009). Next a quad-mesh from the input surface is extracted by the method of QEx (Ebke et al. 2013). Since edges of the resulted quad-mesh align with the principal stress directions of the surface, the dense rib network can be initialized from the quad-mesh.

Principal Stress Field Smoothing To get a better parametrization result, the principal stress field is smoothed with the introduction of smoothness energy. The smoothness energy is defined based on the method in Kälberer et al. (2007), which blends a smoothness energy with an alignment term:

$$E_{sm} = \lambda \sum_{e_{ij} \in E} \cos 4(\theta_i + r_{ij} - \theta_j + \alpha_i - \alpha_j) + (1 - \lambda) \sum_{f_i \in F} \alpha_i^2. \quad (4.4.1)$$

Here θ_i and θ_j are stress directions in local frames of face f_i and f_j , respectively, and r_{ij} is the angle between both local frames. The variables α_i and α_j are the direction deviations on face f_i and f_j , respectively. The rightmost term is the penalty of large deviations which keeps the resulting cross field aligning with the original stress field. The factor λ determines if there is more emphasis on smoothing or alignment, and it is set to be 0.8 here. Figure 4.6 provides a comparison of stress field before and after smoothing.

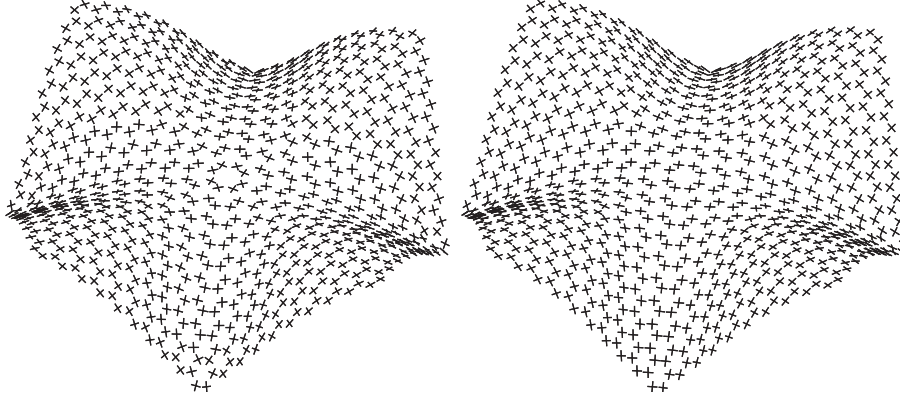


Figure 4.6: Left: principal stress directions. Right: principal stress directions after smoothing.

Global Parametrization In the global parametrization, each vertex of the input mesh is assigned a (u, v) parameter value so that its iso-parameter lines on the surface are locally aligned with the principal stress field. The optimal parametrization is obtained by minimizing the following energy function

$$E_T = \sum_{f_i \in F} A_{f_i} (\|\rho \nabla u - \mathbf{u}_{f_i}\|^2 + \|\rho \nabla v - \mathbf{v}_{f_i}\|^2), \quad (4.4.2)$$

where ρ is a global scaling parameter which controls the length of edges in the resulting quad-mesh. And \mathbf{u}_{f_i} and \mathbf{v}_{f_i} are two orthogonal vectors in face

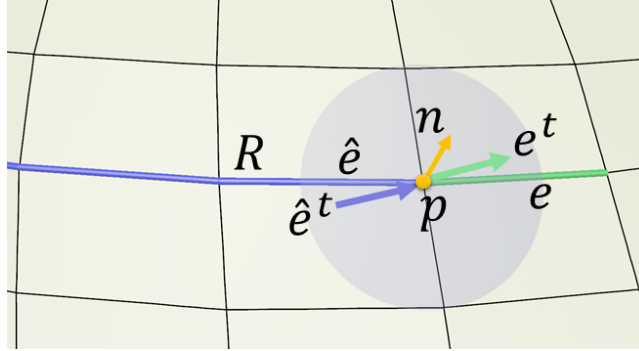
f_i corresponding to the cross field directions. The scalar A_{f_i} is the area of face f_i .

Quad-mesh Extraction and Processing As long as the global parametrization result is found, a quad-mesh can be generated by just using the method of QEx (Ebke et al. 2013). The quad-mesh is further smoothed using a simple Laplacian smoothing method, and then projected to the original triangle mesh along vertex normal directions.

For some complex surfaces, the output quad-mesh may contain many singularities, which is harmful to the rib generation process. Therefore Peng’s connectivity editing operations (Peng et al. 2011) is used to explicitly move and merge singularities.

4.5 Rib Network Initialization

Given a quad-mesh $\mathcal{M}(V, E, F)$, consecutive edges that don’t bend too much are traced and the resulting curve is taken as a rib. For a rib R , it reaches an



adjacent edge e intersecting at point p with normal n . To compute the angle between the rib R and e , edge \hat{e} adjacent to e in rib R as well as edge e are projected onto the tangent plane passing the point p perpendicular to the normal n . Then the angle between the rib R and edge e can be calculated by the two projected edge \hat{e}^t and e^t as follows

$$\angle(R, e) = \arccos\left(\frac{\hat{e}^t \cdot e^t}{\|\hat{e}^t\| \|e^t\|}\right), \quad (4.5.1)$$

where $\hat{e}^t = \hat{e} - (\mathbf{n} \cdot \hat{e})\mathbf{n}$ and $e^t = e - (\mathbf{n} \cdot e)\mathbf{n}$ are the projections of edges \hat{e} and e on the tangent plane, respectively.

When tracing a rib, a user-specified parameter ϕ is used to control the degree of bending. The algorithm to trace a rib is described in Algorithm 1.

During the rib network tracing process, tree-like rib elements are first extracted by tracing from the edges originated from the singularities of the quad-mesh. If a rib reaches a new singularity, the tracing will span from here and continue until it reaches boundary or meeting any visited nodes. After all the singularities

Algorithm 1: $\{R, \mathcal{E}\} = \text{ribTracer}(\mathcal{M}, \mathcal{E}, e)$

Input: Quad-mesh \mathcal{M} , edge set \mathcal{E} and starting edge e ;**Output:** Rib R and new edge set \mathcal{E} ;

```
1 add  $e$  into  $R$ ;  
2 while true do  
3    $best\_align = +\text{inf}$ ;  
4    $e\_best = -1$ ;  
5   foreach  $e\_next$  adjacent to rib  $R$  do  
6     if  $e\_next \cap R$  is singularity then  
7       | return;  
8     end  
9     if  $e\_next \notin \mathcal{E}$  then  
10    | continue;  
11    end  
12    if  $\angle(R, e\_next) < best\_align$  then  
13    |  $best\_align = \angle(R, e\_next)$ ;  
14    |  $e\_best = e\_next$ ;  
15    end  
16  end  
17  if  $e\_best \neq -1$  and  $best\_align < \phi$  then  
18  | add  $e\_best$  into  $R$ ;  
19  | remove  $e\_best$  from  $\mathcal{E}$ ;  
20  else  
21  | break;  
22  end  
23 end
```

are processed, namely, tree-like rib elements are all extracted, the rest ribs will either be a circular rib or a curved rib depending on if it meets starting point.

The complete rib network extraction process is described in Algorithm 2. Since the edges of quad-mesh align with the principal stress directions, the resultant rib network also lies along these directions. Once a dense rib network is obtained, all the ribs are projected back to the input mesh to make them on the final shell.

4.6 Rib Network Simplification

For the dense rib network generated from quad-mesh, using all the ribs will be wasteful and unnecessary as some ribs have little contribution to the shell. Moreover, since main deformations in shell structures are bending, a thick rib has much larger second moment of area than several thin ribs whose total cross-section area is same as the thick rib. Therefore, a sparse thick rib structure resists bending deformations more effectively than a dense thin rib structure.

Algorithm 2: $\{\mathcal{N}\} = \text{ribNetworkTracer}(\mathcal{M})$

Input: Quad-mesh $\mathcal{M}(V, E, F)$;
Output: Rib network $\mathcal{N} = \mathcal{R}^c \cup \mathcal{R}^o \cup \mathcal{R}^t$;

- 1 create rib element sets $\mathcal{R}^c, \mathcal{R}^o, \mathcal{R}^t$, and create set \mathcal{E} and \mathcal{S} ;
- 2 add all edges in E into \mathcal{E} and singularities of \mathcal{M} into \mathcal{S} ;
- 3 **while** \mathcal{S} is not empty **do**
- 4 create \mathbb{S} and move a singularity s in \mathcal{S} into \mathbb{S} ;
- 5 create tree-like rib element R^t ;
- 6 **while** \mathbb{S} is not empty **do**
- 7 **foreach** edge e in \mathcal{E} originated from s **do**
- 8 $\{R, \mathcal{E}\} = \text{ribTracer}(\mathcal{M}, \mathcal{E}, e)$;
- 9 **if** R has singularity s' and $s' \in \mathcal{S}$ **then**
- 10 | move s' from \mathcal{S} into \mathbb{S} ;
- 11 **end**
- 12 add R into R^t ;
- 13 **end**
- 14 add R^t into \mathcal{R}^t ;
- 15 **end**
- 16 **end**
- 17 **while** \mathcal{E} is not empty **do**
- 18 choose an arbitrary starting edge e ;
- 19 $\{R, \mathcal{E}\} = \text{ribTracer}(\mathcal{M}, \mathcal{E}, e)$;
- 20 **if** R is a loop **then**
- 21 | add R into \mathcal{R}^o ;
- 22 **else**
- 23 | add R into \mathcal{R}^c ;
- 24 **end**
- 25 **end**

To measure the contribution of each rib element to the shell, the total strain energy U_0 of the pure shell structure is calculated using $U_0 = \mathbf{u}_0^T \mathbf{K}_0^s(t) \mathbf{u}_0$ with shell thickness t . Then given a certain volume V of material, the strain energy of shell together with rib element i is computed as

$$U_i = \mathbf{u}_i^T (\mathbf{K}_0^s(t) + \mathbf{K}_i^r(w_i, h_i)) \mathbf{u}_i. \quad (4.6.1)$$

Here w_i and h_i are the width and height of rib element. An assumption here is that the cross-sectional shape of all the ribs is square to make it simpler. That is to say, $w_i = h_i$ and $l_i w_i h_i = V$ with total rib length l_i . And now the contribution for rib element i is defined as

$$C_i = 1 - \frac{U_i}{U_0}. \quad (4.6.2)$$

That means the more strain energy reduces, the more important the rib element is. Based on strain energy contribution of each rib, any rib element whose

contribution is less than a user-specified threshold value γ is discarded. Figure 4.7 shows an example of rib network simplification.

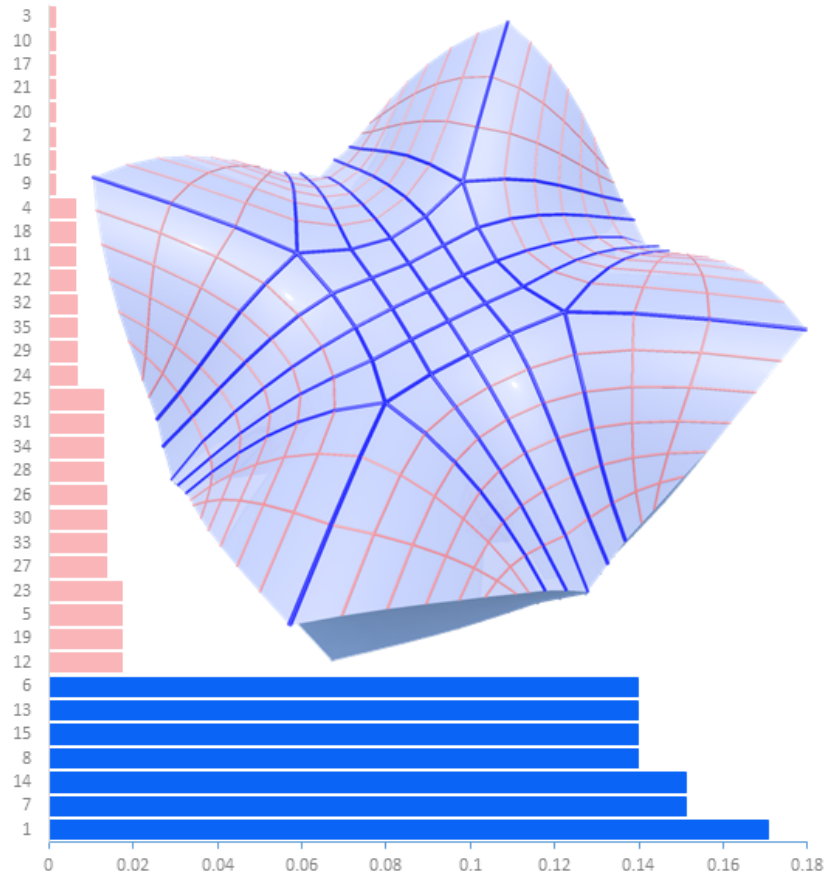


Figure 4.7: Rib network simplification of Guscio. The histogram on the left illustrates the contribution of each rib element. The resultant simplified rib network is coloured in blue. Light orange rib elements are dropped.

4.7 Rib Network Optimization

4.7.1 Rib Flow Optimization

The removal of rib elements with little contribution affects the rest of ribs as this process changes the rib network. To ensure after removal processing the rib network still follow the stress field, a flow step is introduced to readjust the layout of the rib network. Since the rib network is extracted from a quad-mesh \mathcal{M} , whose vertex positions are denoted as $\mathbf{p}_v^0, v = 1, 2, \dots, |V|$, each rib point

R_{ij} has a unique integer v_{ij} corresponding to a vertex in quad-mesh. And for each point R_{ij}^0 in a rib, it has two moving directions as \mathbf{d}_{ij}^+ and \mathbf{d}_{ij}^- . Assume each rib point has a signed moving distance δ_{ij} along its actual moving direction

$$\mathbf{d}_{ij} = \begin{cases} \mathbf{d}_{ij}^+ & \delta_{ij} \geq 0 \\ \mathbf{d}_{ij}^- & \delta_{ij} < 0 \end{cases} . \quad (4.7.1)$$

The new position of each vertex of the quad-mesh can be solved by the following equation

$$\mathbf{p}_v = \mathbf{p}_v^0 + \sum_{v_{ij}=v} |\delta_{ij}| \mathbf{d}_{ij} . \quad (4.7.2)$$

The rib point position is updated by $R_{ij} = \mathbf{p}_{v_{ij}}$ to keep the correspondence of ribs and quad-mesh. And the goal of rib flow optimization is to minimize the total strain energy of rib-shell structure by optimizing the position of each rib point, which is dependent on the moving distance δ_{ij} .

Rib Moving Directions Considering most rib points in quad-mesh have a valence of four, for these points, the moving directions are defined as the two outgoing edge vectors with unit length, as shown in Figure 4.8. And the maximum moving distance for each direction is defined as the half of corresponding edge length L_{ij}^+ and L_{ij}^- . For singularity points whose valence are not four, the

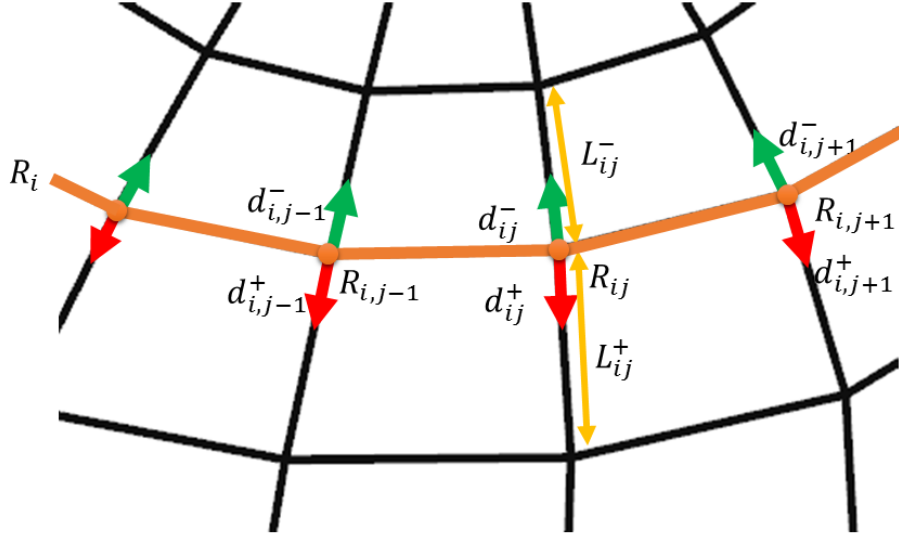


Figure 4.8: Moving directions for rib point with degree 4.

moving directions are ambiguous to define. An alternative way is to update their positions from a linear combination of their neighbouring vertex positions.

Problem Formulation The rib flow optimization is aimed at minimizing the total strain energy by changing the rib point positions. To keep the smoothness of ribs after flowing, a smoothing term is added by modifying the standard

mid-point scheme (e.g., $\mathbf{p}_{i-1} + \mathbf{p}_{i+1} \approx 2\mathbf{p}_i$) so that it reflects the varying density of rib points. The smoothness of rib R_i is defined as

$$S_i = \sum_{j=2}^{n_i-1} \|(1 - u_j)R_{i,j-1} + u_j R_{i,j+1} - R_{ij}\|_2^2, \quad (4.7.3)$$

and the weight is define as

$$u_j = \frac{\|R_{ij}^0 - R_{i,j-1}^0\|_2}{\|R_{ij}^0 - R_{i,j-1}^0\|_2 + \|R_{i,j+1}^0 - R_{ij}^0\|_2}. \quad (4.7.4)$$

Hence the objective function of rib flow optimization can be written as follows:

$$\min_{\delta_{ij}} \frac{1}{2} \mathbf{u}^\top \mathbf{K}(\delta_{ij}) \mathbf{u} + \lambda^r \sum_{i=1}^n S_i. \quad (4.7.5)$$

Here λ^r is the weight of smoothing term and is set as 30 in the research.

The moving distances are constrained to corresponding edge lengths

$$-\frac{L_{ij}^-}{2} \leq \delta_{ij} \leq \frac{L_{ij}^+}{2}. \quad (4.7.6)$$

Figure 4.9 gives the results of rib flow optimization. And the strain energies of the shell for Guscio and Botanic reduced about 1.32% and 3.57%, respectively.

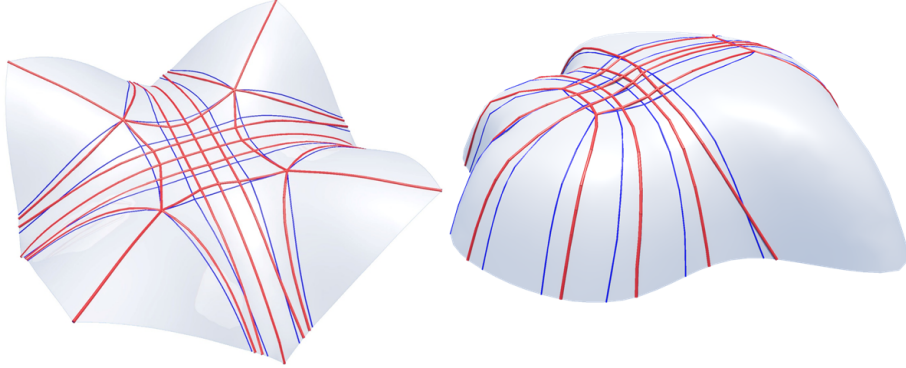


Figure 4.9: Rib network before (blue) and after (red) rib flow optimization for Guscio (left) and Botanic (right).

4.8 Cross-Section Optimization

The aim of rib cross-section optimization is to minimize the material usage of ribs while guaranteeing the overall physical performance of rib-shell structure. As illustrated before, hyperelliptic T-section has many advantages. However,

the calculation becomes a headache. To tackle this problem, the cross-section is first optimized as a rectangle with two variables: width and height. Then based on the rectangular ribs, the cross-sectional shape is further optimized to form a hyperelliptic T-section.

4.8.1 Size Optimization

For point R_{ij} of rectangle cross-sectional shape of each rib, the width and height are w_{ij} and h_{ij} , respectively. The goal is to minimize the rib volume while achieving certain stiffness requirement. The objective function is a combination of total rib volume and a smoothing energy. The smoothing term S_i^w and S_i^h are Laplacian smoothing of width and height along the ribs, and λ^w and λ^h are their weights, respectively. And the formulation of rib size optimization is as follows:

$$\begin{aligned} \min_{\{w_{ij}, h_{ij}\}} \quad & \sum_{i=1}^n (V_i + \lambda^w S_i^w + \lambda^h S_i^h) \\ \text{s.t.} \quad & \begin{cases} \sigma_{\max} \leq \bar{\sigma}, \\ \underline{s} \leq w_{ij} \leq \bar{s}, \\ \underline{s} \leq h_{ij} \leq \bar{s}, \\ \frac{1}{r} \leq \frac{w_{ij}}{h_{ij}} \leq r. \end{cases} \end{aligned} \quad (4.8.1)$$

Here σ_{max} is the maximum von Mises stress, and $\bar{\sigma}$ is the maximum allowable stress which reflects the strength limit of material. \underline{s} and \bar{s} are the lower and upper bound of rib size. And the last constraint keeps the ratio of width and height staying in a reasonable range. This optimization problem calculates the minimum needed material to keep the shell in a safe state.

Shape Optimization

Second Moment of Area The resistance of bending for a rib can be evaluated using second moment of area:

$$I_x = \iint_A y^2 dA, \quad (4.8.2)$$

$$I_y = \iint_A x^2 dA, \quad (4.8.3)$$

where A is cross-sectional domain we concern. Equation 4.8.2 and 4.8.3 indicate that for a shape with a given area, the more geometry accumulates away from z -axis the larger bending resistance it possesses. This provides a more convincing reason to use T-section from the perspective of mechanics principle.

Hyperelliptic T-Section A hyperelliptic T-section is formed from a rectangular rib by removing two halves of a hyperellipse from a rectangle as shown in the Figure 4.10. So the area of the cross-section is the difference between the area of the rectangle and the area of the hyperellipse. And the area of the hyperellipse can be explicitly expressed in terms of the gamma function (Rosin 2000).

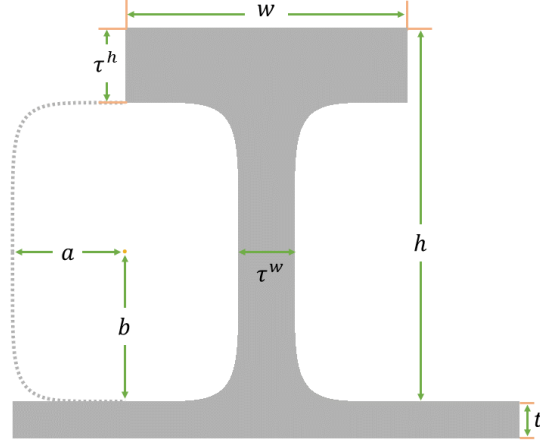


Figure 4.10: Hyperelliptic T-Section attached to a shell with thickness t .

Shape Optimization The goal of cross-sectional shape optimization is to further reduce material usage from a rectangular rib while maintaining the mechanical stiffness of the rib-shell structure under external loads. So the objective function is also the volume of ribs

$$\min \sum_{i=1}^n V_i(w_{ij}, h_{ij}, a_{ij}, b_{ij}), \quad (4.8.4)$$

where $V_i(w_{ij}, h_{ij}, a_{ij}, b_{ij})$ is the volume of rib i with hyperelliptic T-section. w_{ij} and h_{ij} are width and height of the bounding box of cross-section, which are near the original rectangular cross-section by the following constraints:

$$\begin{aligned} |w_{ij} - w_{ij}^*| &\leq \epsilon_w w_{ij}^*, \\ |h_{ij} - h_{ij}^*| &\leq \epsilon_h h_{ij}^*. \end{aligned} \quad (4.8.5)$$

Where w_{ij}^* and h_{ij}^* are width and height of rectangular rib from rib size optimization. ϵ_w and ϵ_h are parameters that control the change of rib width and height, respectively. And furthermore the parameters of hyperellipse are constrained by shell thickness t as follows:

$$\begin{aligned} w_{ij} &= 2a_{ij} + \tau^w, \\ h_{ij} &= 2b_{ij} + \tau^h, \end{aligned} \quad (4.8.6)$$

where τ^w and τ^h are flange and web thicknesses of the hyperelliptic T-section, respectively. To ensure the strength of the T-section, we further constrain τ^w and τ^h by the shell thickness t using the following equations:

$$\begin{aligned} t &< \tau^w < w_{ij}, \\ t &< \tau^h < h_{ij}. \end{aligned} \quad (4.8.7)$$

To guarantee the mechanical performance of each rib, the second moment of area of rib i can't be less than original rib with rectangular cross-section.

$$\begin{aligned} I_x(i) &\geq I_x^*(i), \\ I_y(i) &\geq I_y^*(i). \end{aligned} \tag{4.8.8}$$

Here $I_x^*(i)$ and $I_y^*(i)$ are the second moment of area for original rectangular rib i . And $I_x(i)$ and $I_y(i)$ are the second moment of area for hyperelliptic T-sectional rib i .

From the analysis above, the cross-sectional shape optimization can be formulated as a non-linear optimization problem with objective function Equation 4.8.4 and constraint Equations 4.8.5, 4.8.6, 4.8.7 and 4.8.8.

4.9 Results

The algorithm is implemented on a desktop PC with an Intel I5 CPU and 8G memory. The FEA and initial rib network generation process are implemented in C++, while the rib optimization process is implemented with Matlab. The non-linear optimization problems (Equations 4.7.5, 4.8.1 and 4.8.4) can be solved using the Interior Point Method (Nocedal & Wright 2006) where the gradients are estimated using finite differences.

Parameters Setting In the experiments the models are all scaled such that the maximum edge length of bounding box is 100. The shell thickness t is set to 1.2. The lower and upper bounds of rib size are set as 0.8 and 8, respectively. The maximum ratio of rib width and height r is set as 4. Note that the unit is millimetre. The scaling parameter ρ for MIQ is between 18 and 30 in our method. And smoothing weights λ^w and λ^h are both set as 10. And parameters ϵ^w and ϵ^h are set as 0.2 here. The maximum allowable von Mises stress $\bar{\sigma}$ is set as 40 according to the yield strength of plastic (42 MPa). And the angle deviation threshold ϕ in Algorithm 1 is set as $\pi/3$. The external loads are imposed as gravity by default.

Discussions

Choice of Hyperelliptic Order As the order of hyperellipse in Equation 4.3.1 increases, it looks apparently like a rectangle with rounded corners. The performances of hyperelliptic T-section with different orders are shown in Figure 4.11. In the figure, only moments for bending resistance in height direction are shown as they are more important than moments in width direction for shell structures. It can be seen that with the growth of orders, both values of hyperelliptic T-section are getting closer to corresponding values of right-angled T cross-section. But the computational cost of hyperelliptic shape rises as the increase of orders. Consequently the order is chosen to be 6 where the changes of area and moment properties are small and the order is not too large.

Iteratively Alternate Optimization of Rib Flow and Cross-section The rib flow optimization and cross-section optimization can be performed alternately

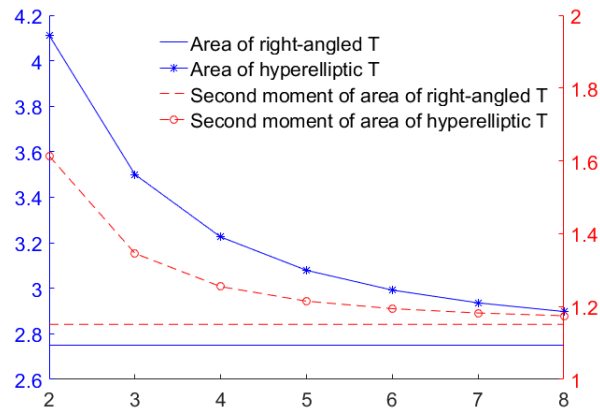


Figure 4.11: Area (blue) and second area moments (red) about orders of right-angled and hyperelliptic T-sections.

and iteratively. But it turned that after a round of rib flow and cross-section optimization, the effect of rib flow in the next step is pretty minor. As a consequence, the rib flow and cross-section optimization are not done iteratively

Comparisons

Comparison Between Concentrated and Distributed Load The final rib-shell structure depends on the principal stress directions which are determined by external load conditions used in FEA. Results from distributed and concentrated loads are compared and shown in Figure 4.12, and turned out that under the concentrated external loads, ribs tend to be denser near the region of loading nodes.

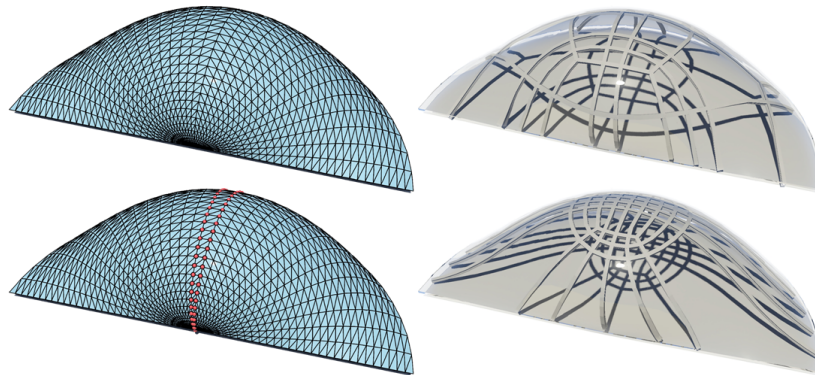


Figure 4.12: Top: distributed loads (gravity). Bottom: concentrated loads (load nodes are marked as red).

Comparison to Grid-shell Structure Figure 4.13 shows the results of Voronoi grid-shell (Pietroni et al. 2015) and self-support quad grid-shell (Vouga et al. 2012) structures for visual comparison. The rib-shell structure is simpler and easier to fabricate compared with the other two which are assembled by a mass of beams. Moreover, rib-shell structure achieves better global structural stability especially at the centre. Unfortunately, due to the lack of sufficient information, like boundary conditions, grid size and so on, no numeric comparison is made.

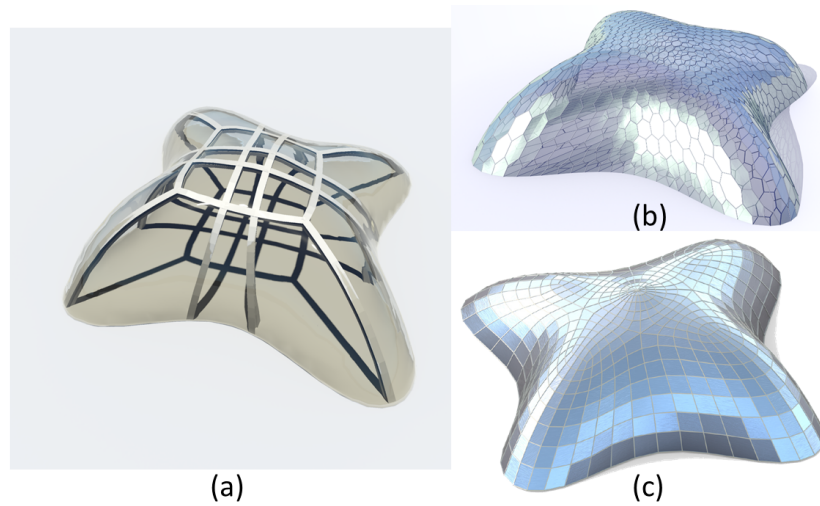


Figure 4.13: Results of Lilium. From (a) to (c): Our result, Voronoi grid-shell (Pietroni et al. 2015) and self-support quad shell (Vouga et al. 2012).

Results

Examples Figure 4.14 showcases various rib-shell structures produced by our method. Figure 4.15 demonstrates the improvement of structural strength for the Lilium. In order to compare with a pure shell, the thickness of the shell is set to a value so that it has the same volume as the final rib-reinforced shell. The maximum von Mises stress for the pure shell is 69.42 MPa which is beyond the allowable yield strength, and it is less than 40 MPa for the rib-reinforced shell. This comparison indicates rib-reinforced shell structures have a much higher strength than the pure shells with the same amount of material.

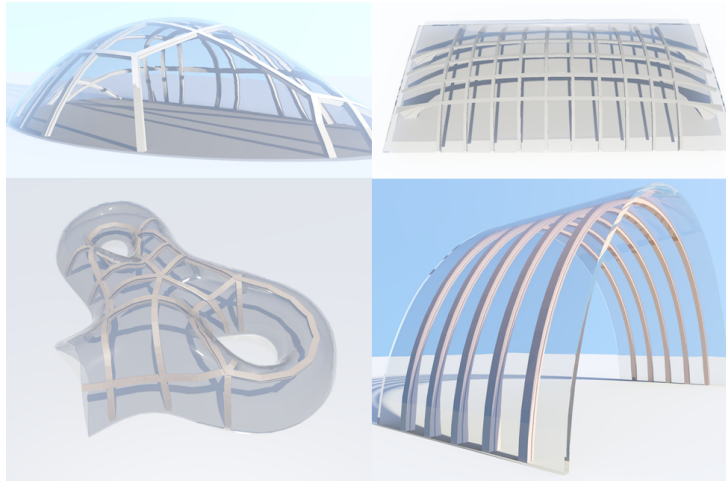


Figure 4.14: Rib-shell structures generated by our system, including Snail, Neumunster, Aquadom, and Bridge.

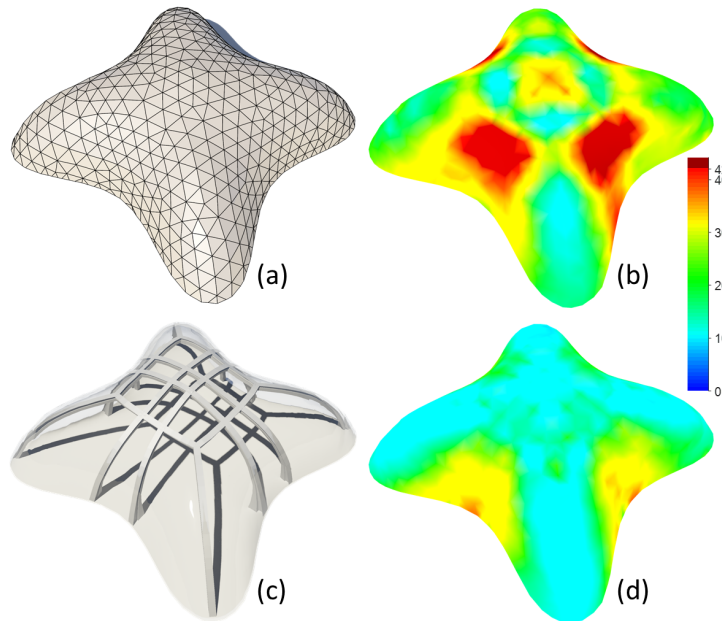


Figure 4.15: Rib-reinforced shell structure (c) generated from input mesh (a). And (b) and (d) are colouring visualizations of von Mises stress for pure shell and rib-reinforced shell, respectively, which cost the same volume of material.

Physical Experiments By performing a boolean operation on ribs and shell,

a watertight mesh of Guscio is obtained and fabricated rib-shell structure using an SLA 3D printer. To show the improvement of ribs, a pure shell with same amount of material is also fabricated. As shown in Figure 4.16 (a-1) and (b-1), the weight of the pure shell is 19.26g, while the weight of the shell reinforced by ribs is 19.25g. To compare the stiffness of the two models, same external loads are applied on the centre as shown in the bottom of Figure 4.16 to see the deformation. Figure 4.16 (a-2) and (b-2) are the initial states of the two shells for reference, and (a-3) and (b-3) are the final state under external loads. In Figure 4.16 (a-3), the pure shell is under a 30N load, the displacement at the centre is 5.6mm. While for the shell reinforced by ribs, the displacement at the centre is 1.2mm under a 33N load. The rib-shell structure achieves over 4 times higher strength compared with a pure shell under the same external load with the same volume of materials.

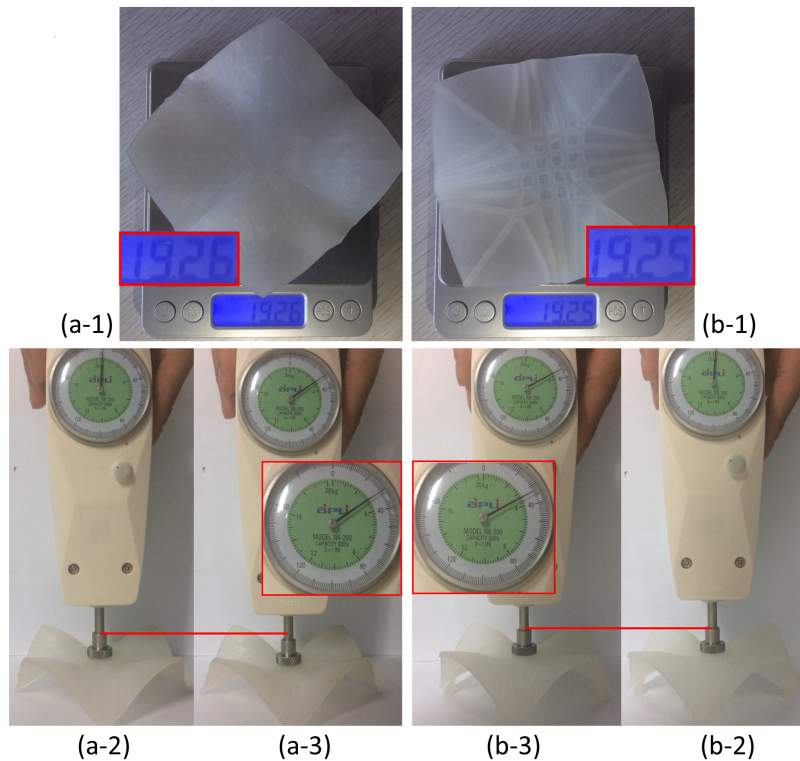


Figure 4.16: The fabricated shell (a-1) and rib-reinforced shell (b-1) cost about the same amount of materials (19.26g for the former and 19.25g for the latter). When imposing loads at the centre, the pure shell has a displacement of 5.6mm under a 30N load (a-3), while the displacement is 1.2mm for the rib-reinforced shell under a 33N load (b-3). And (a-2) and (b-2) are initial states without load for reference.

Extensions The system is also capable of generating other results similar to rib-shell structures. Two triangular meshes are generated from the images of kite and leaf shown in Figure 4.17 (a) and (c). For the kite model, the centre is fixed, and loads are imposed to every node to simulate wind force. And the for the leaf model, the petiole is fixed and gravity is applied. The resultant rib-shell structures for kite and leaf generated by the method are shown in Figure 4.17 (b) and (d), which seem to make sense to some extent.

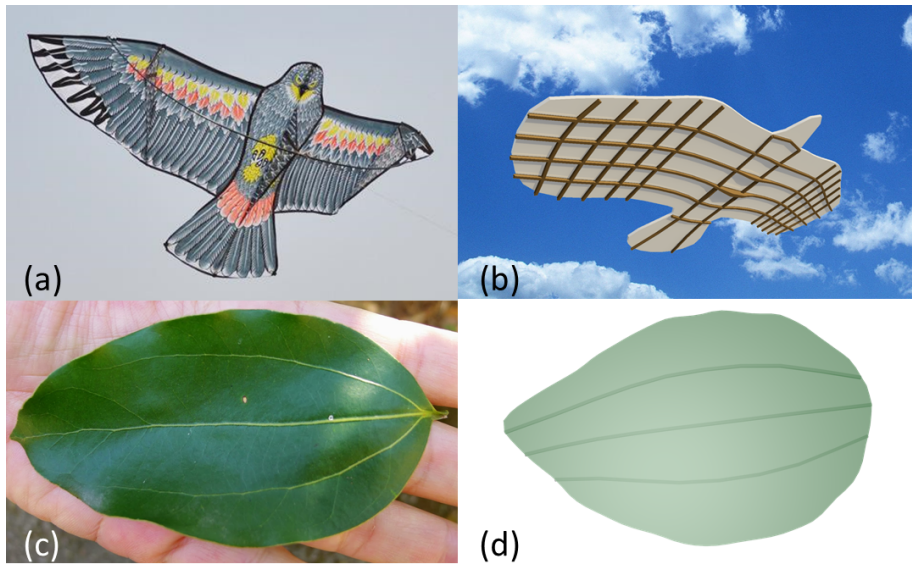


Figure 4.17: Rib-shell structures for kite (b) and leaf (d) models generated by our system, which imitate the things (a and c) in real world to some extent.

4.10 Summary

In this chapter, a method based on traditional elements is presented to generate and optimize a rib network to reinforce the structural stiffness and physical strength of input shell structure. The basic idea is to place ribs along the principal stress directions which are calculated from FEA results and encode the optimal topology. A variety of examples validate the capability and efficiency of the computational method.

Chapter 5

Unidirectional and bidirectional stiffened structure

5.1 Overview

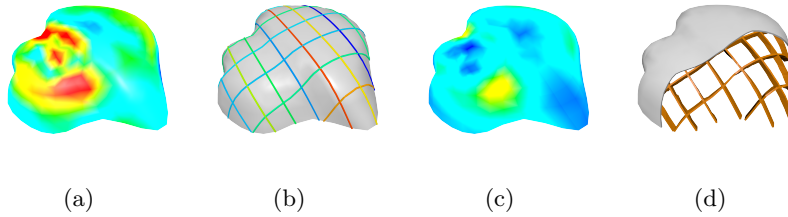


Figure 5.1: System overview. From left to right (a) the stress field on input surface, (b) the geometry is sliced equally, (c) after number and cross-section optimization of stiffeners, the final stress field on the same surface and (d) a cut-away show of the underlying stiffener structure.

The previous chapter introduced traditional finite elements including CST and DKT elements to simulate in-plane and out-plane behaviour of plate, and beam element to simulate behaviour of stiffeners. The coupled system of plate and beam elements is formulated by adding stiffeners' stiffness contributions to connecting plate nodes. Following the stress field computed from the coupled system, the stiffener network is flowed to best align with stress field so that the stiffener network can maximally support the geometry. The drawback of this method is that all the stiffeners must align with edges of the surface since the formulation of the coupled system is adding contribution from beam elements to

the connecting plate nodes.

To overcome above problem, this chapter introduces a well studied stiffened plate element (Samanta & Mukhopadhyay (2004)) in engineering that is capable of accounting for influence of arbitrary stiffener within a plate element. By applying plate's shape function to attached stiffener, the stiffener is able to deform simultaneously with plate element at any point. Thus, the stiffener does not have to align with any edge of the plate element, instead, it can be in arbitrary location within the plate element. Also the formulation can account for the influences of multiple stiffeners in a single element. With introduction of the stiffened element, the input mesh can be stiffened in arbitrary direction without affecting the geometry. A simple strategy of slicing the Axis-Aligned Bounding Box of input mesh is adopted to generate stiffeners along the interior surface of the mesh, and a constrained problem of finding minimum supporting structure is formulated and solved.

5.2 Stiffener element formulation

5.2.1 Stiffness matrix of the stiffener element

The formulation of the stiffener has been made in such a way that the stiffener can be placed within the shell element (Figure 5.2). The following assumptions have been made for the formulation of the stiffener.

- The stiffeners are considered as straight axis ribs in a 3D space.
- The stiffeners have same displacements as that of the plate.
- The common normal to the plate and stiffener system before bending remains straight and normal to the deflected shape after bending.
- The middle plane of the shell is taken as reference plane in the analysis of the stiffener, as shown in Figure 5.3.

The common shape function is used for both shell and stiffener element. It not only facilitates expressing the stiffness matrix of the stiffener in terms of the parameters of the shell element, but also maintains the compatibility of the stiffener within the shell.

If the angle between the arbitrary oriented stiffener and the local coordinate axis x of the shell element is ϕ (Figure 5.3), then the relationship between stiffener local coordinates ξ, η and shell local coordinates x, y can be expressed as

$$\begin{aligned}\xi &= (x - x_0) \cos \phi + (y - y_0) \sin \phi \\ \eta &= -(x - x_0) \sin \phi + (y - y_0) \cos \phi\end{aligned}\tag{5.2.1}$$

The relationship between the stiffener local displacement and shell elemental local displacement can also be expressed in a similar manner as

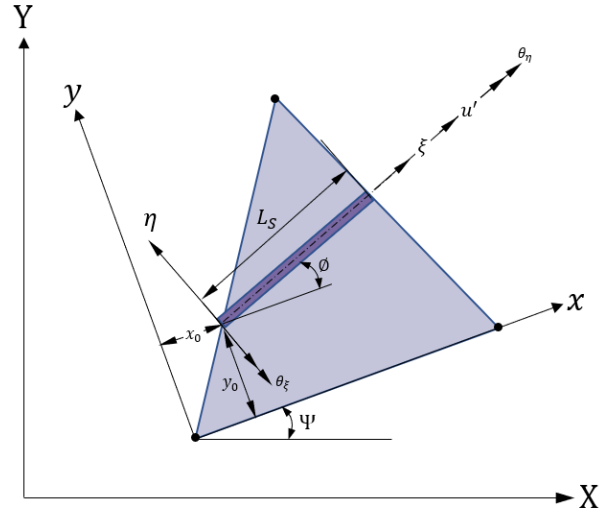


Figure 5.2: Local axis system of the stiffener, placed within the shell element

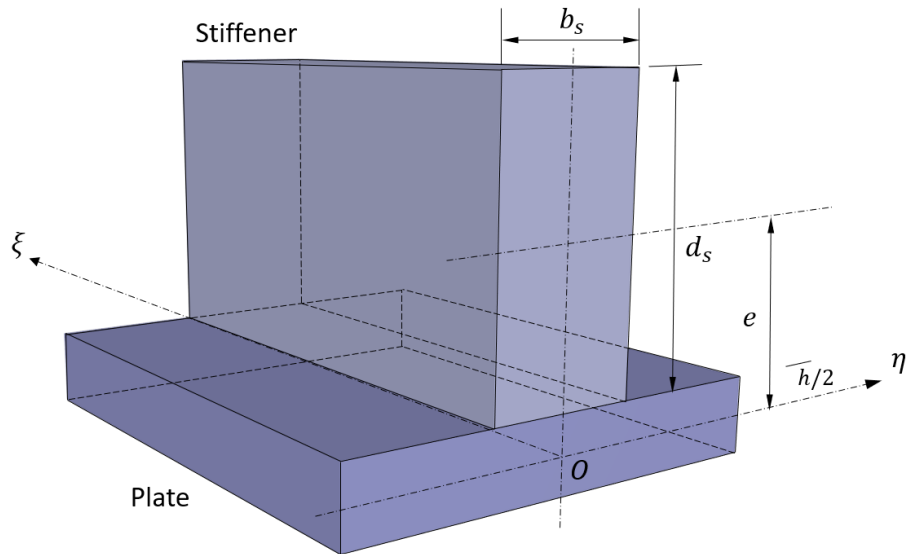


Figure 5.3: A stiffened plate showing the reference axis of the stiffener

$$\begin{aligned}
 u' &= u \cos \phi + v \sin \phi \\
 \theta_\xi &= \theta_x \cos \phi + \theta_y \sin \phi \\
 \theta_\eta &= -\theta_x \sin \phi + \theta_y \cos \phi
 \end{aligned}
 \tag{5.2.2}$$

where $u', \theta_\xi, \theta_\eta$ are the deflection and rotations in the stiffener local coordinate system as shown in Figure 5.2. The generalized strain vector $\boldsymbol{\varepsilon}_s$ in the stiffener local coordinate system (ξ, η) is given by:

$$\boldsymbol{\varepsilon}_s^\top = \left\{ \frac{\partial u'}{\partial \xi} \quad -\frac{\partial \theta_\xi}{\partial \theta} \quad -\frac{\partial \theta_\eta}{\partial \theta} \right\} \quad (5.2.3)$$

As the strain vector is expressed in terms of displacements in the shell middle plane, the shape function used is the same as that of the shell element which yields the stiffness matrix of the stiffener in terms of the nodal parameters of the shell element. Thus the deformation compatibility between the shell and the stiffener is ensured. Moreover, it avoids the incorporation of additional degrees of freedom for the stiffener element which is the most elegant feature of this modelling.

The generalized strain in the stiffener local coordinate system (ξ, η) has been transformed into the shell elemental local coordinate system (x, y) by using the following transformation

$$\boldsymbol{\varepsilon}_s = \mathbf{T}_s \boldsymbol{\varepsilon}'_s \quad (5.2.4)$$

where \mathbf{T}_s is the transformation matrix for the stiffener to correlate the strain in the stiffener local coordinate system to the shell elemental local coordinate system. $\boldsymbol{\varepsilon}'_s$ can be defined as

$$\boldsymbol{\varepsilon}'_s = \left\{ \frac{\partial u}{\partial x} \quad \frac{\partial v}{\partial y} \quad \left(\frac{\partial u}{\partial y} + \frac{\partial v}{\partial x} \right) \quad -\frac{\partial \theta_x}{\partial x} \quad -\frac{\partial \theta_y}{\partial y} \quad -\frac{\partial \theta_x}{\partial y} \quad -\frac{\partial \theta_y}{\partial x} \right\} \quad (5.2.5)$$

Equation 5.2.1 can be rewritten as

$$\begin{aligned} x &= x_0 + \xi \cos \phi - \eta \sin \phi \\ y &= y_0 + \xi \sin \phi + \eta \cos \phi \end{aligned} \quad (5.2.6)$$

The partial derivations of x and y with respect to ξ are

$$\frac{\partial x}{\partial \xi} = \cos \phi \quad \text{and} \quad \frac{\partial y}{\partial \xi} \quad (5.2.7)$$

By applying the chain rule, the strain matrix in the stiffener coordinate system can be written as

$$\frac{\partial u'}{\partial \xi} = \frac{\partial u'}{\partial x} \frac{\partial x}{\partial \xi} \quad (5.2.8)$$

With the help of Equation 5.2.2 and Equation 5.2.7, Equation 5.2.8 can be expressed as

$$\frac{\partial u'}{\partial \xi} = \frac{\partial}{\partial x} (u \cos \phi + v \sin \phi) \cos \phi + \frac{\partial}{\partial y} (u \cos \phi + v \sin \phi) \sin \phi \quad (5.2.9)$$

which leads to

$$\frac{\partial u'}{\partial \xi} = \frac{\partial u}{\partial x} \cos^2 \phi + \frac{\partial v}{\partial y} \sin^2 \phi + \left(\frac{\partial u}{\partial y} + \frac{\partial x}{\partial x} \right) \left(\frac{1}{2} \sin \phi \right) \quad (5.2.10)$$

Similarly other strain terms in the stiffener local coordinate system can be written as

$$\begin{aligned} -\frac{\partial \theta_\xi}{\partial \xi} &= -\left(\frac{\partial \theta_x}{\partial x} \cos^2 \phi + \frac{\partial \theta_y}{\partial y} \sin^2 \phi + \frac{\partial \theta_x}{\partial y} \left(\frac{1}{2} \sin 2\phi \right) + \frac{\partial \theta_y}{\partial x} \left(\frac{1}{2} \sin 2\phi \right) \right) \\ -\frac{\partial \theta_\eta}{\partial \xi} &= -\left(\frac{\partial \theta_x}{\partial x} \left(-\frac{1}{2} \sin 2\phi \right) + \frac{\partial \theta_y}{\partial y} \left(\frac{1}{2} \sin 2\phi \right) + \frac{\partial \theta_x}{\partial y} (-\sin^2 \phi) + \frac{\partial \theta_y}{\partial x} (\cos^2 \phi) \right) \end{aligned} \quad (5.2.11)$$

So the transformation matrix \mathbf{T}_s can be written as

$$\mathbf{T}_s = \begin{bmatrix} \cos^2 \phi & \sin^2 \phi & \frac{1}{2} \sin 2\phi & 0 & 0 & 0 & 0 \\ 0 & 0 & 0 & \cos^2 \phi & \sin^2 \phi & \frac{1}{2} \sin 2\phi & \frac{1}{2} \sin 2\phi \\ 0 & 0 & 0 & -\frac{1}{2} \sin 2\phi & \frac{1}{2} \sin 2\phi & -\sin^2 \phi & \cos^2 \phi \end{bmatrix} \quad (5.2.12)$$

The stress-strain relationship of the stiffener in the local coordinate system can be expressed as

$$\bar{\boldsymbol{\sigma}}_s = \mathbf{D}_s \boldsymbol{\varepsilon}_s \quad (5.2.13)$$

where

$$\bar{\boldsymbol{\sigma}}_s = \{N_{ss} \quad M_{ss} \quad T_{ss}\}^\top \quad (5.2.14)$$

and

$$\mathbf{D}_s = \begin{bmatrix} E_s A_s & E_s S_s & 0 \\ E_s S_s & E_s I_s & 0 \\ 0 & 0 & G_s J_s \end{bmatrix} \quad (5.2.15)$$

In the above equations, N_{ss} , M_{ss} , T_{ss} are the axial force, bending moment and torsion in the stiffener. E_s is the modulus of elasticity of the stiffener material, A_s is the cross-sectional area of the stiffener. S_s is the first moment of the stiffener cross-sectional area about the reference axis (i.e. the plate middle surface) as shown in Figure 5.3. I_s is the second moment of the stiffener cross-sectional area about reference axis, G_s is the modulus of rigidity and J_s is the polar moment of inertia of the stiffener cross-sectional area. The details of J_s is given by [Mukhopadhyay & Satsangi \(1984\)](#).

Eccentricity of the eccentric stiffener has been taken into account in the rigidity matrix, where I_s and S_s have been calculated with reference to the plate middle surface. For concentric stiffener this eccentricity is zero and I_s and S_s

have been calculated with reference to the stiffener middle surface, as in this case plate middle surface and stiffener middle surface are same.

Using the principle of virtual work, the element stiffness matrix of the stiffness matrix of the stiffener is given by

$$\mathbf{k}_s = \int_{L_s} \mathbf{T}^T \mathbf{B}_s^T \mathbf{T}_s^T \mathbf{D}_s \mathbf{T}_s \mathbf{T} d\xi \quad (5.2.16)$$

where \mathbf{T} is the transformation matrix defined in Equation 3.2.18.

In the above equation, all the matrices are defined previously. Equation 5.2.16 has been integrated by two point Gaussian quadrature rule (see Table 5.1) along the length of the stiffener L_s , where L_s is shown in Figure 5.2.

After the element stiffness matrix of the stiffener has been formulated, it is added to the element stiffness of the shell with which the global stiffness matrix \mathbf{K} is assembled.

In the above formulation of the stiffener, as the same displacement function is used for both the shell and the stiffener element, the compatibility condition at the shell beam junction is ensured. The formulation of the stiffener is done in such a manner that it can be placed anywhere within the shell element. Due to this the restriction of mesh grading is obviated and thus the treatment of stiffened shell problems can be carried out in a more elegant manner.

5.3 Pipeline of the uni- and bi-stiffened optimization

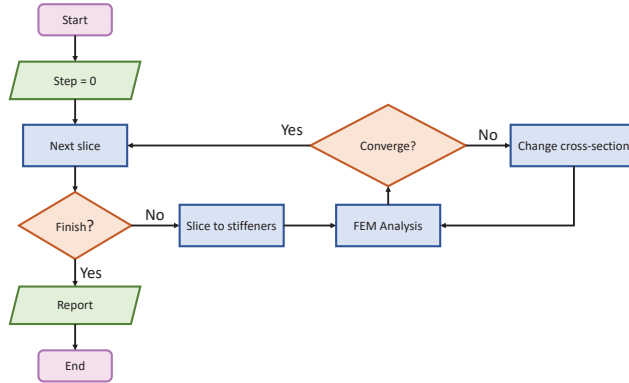


Figure 5.4: The pipeline of the uni- and bi-stiffened structure optimization

Figure 5.4 shows the pipeline of optimisation. Given the input geometry, the bounding box of the object is first computed. Two values corresponding to number of slices N_U in U direction and number of slices N_V in V direction are given here to slice the bounding box. In total, there are a combination of

Table 5.1: 1D Gauss points and weights

Figure	Points	Weights
	$a = 0$	2
	$a = -\sqrt{3}/3$ $b = \sqrt{3}/3$	1 1
	$a = -\sqrt{0.6}$ $b = 0$ $c = \sqrt{0.6}$	$5/9$ $8/9$ $5/9$

$\{S_{ij} | \forall i \in \{1, N_U\}, \forall j \in \{1, N_V\}, i + j \neq 0\}$ situations. Starting from step 0 (S_{00}) which doesn't generate any stiffeners), the algorithm then automatically takes one slicing S_{ij} out of the set to slice spatially equally in one direction or two directions to produce unidirectional or bidirectional stiffeners. With the generated stiffeners, lower and upper bounds of cross-section size and maximum material strength, a constrained optimization problem is formulated to find least

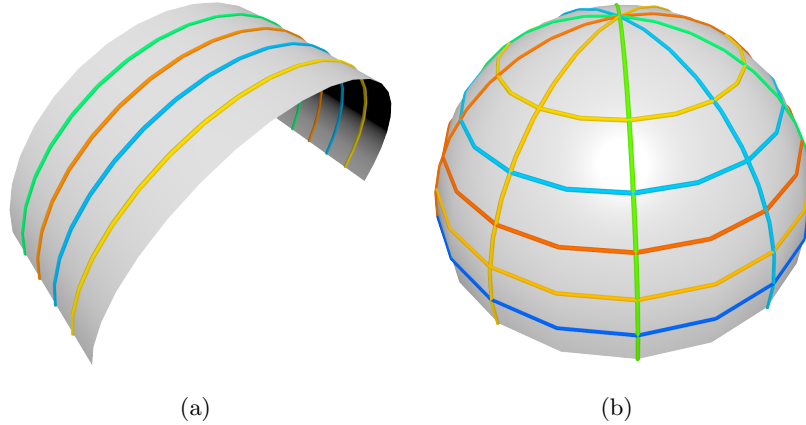


Figure 5.5: Unidirectional (a) and bidirectional (b) slicing of geometries

material. The algorithm terminates when all slicing cases have been examined and the optimal slicing $S_{i^*j^*} \in S_{ij}$ with minimum material consumption will be returned as solution.

5.3.1 Unidirectional and bidirectional slicing

In this part, two ways are presented to generate stiffeners along geometry surface. The unidirectional stiffeners are generated by slicing objects in the same direction as can be seen in Figure 5.5 (a). While the bidirectional stiffeners are created by slicing the geometry in two orthogonal directions (Figure 5.5 (b)).

5.3.2 Optimization formulation

For 3D printed objects and structures, the wall-thickness of shell structures is usually taken to be the minimum printing wall-thickness to reduce material consumption. The structural strength and stiffness are satisfied by stiffening shell structures with stiffeners. Since the wall-thickness of shell structures has been the minimum printing thickness, minimizing material consumption of 3D printed objects and structures becomes minimization of the total volume of all stiffeners.

There are a number of different types of stiffeners available in engineering applications. Here stiffeners with rectangle cross-sections are used to demonstrate the optimization design model. Let w and h represent the width and height of the stiffener cross-section. The goal is to minimize the overall volume of stiffeners while satisfy the strength requirement. The objective function for optimization design can be formulated as finding the minimum of total stiffener volume:

$$\min_{w,h} \sum_{i=1}^n \text{Volume} \mathcal{R}_i \quad (5.3.1)$$

$$s.t. \begin{cases} \sigma_{\max} \leq \bar{\sigma} \\ \underline{w} \leq w \leq \bar{w} \\ \underline{h} \leq h \leq \bar{h} \end{cases} \quad (5.3.2)$$

where σ_{\max} is the maximum von Mises stress in both shell elements and stiffener elements, and $\bar{\sigma}$ is the material yield strength, \underline{w} , \bar{w} , \underline{h} and \bar{h} are the lower and upper bounds of stiffener width and height.

5.4 Numerical examples and experimental results

The integrated finite element analysis and optimization design are implemented in MATLAB on a desktop PC with an Intel Xeon E5 CPU and 32GB memory. As the FEA is computational expensive, the CST, DKT and stiffener elements are implemented in C++ but compiled as MEX functions for speed-up consideration. The unconstrained problem can be solved using Interior Point method.

Unidirectional stiffeners Stiffened flat plates and stiffened curved shells are most popular. A flat plate is first considered here to be stiffened optimally with unidirectional stiffeners. The unidirectional stiffeners mean that all the stiffeners go in same direction.

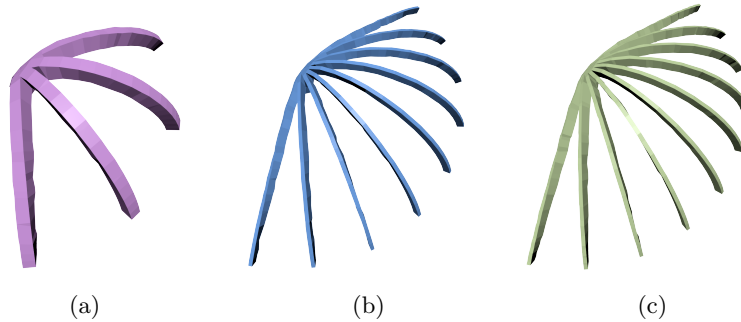


Figure 5.6: Optimized unidirectional stiffeners from the algorithm

Figure 5.6 presents optimized supporting structures in same direction. Figure 5.6(a) has 4 stiffeners reaching size limits with a volume consumption 3710.55mm^3 but still fails to satisfy strength requirement. Figure 5.6(b) is the best output within the searching domain which has a material consumption 1301.65mm^3 . Figure 5.6(c) shows more stiffeners than Figure 5.6(b) are used, and the overall material usage 1658.35mm^3 is slightly larger than Figure 5.6(b).

Bi-directional stiffeners In order to maintain overall structure strength under loads, there is a limit of minimum material required. For the purpose of saving material, less supporting stiffeners are to be expected. To find out the balance between maintaining object soundness and reducing printing material, all possible combinations of stiffeners in orthogonal directions are iterated to search for an optimized result.

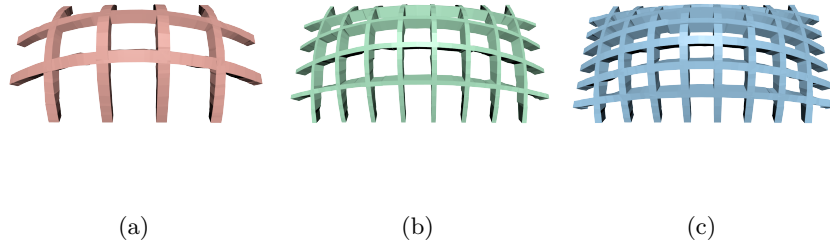


Figure 5.7: Optimized bidirectional stiffeners from the algorithm

Figure 5.7 presents some of the optimized results with different slices. For the case in Figure 5.7 (a), less stiffeners are used in both directions leading to less volume of stiffeners 7068.91mm^3 . But the stress constraint $\sigma < \bar{\sigma}$ cannot be satisfied even when the size of stiffeners reaches the upper limit. Figure 5.7 (b) is the best output from the algorithm with material usage at 6780.97mm^3 . In Figure 5.7 (c), though the stress constraint is satisfied, the use of more stiffeners causes the material usage up to 7200.96mm^3 .

5.5 3D printed uni- and bi-directional stiffened objects

With the optimization algorithm of unidirectional and bidirectional stiffened objects proposed in this chapter, the minimum stiffener volumes of some stiffened objects were obtained, their 3D printed models were shown in Figure 5.8, and the stress changes with and without the optimized stiffeners were shown in Figure 5.9 -Figure 5.15, respectively.

Figure 5.9 shows the stress distributions, stiffeners, and 3D printed model of a unidirectionally stiffened plate. In the figure, (a) depicts the stress distribution in the flat plate without unidirectional stiffeners with a maximum stress of 278.198MPa , (b) shows the optimized unidirectional stiffeners with a total volume of 338.53mm^3 , (c) gives the stress distribution in the flat plate stiffened by the optimized stiffeners with a maximum stress 22.9778MPa , and (d) is a photo of the 3D printed model of the stiffened plate. By applying the optimized unidirectional stiffeners, the maximum stress reduces from 278.198MPa to 22.977MPa .

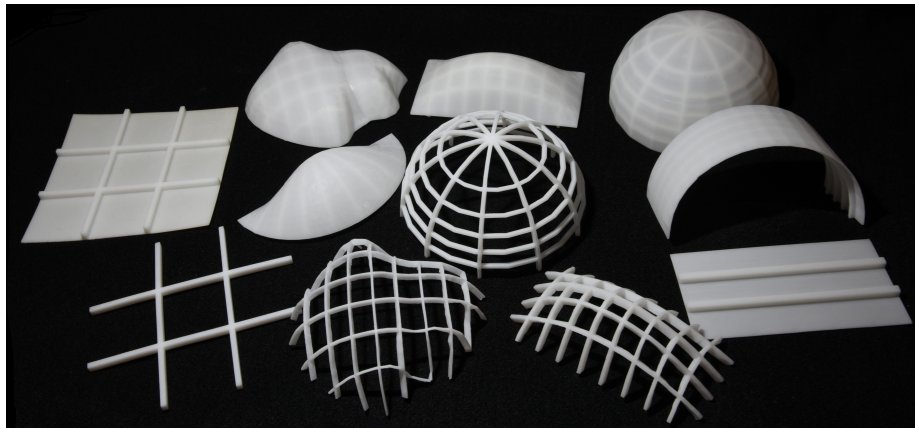


Figure 5.8: All prints

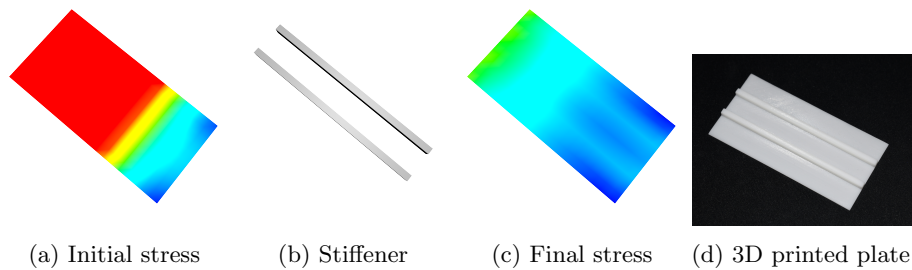


Figure 5.9: Unidirectionally stiffened flat Plate.

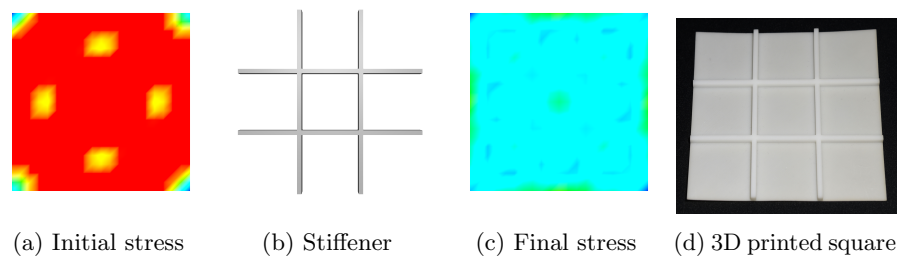


Figure 5.10: Bidirectionally stiffened Square.

Figure 5.10 gives the stress distributions, stiffeners, and 3D printed model of a bidirectionally stiffened square. Figure 5.10 (a) shows initial stress distribution of square without bidirectional stiffeners with a maximum stress of 159.268MPa, (b) shows the optimized bidirectional stiffeners with a total volume of 481.623mm³, (c) gives the stress distribution in the square stiffened by the optimized stiffeners with a maximum stress 21.749MPa, and (d) is a photo of the 3D printed model

of the stiffened square. By applying the optimized bidirectional stiffeners, the maximum stress reduces from 159.268MPa to 21.749MPa.

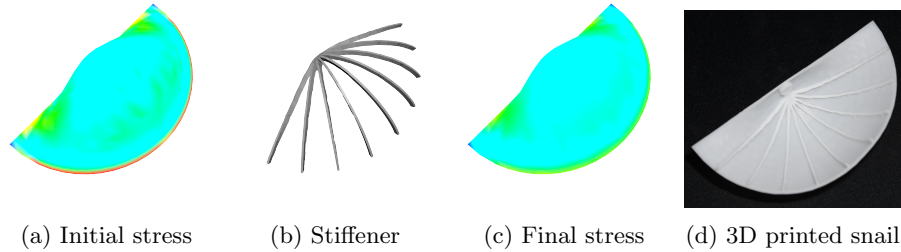


Figure 5.11: Unidirectionally stiffened Snail.

The stress fields, stiffeners and 3D printed model of a unidirectionally stiffened snail are shown in Figure 5.11. In the figure, the initial maximum stress within the snail without any stiffening structures is 33.273MPa as shown in (a). After applying a total volume of 141.645mm³ stiffeners (b) to the snail, the maximum stress (c) drops from 33.273MPa to 27.2818MPa in the final printed 3D model (d).

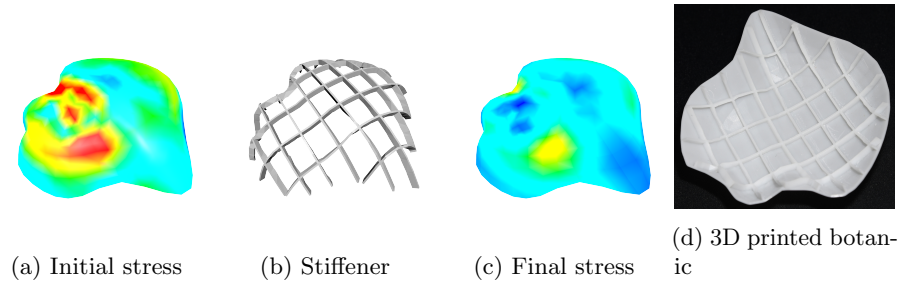


Figure 5.12: Bidirectionally stiffened Botanic.

Another example of botanic is given in Figure 5.12 to show the stress distributions, stiffeners, and 3D printed model. Figure 5.12 (a) shows initial stress distribution of botanic without bidirectional stiffeners with a maximum stress of 90.927MPa, (b) shows the optimized bidirectional stiffeners with a total volume of 346.926mm³, (c) gives the stress distribution in the botanic stiffened by the optimized stiffeners with a maximum stress 38.6041MPa, and (d) is a photo of the 3D printed model of the stiffened botanic. By applying the optimized bidirectional stiffeners, the maximum stress reduces from 90.927MPa to 38.6041MPa.

The stress fields, stiffeners and 3D printed model of a unidirectionally stiffened bridge are shown in Figure 5.13. In the figure, the initial maximum stress within the bridge without any stiffening structures is 94.4982MPa as shown in (a). After applying a total volume of 281.855mm³ stiffeners (b) to the bridge, the

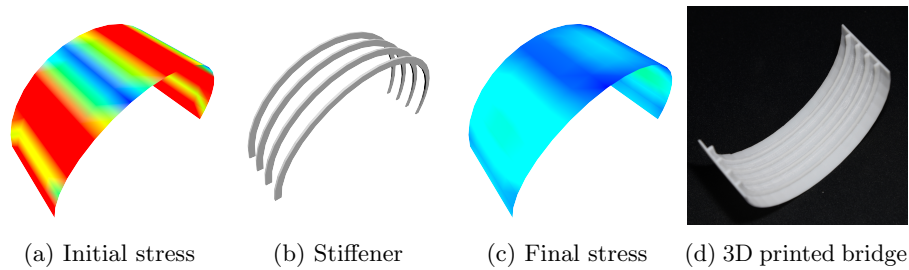


Figure 5.13: Unidirectionally stiffened Bridge.

maximum final stress (c) drops from 94.4982MPa to 15.7848MPa in the final printed 3D model (d).

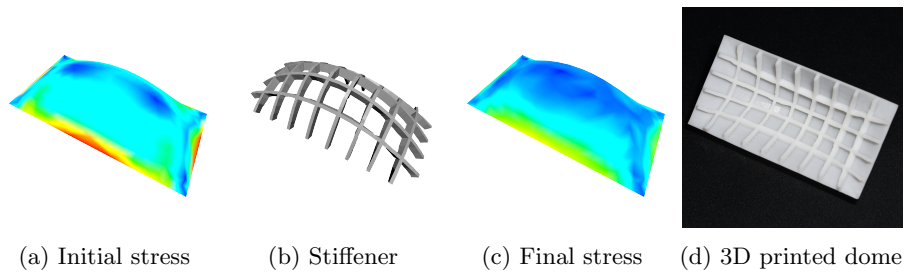


Figure 5.14: Bidirectionally stiffened Dome.

Figure 5.14 show the stress distributions, stiffeners, and 3D printed object of a dome. The maximum stress 59.028MPa in the initial stress distribution without bidirectional stiffeners (a) is reduced to the maximum stress 35.6306MPa (c) with the introduction of a total volume of 689.206mm³ bidirectionally stiffened stiffeners (b). (d) is a photo of the 3D printed model of the stiffened dome.

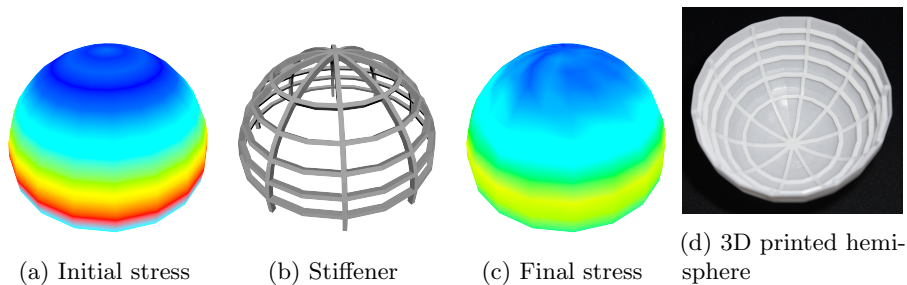


Figure 5.15: Bidirectionally stiffened Hemisphere.

Figure 5.15 show the stress distributions, stiffeners, and 3D printed object of a hemisphere. The initial stress distribution without bidirectional stiffeners

has a maximum stress of 42.0198MPa shown in (a), (b) shows the optimized bidirectional stiffeners with a total volume of 989.145mm³, (c) gives the stress distribution in the hemisphere stiffened by the optimized stiffeners with a maximum stress 36.6904MPa, and (d) is a photo of the 3D printed model of the stiffened hemisphere. The applied optimized bidirectional stiffeners help to reduce, the maximum stress from 42.0198MPa to 36.6904MPa.

5.6 Summary

In this chapter, stiffened structures widely applied in engineering are used to stiffen 3D printed objects and structures for saving material costs and improving structural strength and stiffness. To this aim, finite element analysis of stiffened structures with unidirectional and bidirectional stiffeners placing in arbitrary positions is investigated, optimization design of the stiffened structures is examined, and they are integrated to minimize the material consumption of 3D printing. Numerical examples demonstrate obvious improvements brought in by the proposed approach.

Chapter 6

Stress guided stiffened structures

6.1 Overview

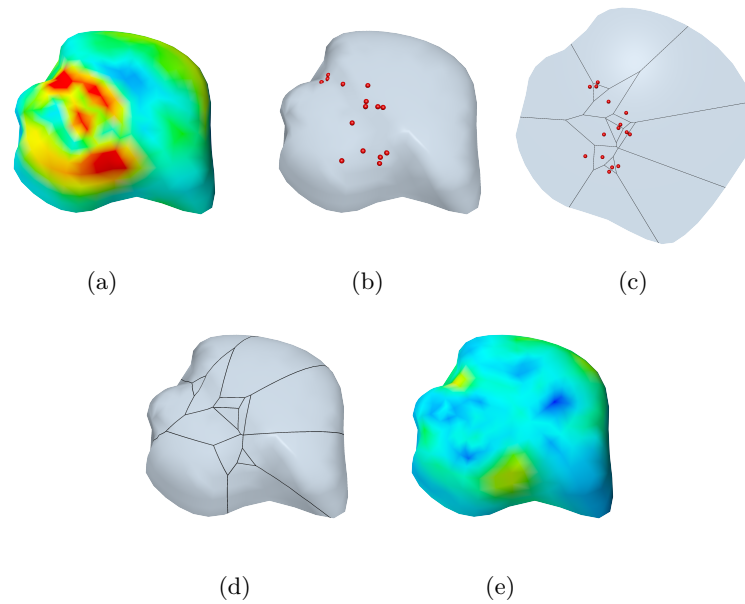


Figure 6.1: Algorithm overview. From left to right: (a) the initial stress field of a pure plate shell structure (b) seeds dispersed randomly on dangerous areas (c) Voronoi diagram in parametric space (d) stiffeners created in 3D space based on 2D Voronoi diagram and (e) final stress field after size optimization of stiffeners

In Chapter 5 a well studied stiffener element has been introduced and analysed. However, during the simulation, a naive and straight-forward method is applied to generate stiffeners, which is to slice the axis aligned bounding box of the object. It is easy to implement and has a small amount of user inputs to control the generation of stiffeners. Also it requires little knowledge of FEM and optimization for the user to find an optimised result. The drawback of the uni- and bi-stiffened optimisation is the stiffeners are created purely based on the geometry information, regardless of stress field of the mesh which might not place the stiffeners in the best locations. To improve the uni- and bi-stiffened optimization, a stress guided stiffener optimisation is proposed using the same stiffener element.

6.2 Pipeline of stress guided stiffener optimisation

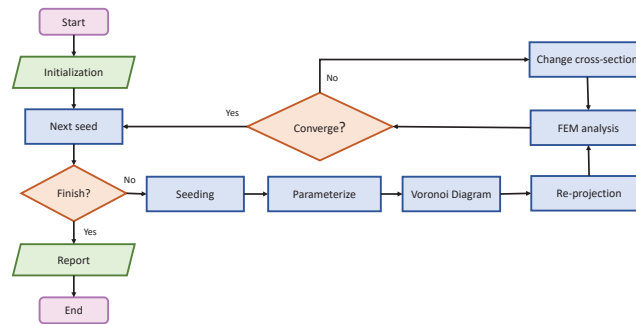


Figure 6.2: The pipeline of the stress guided stiffener optimization

The pipeline of the stress guided stiffener optimisation is summarised in Figure 6.2.

Seed generation To seed the mesh, the stress field of the geometry is first calculated under given boundary conditions and forces. A probability map \mathcal{P} of the surface is built by dividing the stress map with the material strength $\mathcal{P} = \{\sigma_i/\sigma_s\}$. With the computed probability map \mathcal{P} , a given number N_s of seeds are placed along the geometry. The seeding is driven by the map \mathcal{P} and tends to place more seeds in areas with higher stress. Therefore more supporting structures will be generated around dangerous places.

Stiffener generation Once seeds $\mathcal{S} \in \mathbf{R}^3$ are obtained, they are mapped to 2D space by LSCM to create a 2D Voronoi diagram of these seeds. Then the 2D Voronoi diagram is re-projected back to 3D space using barycentre coordinate and edges of the diagram are representations of stiffeners attached to the geometry. An optimization of the stiffeners' cross-sections is carried out to find the optimized size to meet design conditions with least printing material used.

Monte-Carlo simulation As the generation of seeds is a random process based on stress field and is fixed during the optimization after initialization, it is more accurate to simulate the seeding step some times to find a global optimal solution. To fulfil this goal, Monte-Carlo simulation is therefore introduced to repeat the procedure by a given number of times to avoid local minima.

6.3 Seed generation

In order to generate stress guided stiffeners, it is natural to identify and enhance dangerous areas based on stress field. In this research, the strategy to achieve the above goal is by controlling the distribution of seeds over the geometry. The generation of these seeds over the surface of a 3D mesh is thus a constrained sampling problem.

In the past decades, a lot of research effort has been envisaged to develop new and efficient sampling algorithms, especially to create sampling with blue noise features, that best fit the needs of several geometric modelling and graphics applications (Li et al. 2008, Lagae & Dutré 2008, Cline et al. 2009).

In the following, n_t stands for the number of triangles of the mesh, s_i the stress of triangle t_i , σ_s the material strength, n_s the number of expected seeds, p^* for the probability threshold.

Algorithm 3: Seed generation

Input: stress field $\{s_i\}$, material strength σ_s , number of expected seeds n_s and probability threshold p^*

Output: markedFaces

```

count = 0
markedFaces[ $n_t$ ] = false
while count  $\leq$   $n_s$  do
    |  $t_i$  = UniformRandom(1,  $\dots$ ,  $n_t$ )
    |  $p$  = UniformRandom(0, 1)
    | if not markedFaces[ $t_i$ ] and  $p^* < p < s_i/\sigma_s$  then
    | | count++
    | | markedFaces[ $t_i$ ] = true
    | end
end
end

```

The algorithm 3 shows how to generate seeds over the surface. For an input shell with given boundary conditions and external loads, an initial stress field is calculated. The stress field is used to compute s_i/σ_s for each triangle. The algorithm then randomly picks an unmarked triangle with randomly generated probability p . If the probability p is over probability threshold p^* and smaller than the computed s_i/σ_s , the triangle is seeded and marked. The algorithm repeats searching for faces with high stress until reaching the expected n_s seeds.

6.4 Parametrization

To generate a Voronoi diagram from a number of seeds in 3D and trace stiffeners from the diagram and the mesh is more complicated than in 2D since it requires searching for geodesic lines between arbitrary two points. Once converted to 2D space, the tracing of stiffeners in 3D space becomes the problem of finding intersections between a segment and mesh edges, which is easier to implement.

Based on a least-squares approximation of the Cauchy-Riemann equations, Lévy et al. (2002) proposed a new quasi-conformal parametrization method.

6.4.1 Conformal Maps

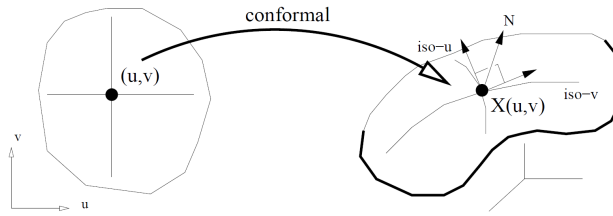


Figure 6.3: In a conformal map, the tangent vectors to the iso- u and to the iso- v curves are orthogonal and have the same length. (Figure from Lévy et al. (2002))

As shown in Figure 6.3, an application \mathcal{X} mapping a (u, v) domain to a surface is said to be conformal if for each (u, v) , the tangent vectors to the iso- u and iso- v curves passing through $\mathcal{X}(u, v)$ are orthogonal and have the same norm, which can be written as:

$$N(u, v) \times \frac{\partial \mathcal{X}}{\partial u}(u, v) = \frac{\partial \mathcal{X}}{\partial v}(u, v) \quad (6.4.1)$$

where $N(u, v)$ denotes the unit normal to the surface. In other words, a conformal map is locally isotropic, i.e. maps an elementary circle of the (u, v) domain to an elementary circle of the surface.

6.4.2 Conformality in a Triangulation

Consider a triangulation $\mathcal{G} = \{[1 \cdots n], \mathcal{T}, (\mathbf{p}_j)_{1 \leq j \leq n}\}$, where $[1 \cdots n], n \geq 3$ corresponds to the vertices, \mathcal{T} is a set of n' triangles represented by triples of vertices, and $\mathbf{p}_j \in \mathbb{R}^3$ denotes the geometric location at the vertex j . Each triangle has a local orthonormal basis, where $(x_1, y_1), (x_2, y_2), (x_3, y_3)$ are the coordinates of its vertices in this basis (i.e., the normal is along the z -axis). The local bases of two triangles sharing an edge are consistently oriented.

By considering the restriction of \mathcal{X} to a triangle T and applying the conformality criterion to the inverse map $\mathcal{U} : (x, y) \rightarrow (u, v)$, Equation 6.4.1 becomes:

$$\frac{\partial \mathcal{X}}{\partial u} - i \frac{\partial \mathcal{X}}{\partial v} = 0 \quad (6.4.2)$$

where \mathcal{X} has been written using complex numbers, i.e. $\mathcal{X} = x + iy$. According to the theorem on the derivatives of inverse functions, this implies that

$$\frac{\partial \mathcal{U}}{\partial x} + i \frac{\partial \mathcal{U}}{\partial y} = 0 \quad (6.4.3)$$

PC

where $\mathcal{U} = u + iv$.

Since this equation cannot in general be strictly enforced, the violation of the conformality condition is minimized in the least squares sense, which defines the criterion C :

$$C(T) = \int_T \left| \frac{\partial \mathcal{U}}{\partial x} + i \frac{\partial \mathcal{U}}{\partial y} \right|^2 dA = \left| \frac{\partial \mathcal{U}}{\partial x} + i \frac{\partial \mathcal{U}}{\partial y} \right|^2 A_T \quad (6.4.4)$$

where A_T is the area of the triangle and the notation $|z|$ stands for the modulus of the complex number z . Summing over the whole triangulation, the criterion to minimize is then

$$C(\mathcal{T}) = \sum_{T \in \mathcal{T}} C(T) \quad (6.4.5)$$

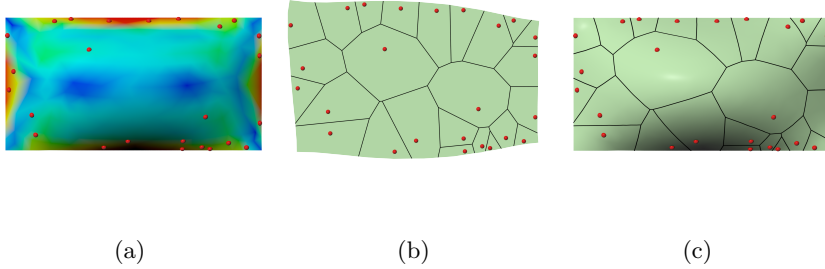


Figure 6.4: Overflow of the generation of Voronoi stiffeners.

Figure 6.4 gives an example of overflow of the generation of Voronoi stiffeners. After 3D seeds are obtained from previous step, they are projected to 2D space by LSCM parametrization as shown in Figure 6.4.

6.5 Voronoi diagram

Voronoi diagrams appear in many forms in nature, and in several cases they are related lightweight and strong structures. For example, bones have a Voronoi-like porous structure (see Figure 6.5), with a higher concentration of material where

the bone undergoes more stress. This natural principle has also been applied recently to 3D print honeycomb-like structures (Lu et al. 2014) and grid-shell structures (Pietroni et al. 2014).

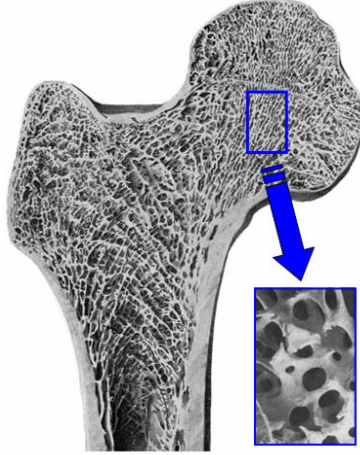


Figure 6.5: Example of cancellous bone. Cancellous bone has fully interconnected porous structure. (Figure from Ishikawa (2010))

For the input boundary surface \mathcal{S} and a given number n of seeds $\{\mathbf{s}_i\}, i \in (1, n)$ defined in the interior domain of \mathcal{S} , a Voronoi tessellation of \mathcal{S} is defined to be the collection of Voronoi cells $\{\Omega_i\}, i \in (1, n)$ of these seeds, where

$$\Omega_i = \{\mathbf{x} \in \mathcal{S} \mid \|\mathbf{x} - \mathbf{s}_i\| \leq \|\mathbf{x} - \mathbf{s}_j\|, \forall j \neq i\} \quad (6.5.1)$$

and $\|\cdot\|$ denotes the Euclidean norm. A Voronoi tessellation is called a centroidal Voronoi tessellation (CVT) (Du et al. 1999) if each seed coincides with the centroid of its Voronoi cell, where the centroid \mathbf{c}_i of its Voronoi cell Ω_i is defined as

$$\mathbf{c}_i = \frac{\int_{\mathbf{x} \in \Omega_i} \rho(\mathbf{x}) \mathbf{x} d\sigma}{\int_{\mathbf{x} \in \Omega_i} \rho(\mathbf{x}) d\sigma} \quad (6.5.2)$$

in which $d\sigma$ is the area differential, and $\rho(\mathbf{x})$ is the density function over the domain \mathcal{S} .

6.6 Stiffener Extraction

After having the Voronoi diagram in 2D, the next thing is to extract stiffeners from the diagram. Suppose two ends of an edge of the diagram is represented as p_a and p_b respectively. And the edge intersects with the projected input mesh at $m_i, i = 1, \dots, n$, n is the number of intersections (shown in Figure 6.6).

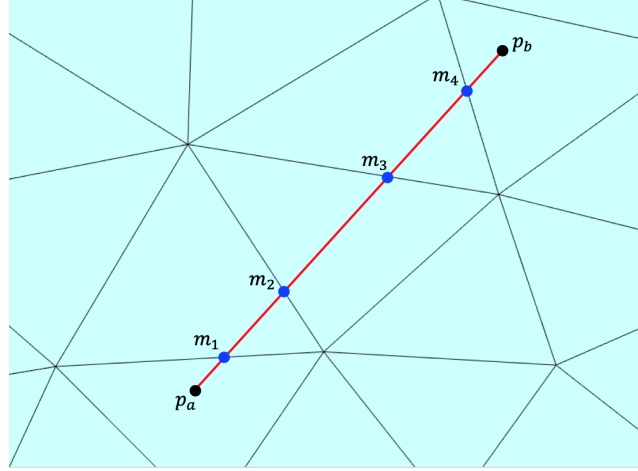


Figure 6.6: Stiffener extraction

The stiffener extraction step takes each edge from the Voronoi diagram, and iterates through all triangles t_i^l to detect all intersections p_1, p_2 in all triangles. In order to easily project 2D intersection points back to 3D, the found intersections p_1, p_2 are converted to area coordinates L_1, L_2 using local triangle t_i^l . After all edges of the Voronoi diagram have been processed, all intersections represented in local area coordinates are converted back to 3D coordinates. The algorithm is summarized in Algorithm 4.

Algorithm 4: Stiffener Extraction

Input: voronoi diagram, local triangles t_i^l , global triangles t_i^g

Output: stiffeners

```

for each edge  $\epsilon_i$  in voronoi diagram do
  for each  $t_j^l$  do
    if  $\epsilon_i$  intersects with  $t_j^l$  then
       $[p_1, p_2] = \text{IntersectSegments}(\epsilon_i, t_j^l)$ 
       $[L_1, L_2] = \text{AreaCoords}(p_1, p_2, t_j^l)$ 
      stiffeners.append( $L_1, L_2, t_j^l$ )
    end
  end
end
end
Project all 2D stiffeners back to 3D space
for stiffener in stiffeners do
   $[p_1, p_2] = \text{CartesianCoords}(L_1, L_2, t_i^g)$ 
end

```

6.9 Results

The proposed algorithm is implemented in Matlab with FEM calculations compiled into MEX functions for speed reason. The results are tested on a PC with an Intel Xeon E5 CPU and 32GB memory, running Windows OS.

6.9.1 Parameter setting

During the optimization and fabrication, the printer minimal wall thickness w_s is set to be 1mm so both the \underline{w} and \underline{h} are set to be 1mm. The material strength σ_s for photosensitive resin is 42N/m^2 . The user specified upper printing thickness is assumed to be 4mm.

6.9.2 Different probability thresholds

The probability threshold p^* is introduced here to control the spread of the seeds over the geometry. When p^* is set to a low value, the faces with small probabilities will not be filtered out and marked as seeded faces (triangles), causing a wide spread of seeds over all faces. On the contrary, if p^* is set to a high value, triangles with stress less than $p^*\sigma_s$ will never be chosen, therefore guarantee the concentration of seeds around critical areas. Figure 6.7 shows the effect of different probability thresholds p^* on the generated stiffeners. As can be seen from the figure, a smaller p^* will produce a more uniform distribution of stiffeners than a larger p^* , but seeds still prefer the areas with large stress.

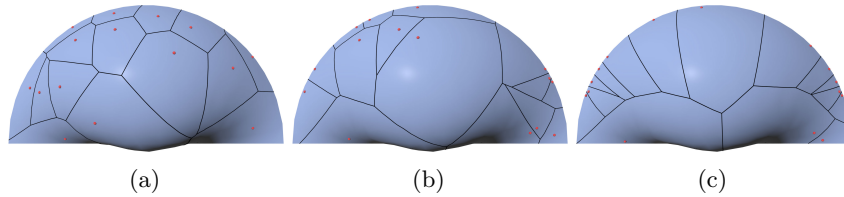


Figure 6.7: Effect of different probability thresholds p^* on the distribution of seeds. From left to right, $p^* = 0$, $p^* = 0.3$ and $p^* = 0.5$

Figure 6.7 illustrates the effect of probability. It can be noticed a smaller p^* leads to a more uniform distribution of seeds over the surface, while a larger p^* drives seeds towards critical areas and creates more supporting structures around those places.

6.9.3 Monte-Carlo simulations

Figure 6.8 shows the effect of random number generator seed r_s . With the same stress map and same number of seeds ($n_s = 35$), the distributions of seeds in Figures 6.8a, 6.8b and 6.8c are different, leading to variational Voronoi diagram demonstrated in 6.8d, 6.8e and 6.8f respectively and creates different supporting structures as shown in 6.8g, 6.8h, and 6.8i respectively.

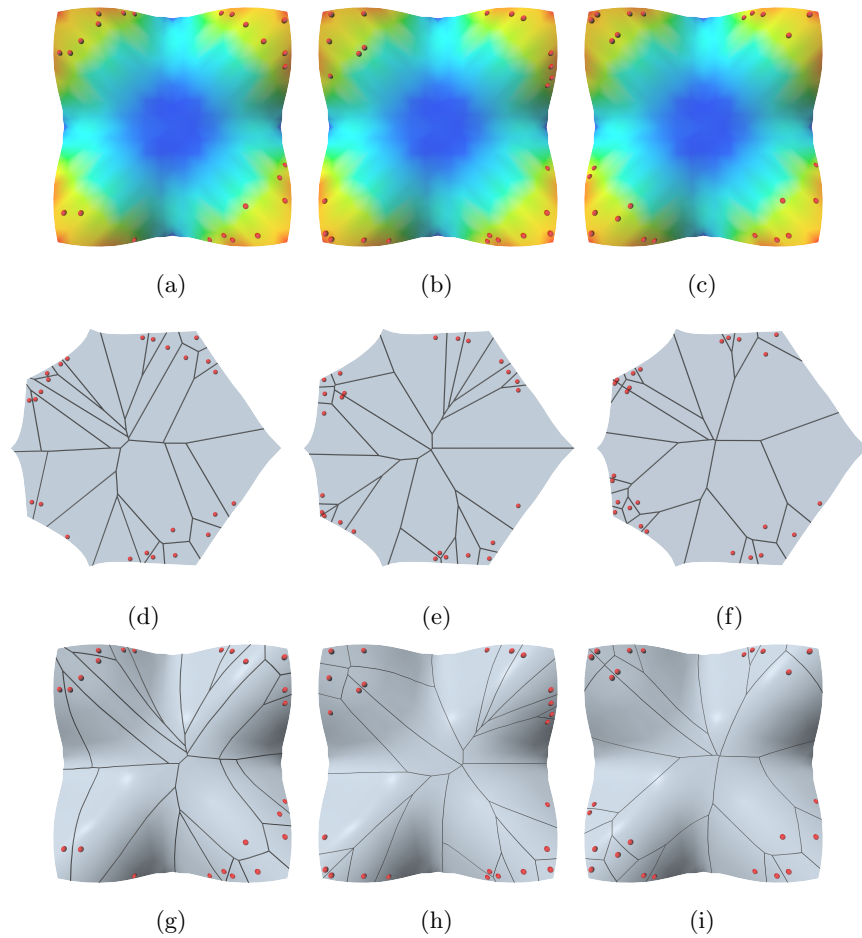


Figure 6.8: Monte-Carlo simulations of Guscio. The random number generator seeds r_s for each column are: 10, 20 and 30 respectively.

6.10 3D printed stress-guided stiffened objects

With the optimization algorithm of stress-guided stiffened objects proposed in this chapter, the minimum stiffener volumes of some stiffened objects are obtained, their 3D printed models are shown in Figure 6.9, and the stress changes with and without the optimized stiffeners are shown in Figure 6.10 - Figure 6.18, respectively.

Figure 6.10 shows the stress distributions, stiffeners, and 3D printed model of a stress-guided stiffened plate. In the figure, (a) depicts the stress distribution in the flat plate without stiffeners with a maximum stress of 278.198MPa, (b) shows the optimized stiffeners with a total volume of 418.5148mm³, (c) gives the stress distribution in the flat plate stiffened by the optimized stiffeners with



Figure 6.9: All prints

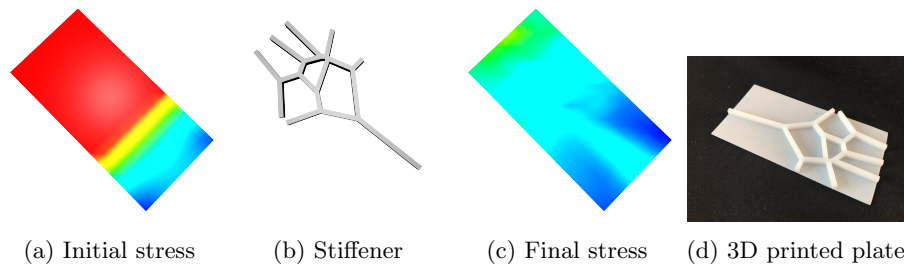


Figure 6.10: Stress-guided stiffened Plate.

a maximum stress 24.6426MPa, and (d) is a photo of the 3D printed model of the stiffened plate. By applying the optimized stiffeners, the maximum stress reduces from 278.198MPa to 24.6426MPa.

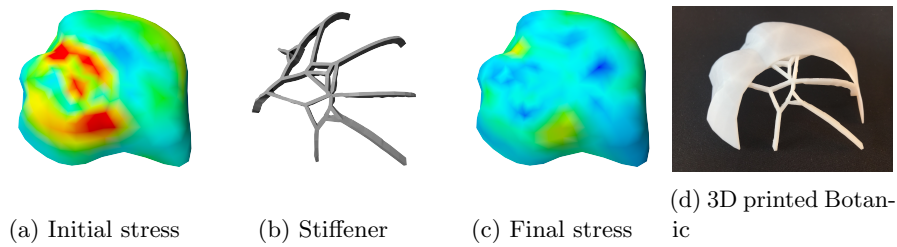


Figure 6.11: Stress-guided stiffened Botanic.

Another example of Botanic is given in Figure 6.11 to show the stress distributions, stiffeners, and 3D printed model. Figure 6.11 (a) shows the initial stress distribution of Botanic without stiffeners with a maximum stress of

90.927MPa, (b) shows the optimized stiffeners with a total volume of 418.856mm³, (c) gives the stress distribution in the Botanic stiffened by the optimized stiffeners with a maximum stress 33.8706MPa, and (d) is a photo of the 3D printed model of the stiffened Botanic. By applying the optimized stiffeners, the maximum stress reduces from 90.927MPa to 33.8706MPa.

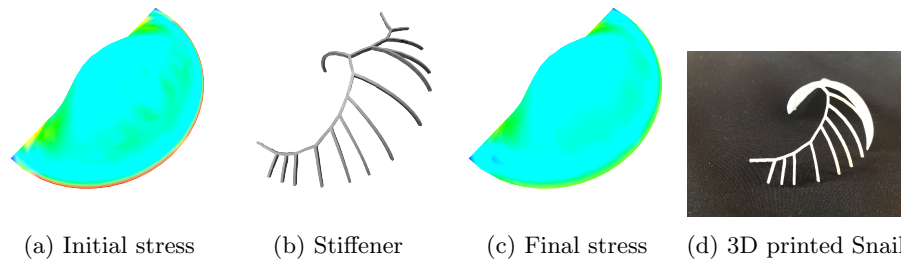


Figure 6.12: Stress-guided stiffened Snail.

The stress fields, stiffeners and 3D printed model of a stiffened Snail is shown in Figure 6.12. In the figure, the initial maximum stress within the Snail without any stiffening structures is 33.273MPa as shown in (a). After applying a total volume of 84.0108mm³ stiffeners (b) to the Snail, the maximum stress (c) drops from 33.273MPa to 28.3634MPa in the final printed 3D model (d).

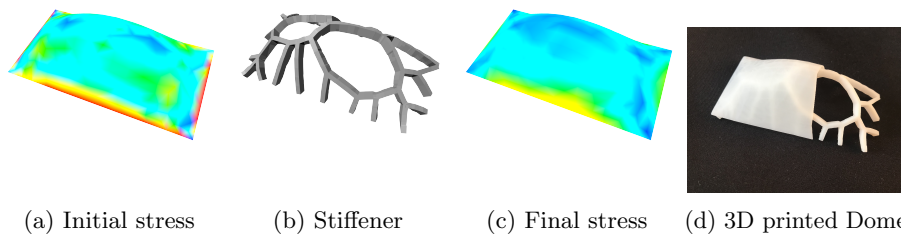


Figure 6.13: Stress-guided stiffened Dome.

Figure 6.13 shows the stress distributions, stiffeners, and 3D printed object of a Dome. The maximum stress 59.028MPa in the initial stress distribution without supporting stiffeners (a) is reduced to the maximum stress 34.3583MPa (c) with the introduction of a total volume of 754.704mm³ stiffened stiffeners (b). (d) is a photo of the 3D printed model of the stiffened Dome.

The stress fields, stiffeners and 3D printed model of a stiffened bridge is shown in Figure 6.14. In the figure, the initial maximum stress within the bridge without any stiffening structures is 94.4982MPa as shown in (a). After applying a total volume of 535.109mm³ stiffeners (b) to the bridge, the maximum final stress (c) drops from 94.4982MPa to 16.8744MPa in the final printed 3D model (d).

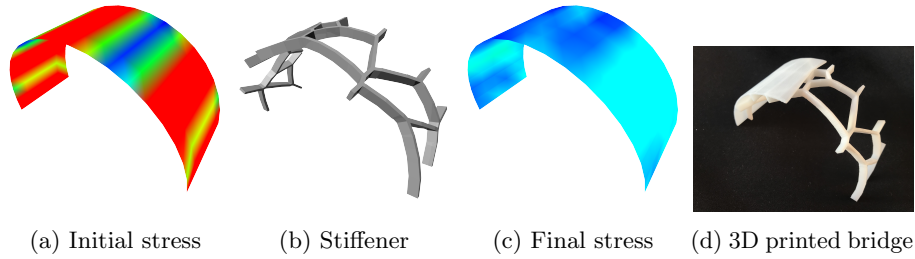


Figure 6.14: Stress-guided stiffened Bridge.

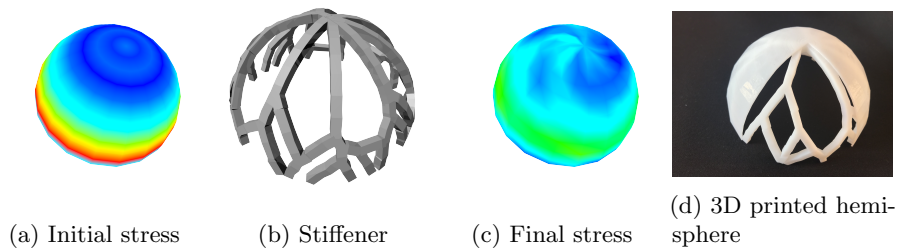


Figure 6.15: Stress-guided stiffened Hemisphere.

Figure 6.15 shows the stress distributions, stiffeners, and 3D printed object of the hemisphere. The initial stress distribution without stiffeners has a maximum stress of 42.0198MPa shown in (a), (b) shows the optimized stiffeners with a total volume of 1961.93mm³, (c) gives the stress distribution in the hemisphere stiffened by the optimized stiffeners with a maximum stress 31.2246MPa, and (d) is a photo of the 3D printed model of the stiffened hemisphere. The applied optimized stiffeners help to reduce to the maximum stress from 42.0198MPa to 31.2246MPa.

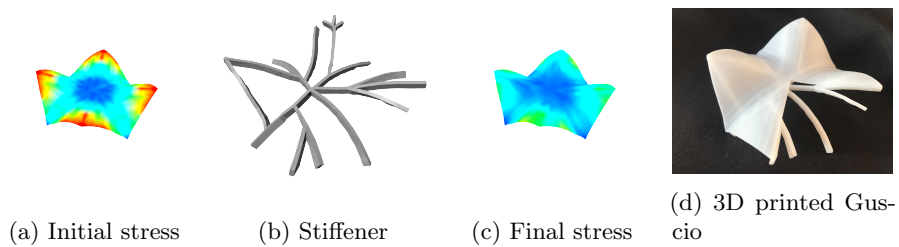


Figure 6.16: Stress-guided stiffened Guscio.

Figure 6.16 show the stress distributions, stiffeners, and 3D printed object of the Guscio. The maximum stress 43.8379MPa in the initial stress distribution without supporting stiffeners (a) is reduced to the maximum stress 29.5158MPa

(c) with the introduction of a total volume of 711.483mm^3 stiffened stiffeners (b). (d) is a photo of the 3D printed model of the stiffened Guscio.

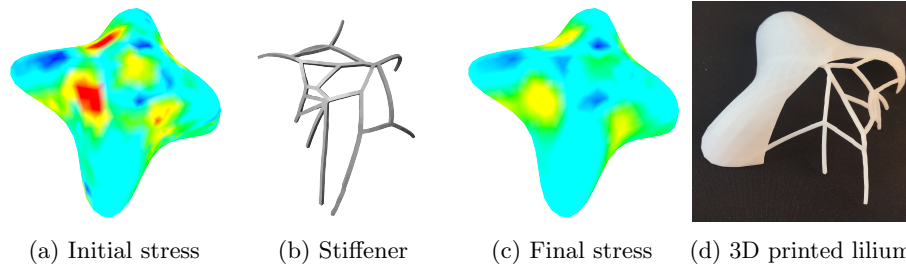


Figure 6.17: Stress-guided stiffened Lilium.

Figure 6.17 show the stress distributions, stiffeners, and 3D printed object of a Lilium. The initial stress distribution without stiffeners has a maximum stress of 52.0412MPa shown in (a), (b) shows the optimized stiffeners with a total volume of 227.294mm^3 , (c) gives the stress distribution in the Lilium stiffened by the optimized stiffeners with a maximum stress 35.3578MPa , and (d) is a photo of the 3D printed model of the stiffened Lilium. The applied optimized stiffeners help to reduce, the maximum stress from 52.0412MPa to 35.3578MPa .

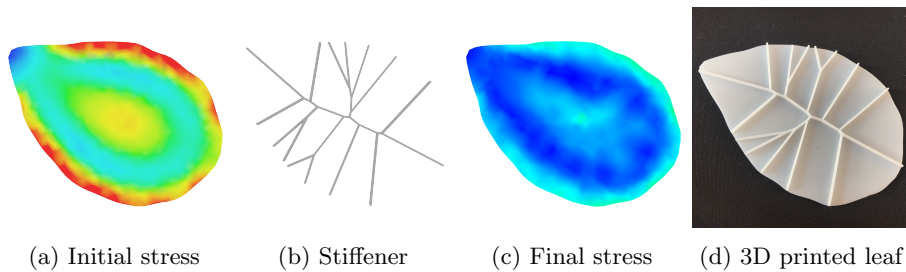


Figure 6.18: Stress-guided stiffened Leaf.

The stress fields, stiffeners and 3D printed object of a leaf is shown in Figure 6.18. In this example, the initial maximum stress in the leaf without any stiffening structures is 54.9437MPa as shown in (a). After attaching a total volume of 112.512mm^3 stiffeners (b) to the leaf, the maximum final stress drops from 54.9437MPa to 20.2208MPa as depicted in (c) and the final printed 3D model is given in (d).

6.11 Summary

The stress guided stiffener optimization framework uses a stress field to guide the distribution of seeds. A parametrization of the input object based on LSCM is computed to map the geometry and seeds to 2D. A Voronoi diagram of the

projected 2D seeds is calculated and 2D stiffeners are reconstructed from the Voronoi diagram and the projected mesh. Finally, the 2D stiffeners are projected back to 3D space by area coordinates and a size optimization is conducted to obtain least supporting structure under current configuration. And some stochastic Monte-Carlo simulations are repeated so that local minimum can be avoided. The results are lightweight supporting structures that can sustain given boundary conditions, external forces and material strength.

Chapter 7

Conclusion and Future Work

7.1 Overview

Large span shell structures are widely applied in architecture, engineering and daily life. To support these shell objects, additional supporting structures are used to improve bending resistance and overall structural soundness. It is obvious that the more material used to stiffen the object, the more solid and sound it will be. But the increase of material will also increase both the cost and time of fabrication. Additionally, the generation, layout and shape of the stiffeners are not easy even for experienced experts or architecture. Therefore the objective of this research is to design automatic pipelines with a few simple user inputs that can automatically generate and optimise the supporting structure for the input geometry without a lot of manual efforts. To this aim, three different methods of enhancing thin shell structures have been proposed in this research.

7.2 Edge stiffened structures

The first method is to combine traditional plate elements and beam elements to simulate the in-plane membrane deformations and out-plane deflections respectively. The stiffness contributions from the beam elements are calculated and added to corresponding nodes. The optimization of this method comes into two parts, 1) a layout optimization to generate stiffeners and remove redundant ones and flow stiffeners to align stress field and 2) a size and shape optimization to further reduce material usage while keeping structural soundness. The disadvantage of this method is the stiffeners are aligned to the mesh edges and the edges need to be updated repeatedly during the flow step.

The limitations future work of this method are:

- The in-plane behaviour of the plate element is simulated using CST element.

Although the CST element is simple to formulate and compute, it is only used to simulate constant strain in-plane deformation. Advanced triangular elements like Linear Strain Triangular element(LST) that are capable of accounting for various variable strains inside an element should be used to replace CST element;

- DKT triangle element assumes the input is thin shell structures, for thick shell structures, elements without neglecting shear forces should be more appropriate;
- The method is based on the principal stress directions which are computed from FEA results. However, the FEA results depend on the external loads. As a consequence, the rib-shell structure has remarkable structural properties under the initial external load. When the loads change, the overall performance cannot be guaranteed. Actually, this is a common limitation for all FEA-based method.

7.3 Uni- and bi-directional stiffened structures

Unlike the first method which changes the geometry constantly during the flow process, the stiffened plate element allows stiffeners to be placed anywhere within the shell element. The theory applies plate element's shape function to stiffeners so that the stiffness terms from the stiffeners can be integrated together into the plate elements. Based on the stiffened plate element, the second method computes the bounding box of the geometry and slice the object in uni- and bi-directional directions to create uni- and bi-directional stiffeners. The stiffener generation step is followed by a size optimization of the cross-section. To avoid local minima, different number of slices in both directions are simulated to find out the best material usage.

The limitations and future work for this method are:

- The Axis Aligned Bounding Box (AABB) of a geometry is sliced equally in space to generate supporting stiffeners without considering the stress field therefore the distributions of unidirectional and bidirectional stiffeners are not optimized for the stress map. An approach to overcome this problem is to find the bounding box of areas exceeding material strength and slice the geometry within these critical areas.
- During the shape optimisation, only rectangular cross-section has been discussed, other cross-sections with good mechanical properties need to be investigated to assess their performances in saving material costs and improving structural strength and stiffness.
- During the size optimization, all the stiffeners are assumed to be the same and have same cross-section size. This assumption will involve much less optimization variables and can be much faster to find the optimal result in the design domain. The disadvantage of this method is that the optimized

stiffener structure will have the same size over the whole geometry and cause material waste in low stress areas. An improvement to this process is to let each stiffener segment has its own width and height to relax constraints on the cross-section.

7.4 Stress guided stiffened structures

The second method generates stiffeners in an intuitive and straightforward way by slicing bounding box of the geometry spatially equally. The generated stiffeners are not stress guided so that may cause material waste at low stress areas. To overcome this problem, the third method is first to compute a probability map which will help disperse seeds based on the stress field. The strategy for spreading seeds is to place more seeds over critical areas since these places have higher stresses therefore larger probability. Once the seeds are obtained, they are projected to 2D space using LSCM to create a Voronoi diagram. The 2D diagram is then projected back to 3D space so that edges of the 3D diagram are a representation of the stiffeners. The size optimization is carried out to further reduce material use. However, the seeds generation is a random process so that the computed Voronoi diagram and generated stiffeners are also random patterns. To ensure global optimization result, some Monte-Carlo simulations are conducted to search in design domain to find global minimum.

The limitations and future work for this method are:

- In current implementation, each plate element can at most has one seed at the centre of the element, limiting the location and number of stiffeners within the element. In the future, the seed should be randomly placed within the element and the element should be able to have multiple seeds so that more supporting structures can be introduced for this element.
- The distribution of seeds are based on the ratio of element stress against material strength. And the ratios of all elements are assumed to be fixed during the seed insertion step which is not accurate. In the future, an incremental way of adding seeds should be discussed to update the stress field after each insertion.
- Since the Monte-Carlo simulations are independent of each other, the method can be easily parallelised to use several threads to simulate various situations simultaneous in the future.

Bibliography

- Adini, A. & Clough, R. W. (1960), *Analysis of plate bending by the finite element method*, University of California.
- Adriaenssens, S., Block, P., Veenendaal, D. & Williams, C. (2014), *Shell structures for architecture: form finding and optimization*, Routledge.
- Alinia, M. M. & Shirazi, R. S. (2009), ‘On the design of stiffeners in steel plate shear walls’, *Journal of Constructional Steel Research* **65**(10), 2069 – 2077.
URL: <http://www.sciencedirect.com/science/article/pii/S0143974X09001436>
- Allman, D. (1984), ‘A compatible triangular element including vertex rotations for plane elasticity analysis’, *Computers & Structures* **19**(1-2), 1–8.
- Ansola, R., Canales, J., Tarrago, J. & Rasmussen, J. (2004), ‘Combined shape and reinforcement layout optimization of shell structures’, *Structural and Multidisciplinary Optimization* **27**(4), 219–227.
- Arashmehr, J., Rahimi, G. & Rasouli, S. (2012), ‘Numerical and experimental stress analysis of stiffened cylindrical composite shell under transverse end load’, *Journal of World Academy of Science, Engineering and Technology* **67**, 1298–1302.
- Arnout, S., Firl, M. & Bletzinger, K.-U. (2012), ‘Parameter free shape and thickness optimisation considering stress response’, *Structural and Multidisciplinary Optimization* **45**(6), 801–814.
- Bainbridge, J. (2017), ‘3d Printing Filament Properties’.
URL: <https://github.com/superjamie/lazyweb>
- Baker, G. & Pavlovic, M. (1982), ‘Elastic stability of simply supported rectangular plates under locally distributed edge forces’, *ASME, Transactions, Journal of Applied Mechanics* **49**, 177–179.
- Barik, M. & Mukhopadhyay, M. (2002), ‘A new stiffened plate element for the analysis of arbitrary plates’, *Thin-Walled Structures* **40**(7), 625–639.
URL: <http://www.sciencedirect.com/science/article/pii/S0263823102000162>

- Barut, A., Madenci, E., Tessler, A. & Jr, J. H. S. (2000), ‘A new stiffened shell element for geometrically nonlinear analysis of composite laminates’, *Computers and Structures* p. 30.
- Bathe, K.-J. & Ho, L.-W. (1981), ‘A simple and effective element for analysis of general shell structures’, *Computers & Structures* **13**(5-6), 673–681.
- Bommes, D., Zimmer, H. & Kobbelt, L. (2009), ‘Mixed-integer quadrangulation’, *ACM TRANS. GRAPH* pp. 1–10.
- Bronstein, A. M., Bronstein, M. M. & Kimmel, R. (2008), *Numerical geometry of non-rigid shapes*, Springer Science & Business Media.
- Burton, J., Basiliere, P., Smith, S., Shanler, M. & Halpern, M. (2017), Predicts 2018: 3d Printing and Additive Manufacturing, Technical Report G00342398, Gartner.
- Chattopadhyay, B., Sinha, P. & Mukhopadhyay, M. (1995), ‘Geometrically non-linear analysis of composite stiffened plates using finite elements’, *Composite Structures* **31**(2), 107–118.
URL: <http://linkinghub.elsevier.com/retrieve/pii/0263822395000046>
- Cline, D., Jeschke, S., White, K., Razdan, A. & Wonka, P. (2009), Dart throwing on surfaces, in ‘Computer Graphics Forum’, Vol. 28, Wiley Online Library, pp. 1217–1226.
- Cook, R. D. (1993), ‘Further development of a three-node triangular shell element’, *International Journal for Numerical Methods in Engineering* **36**(8), 1413–1425.
- Cutler, B. & Whiting, E. (2007), Constrained planar remeshing for architecture, in ‘Proceedings of Graphics Interface 2007’, ACM, pp. 11–18.
- Davis, L. & Block, P. (2011), *Scaffolding to Structure: Construction in Thin-Shell Masonry*.
- Ding, X., Ji, X., Ma, M. & Hou, J. (2013), ‘Key techniques and applications of adaptive growth method for stiffener layout design of plates and shells’, *Chinese Journal of Mechanical Engineering* **26**(6), 1138–1148.
- Du, Q., Faber, V. & Gunzburger, M. (1999), ‘Centroidal Voronoi tessellations: Applications and algorithms’, *SIAM review* **41**(4), 637–676.
- Ebke, H.-C., Bommes, D., Campen, M. & Kobbelt, L. (2013), ‘QEx: Robust quad mesh extraction’, *ACM Trans. Graph.* **32**(6), 168:1–168:10.
- Eigensatz, M., Kilian, M., Schiftner, A., Mitra, N. J., Pottmann, H. & Pauly, M. (2010), ‘Paneling architectural freeform surfaces’, *ACM transactions on graphics (TOG)* **29**(4), 45.

- Esterhuizen, G. S., Dolinar, D. R. & Ellenberger, J. L. (2010), ‘Pillar and roof span design in stone mines’, *Extracting the Science A Century of Mining Research* .
- Fraeijs de Veubeke, B. (1963), Upper and lower bounds in matrix structural analysis, Technical report, LTAS.
- Frei, O. & Rasch, B. (1995), ‘Finding form: towards an architecture of the minimal’, *Axel Menges, Stuttgart* .
- Gibson, L. J. & Ashby, M. F. (1999), *Cellular solids: structure and properties*, Cambridge university press.
- Glymph, J., Shelden, D., Ceccato, C., Mussel, J. & Schober, H. (2004), ‘A parametric strategy for free-form glass structures using quadrilateral planar facets’, *Automation in construction* **13**(2), 187–202.
- Goswami, S. & Mukhopadhyay, M. (1995), ‘Geometrically non-linear transient dynamic response of laminated composite stiffened shells’, *Journal of reinforced plastics and composites* **14**(6), 618–640.
- Gunderson, R., Haisler, W., Stricklin, J. & Tisdale, P. (1969), ‘A rapidly converging triangular plate element.’, *AIAA journal* **7**(1), 180–181.
- Hao, P., Wang, B., Li, G., Meng, Z., Tian, K. & Tang, X. (2014), ‘Hybrid optimization of hierarchical stiffened shells based on smeared stiffener method and finite element method’, *Thin-Walled Structures* **82**, 46–54.
URL: <http://linkinghub.elsevier.com/retrieve/pii/S0263823114001177>
- Holgate, A. (1997), *The Art of Structural Engineering: The Work of Jörg Schlaich and His Team*, Stuttgart: Ed. Axel Menges.
- Ishikawa, K. (2010), ‘Bone Substitute Fabrication Based on Dissolution-Precipitation Reactions’, *Materials* **3**(2), 1138–1155.
URL: <http://www.mdpi.com/1996-1944/3/2/1138>
- Jacobson, A., Baran, I., Popovic, J. & Sorkine, O. (2011), ‘Bounded biharmonic weights for real-time deformation.’, *ACM Trans. Graph.* **30**(4), 78–1.
- Ji, J., Ding, X. & Xiong, M. (2014), ‘Optimal stiffener layout of plate/shell structures by bionic growth method’, *Comput. Struct.* **135**, 88–99.
- Jirousek, J. (1981), ‘A family of variable section curved beam and thick-shell or membrane-stiffening isoparametric elements’, *International Journal for Numerical Methods in Engineering* **17**(2), 171–186.
- Johannes, M. (1958), ‘Stability of rib-reinforced cylindrical shells under lateral pressure’, *IABSE* **18**.
- Kälberer, F., Nieser, M. & Polthier, K. (2007), ‘Quadcover - surface parameterization using branched coverings’, *Comput. Graph. Forum* **26**(3), 375–384.

- Kang, Y. G. & Chang, Y. Z. (2013), Dynamic stability analysis of steel concrete composite of ribbed shell under stepped loads, *in* ‘Advances in Manufacturing Science and Engineering’, Vol. 712 of *Advanced Materials Research*, Trans Tech Publications, pp. 815–821.
- Katz, S. & Tal, A. (2003), *Hierarchical mesh decomposition using fuzzy clustering and cuts*, Vol. 22, ACM.
- Knight, N. (1997), ‘Raasch challenge for shell elements’, *AIAA journal* **35**(2), 375–381.
- Kokcharov, I. & Burov, A. (2013), ‘Structural integrity analysis’, *Switzerland: Geneva* .
- Koko, T. & Olson, M. (1991a), ‘Nonlinear transient response of stiffened plates to air blast loading by a superelement approach’, *Computer Methods in Applied Mechanics and Engineering* **90**(1-3), 737–760.
- Koko, T. & Olson, M. (1992), ‘Vibration analysis of stiffened plates by super elements’, *Journal of Sound and Vibration* **158**(1), 149–167.
- Koko, T. S. & Olson, M. D. (1991b), ‘Non-linear analysis of stiffened plates using super elements’, *International Journal for Numerical Methods in Engineering* **31**(2), 319–343.
URL: <https://onlinelibrary.wiley.com/doi/abs/10.1002/nme.1620310208>
- Kwok, T.-H., Li, Y. & Chen, Y. (2016), ‘A structural topology design method based on principal stress line’, *Computer-Aided Design* **80**, 19 – 31.
- Lagae, A. & Dutré, P. (2008), A comparison of methods for generating Poisson disk distributions, *in* ‘Computer Graphics Forum’, Vol. 27, Wiley Online Library, pp. 114–129.
- Lam, Y. & Santhikumar, S. (2003), ‘Automated rib location and optimization for plate structures’, *Structural and multidisciplinary optimization* **25**(1), 35–45.
- Li, B., Hong, J., Yan, S. & Liu, Z. (2013), ‘Multidiscipline topology optimization of stiffened plate/shell structures inspired by growth mechanisms of leaf veins in nature’, *Mathematical Problems in Engineering* **2013**.
- Li, H., Lo, K.-Y., Leung, M.-K., Fu, C.-W. et al. (2008), ‘Dual poisson-disk tiling: An efficient method for distributing features on arbitrary surfaces’, *IEEE Transactions on Visualization & Computer Graphics* (5), 982–998.
- Li, L.-y., Bettess, P., Bull, J. W. & Bond, T. J. (1997), ‘Adaptive finite element analysis of stiffened shells’, *Advances in Engineering Software* **28**(8), 501–507.
- Li, Y., Liu, Y. & Wang, W. (2015), ‘Planar hexagonal meshing for architecture’, *IEEE transactions on visualization and computer graphics* **21**(1), 95–106.

- Liu, Y., Pottmann, H., Wallner, J., Yang, Y.-L. & Wang, W. (2006), Geometric modeling with conical meshes and developable surfaces, *in* ‘ACM transactions on graphics (TOG)’, Vol. 25, ACM, pp. 681–689.
- Liu, Y. & Shimoda, M. (2014), ‘Parameter-free optimum design method of stiffeners on thin-walled structures’, *Structural and Multidisciplinary Optimization* **49**(1), 39–47.
- Liu, Y., Xu, W., Wang, J., Zhu, L., Guo, B., Chen, F. & Wang, G. (2011), ‘General planar quadrilateral mesh design using conjugate direction field’, *ACM Trans. Graph.* **30**(6), 140:1–140:10.
- Logan, D. L. (2011), *A first course in the finite element method*, Cengage Learning.
- Lu, L., Chen, B., Sharf, A., Zhao, H., Wei, Y., Fan, Q., Chen, X., Savoye, Y., Tu, C. & Cohen-Or, D. (2014), ‘Build-to-last: strength to weight 3d printed objects’, *ACM Transactions on Graphics* **33**(4), 1–10.
URL: <http://dl.acm.org/citation.cfm?doid=2601097.2601168>
- Lévy, B., Petitjean, S., Ray, N. & Maillot, J. (2002), Least squares conformal maps for automatic texture atlas generation, *in* ‘ACM transactions on graphics (TOG)’, Vol. 21, ACM, pp. 362–371.
- Melosh, R. J. (1963), ‘Basis for derivation of matrices for the direct stiffness method’, *AIAA Journal* **1**(7), 1631–1637.
- Michell, A. G. M. (1904), ‘Lviii. the limits of economy of material in frame-structures’, *The London, Edinburgh, and Dublin Philosophical Magazine and Journal of Science* **8**(47), 589–597.
- Mukhopadhyay, M. & Satsangi, S. (1984), ‘Isoparametric Stiffened Plate Bending Element For The Analysis Of Ships’structures’, *Royal Institution of Naval Architects Transactions* **126**, 144–151.
- Nguyen-Thoi, T., Bui-Xuan, T., Phung-Van, P., Nguyen-Xuan, H. & Ngo-Thanh, P. (2013), ‘Static, free vibration and buckling analyses of stiffened plates by CS-FEM-DSG3 using triangular elements’, *Computers & Structures* **125**, 100 – 113.
URL: <http://www.sciencedirect.com/science/article/pii/S0045794913001582>
- Nocedal, J. & Wright, S. (2006), *Numerical optimization*, Springer Science & Business Media.
- Ojeda, R., Gangadhara Prusty, B., Lawrence, N. & Thomas, G. (2007), ‘A new approach for the large deflection finite element analysis of isotropic and composite plates with arbitrary orientated stiffeners’, *Finite Elements in Analysis and Design* **43**(13), 989–1002.
URL: <http://linkinghub.elsevier.com/retrieve/pii/S0168874X07000807>

- Ortega, J. M. & Rheinboldt, W. C. (1970), *Iterative solution of nonlinear equations in several variables*, Vol. 30, Siam.
- Panozzo, D., Puppo, E., Tarini, M. & Sorkine-Hornung, O. (2014), ‘Frame fields: Anisotropic and non-orthogonal cross fields’, *ACM Transactions on Graphics (TOG)* **33**(4), 134.
- Paris, J., Navarrina, F., Colominas, I. & Casteleiro, M. (2010), ‘Stress constraints sensitivity analysis in structural topology optimization’, *Computer Methods in Applied Mechanics and Engineering* **199**(33-36), 2110–2122.
- Peng, C.-H., Zhang, E., Kobayashi, Y. & Wonka, P. (2011), ‘Connectivity editing for quadrilateral meshes’, *ACM Trans. Graph.* **30**(6), 141:1–141:12.
- Pietroni, N., Tonelli, D., Puppo, E., Froli, M., Scopigno, R. & Cignoni, P. (2014), ‘Voronoi Grid-Shell Structures’, *arXiv:1408.6591 [cs]*. arXiv: 1408.6591.
URL: <http://arxiv.org/abs/1408.6591>
- Pietroni, N., Tonelli, D., Puppo, E., Froli, M., Scopigno, R. & Cignoni, P. (2015), ‘Statics aware grid shells’, *Computer Graphics Forum* **34**(2), 627–641.
URL: <http://doi.wiley.com/10.1111/cgf.12590>
- Pirazzi, C., Weinand, Y. & others (2006), Geodesic lines on free-form surfaces: optimized grids for timber rib shells, in ‘Proc. World Conference on Timber Engineering’, Vol. 7, p. 595.
- Pottmann, H., Jiang, C., Höbinger, M., Wang, J., Bompas, P. & Wallner, J. (2015), ‘Cell packing structures’, *Computer-Aided Design* **60**, 70–83.
URL: <https://linkinghub.elsevier.com/retrieve/pii/S0010448514000426>
- Pottmann, H., Liu, Y., Wallner, J., Bobenko, A. & Wang, W. (2007), ‘Geometry of multi-layer freeform structures for architecture’, *ACM Transactions on Graphics* **26**(99), 65.
URL: <http://portal.acm.org/citation.cfm?doid=1276377.1276458>
- Pottmann, H., Schiftner, A., Bo, P., Schmiedhofer, H., Wang, W., Baldassini, N. & Wallner, J. (2008), ‘Freeform surfaces from single curved panels’, *ACM Transactions on Graphics (TOG)* **27**(3), 76.
- Prusty, B. G. (2003), ‘Linear static analysis of composite hat-stiffened laminated shells using finite elements’, *Finite Elements in Analysis and Design* p. 14.
- Prusty, B. G. & Satsangi, S. (2001), ‘Analysis of stiffened shell for ships and ocean structures by finite element method’, *Ocean Engineering* **28**(6), 621–638.
- Prévost, R., Whiting, E., Lefebvre, S. & Sorkine-Hornung, O. (2013), ‘Make it stand: balancing shapes for 3d fabrication’, *ACM Transactions on Graphics* **32**(4), 1.
URL: <http://dl.acm.org/citation.cfm?doid=2461912.2461957>

- Rao, D. V., Sheikh, A. H. & Mukhopadhyay, M. (1993), ‘A finite element large displacement analysis of stiffened plates’, *Computers & structures* **47**(6), 987–993.
URL: <http://www.sciencedirect.com/science/article/pii/004579499390303U>
- Rosin, P. L. (2000), ‘Fitting superellipses’, *IEEE Transactions on Pattern Analysis & Machine Intelligence* **22**(7), 726–732.
- Samanta, A. & Mukhopadhyay, M. (1998), ‘Finite element static analysis of stiffened shells’, *Applied Mechanics and Engineering* **3**(1), 55–87.
- Samanta, A. & Mukhopadhyay, M. (1999), ‘Finite element large deflection static analysis of shallow and deep stiffened shells’, *Finite elements in analysis and design* **33**(3), 187–208.
URL: <http://www.sciencedirect.com/science/article/pii/S0168874X99000220>
- Samanta, A. & Mukhopadhyay, M. (2004), ‘Free vibration analysis of stiffened shells by the finite element technique’, *European Journal of Mechanics - A/Solids* **23**(1), 159–179.
URL: <http://linkinghub.elsevier.com/retrieve/pii/S0997753803001281>
- Satsangi, S. & Ray, C. (1998), ‘Structural analysis of ships’ stiffened plate panels in bending’, *International shipbuilding progress* **45**(442), 181–195.
- Schiftner, A. & Balzer, J. (2010), ‘Statics-sensitive layout of planar quadrilateral meshes’, *Advances in Architectural Geometry 2010* pp. 221–236.
- Schiftner, A., Höbinger, M., Wallner, J. & Pottmann, H. (2009), ‘Packing circles and spheres on surfaces’, *ACM Trans. Graph.* **28**(5), 139:1–139:8.
- Schober, H. & Kuerschner, K. (2005), ‘Meraviglioso’, *Civil Engineering Magazine Archive* **75**(12), 36–43.
URL: <https://ascelibrary.org/doi/abs/10.1061/cieag.0000049>
- Simplify3D (2019), ‘Filament Properties Table’.
URL: <https://www.simplify3d.com/support/materials-guide/properties-table/>
- Sokół, T. (2011), ‘A 99 line code for discretized michell truss optimization written in mathematica’, *Structural and Multidisciplinary Optimization* **43**(2), 181–190.
- Srinivasan, R. S. & Ramachandran, S. V. (1977), ‘Linear and nonlinear analysis of stiffened plates’, *International Journal of Solids and Structures* **13**(10), 897–912.
URL: <http://www.sciencedirect.com/science/article/pii/0020768377900038>
- Srivastava, A., Datta, P. & Sheikh, A. (2003), ‘Buckling and vibration of stiffened plates subjected to partial edge loading’, *International Journal of Mechanical Sciences* **45**(1), 73–93.
URL: <http://linkinghub.elsevier.com/retrieve/pii/S0020740303000389>

- Stava, O., Vanek, J., Benes, B., Carr, N. & Měch, R. (2012), ‘Stress relief: improving structural strength of 3d printable objects’, *ACM Transactions on Graphics* **31**(4), 1–11.
- Su, L., Zhu, S.-l., Xiao, N. & Gao, B.-q. (2014), ‘An automatic grid generation approach over free-form surface for architectural design’, *Journal of Central South University* **21**(6), 2444–2453.
- Szczepanik, M. & Burczyński, T. (2012), ‘Swarm optimization of stiffeners locations in 2-d structures’, *Bulletin of the Polish Academy of Sciences: Technical Sciences* **60**(2), 241–246.
- Tam, K.-M. M., Coleman, J. R., Fine, N. W. & Mueller, C. T. (2016), Robotics-enabled stress line additive manufacturing, in ‘Robotic Fabrication in Architecture, Art and Design 2016’, Springer, pp. 350–361.
- Tam, K.-M. M., Mueller, C. T., Coleman, J. R. & Fine, N. W. (2016), ‘Stress line additive manufacturing (slam) for 2.5-d shells’, *Journal of the International Association for Shell and Spatial Structures (J. IASS)* **57**(4).
- Tang, C., Sun, X., Gomes, A., Wallner, J. & Pottmann, H. (2014), ‘Form-finding with polyhedral meshes made simple’, *ACM Trans. Graph.* **33**(4), 70:1–70:9.
- Telea, A. & Jalba, A. (2011), Voxel-based assessment of printability of 3d shapes, in ‘International Symposium on Mathematical Morphology and Its Applications to Signal and Image Processing’, Springer, pp. 393–404.
- Thompson, P. & Bettess, P. (1991), ‘Analysis of reinforced openings in ring stiffened shells using integrally stiffened shell elements’.
- Thompson, P., Bettess, P. & Caldwell, J. (1988), ‘An isoparametric eccentrically stiffened plate bending element’, *Engineering Computations* **5**(2), 110–116.
URL: <http://www.emeraldinsight.com/doi/10.1108/eb023728>
- Timoshenko, S. & Goodier, J. (1970), *Theory of Elasticity*, 3 edn, McGraw-Hill.
- Turner, M. J. (1956), ‘Stiffness and deflection analysis of complex structures’, *journal of the Aeronautical Sciences* **23**(9), 805–823.
- Umetani, N. & Schmidt, R. (2013), Cross-sectional structural analysis for 3d printing optimization., in ‘SIGGRAPH Asia Technical Briefs’, pp. 5–1.
URL: <https://pdfs.semanticscholar.org/f68c/aa0602d6ce2c3755f7df09569904eb2218eb.pdf>
- Ventsel, E. & Krauthammer, T. (2001), *Thin plates and shells: theory, analysis, and applications*, CRC press.
- Voronoi, G. (1908), ‘Nouvelles applications des paramètres continus à la théorie des formes quadratiques. Deuxième mémoire. Recherches sur les paralléloèdres primitifs.’, *Journal für die reine und angewandte Mathematik* **134**, 198–287.
URL: <http://eudml.org/doc/149291>

- Vouga, E., Höbinger, M., Wallner, J. & Pottmann, H. (2012), ‘Design of self-supporting surfaces’, *ACM Transactions on Graphics (TOG)* **31**(4), 87.
- Vörös, G. M. (2007), ‘Finite element analysis of stiffened plates’, *Periodica Polytechnica. Engineering. Mechanical Engineering* **51**(2), 105.
- Wang, B., Tian, K., Hao, P., Cai, Y., Li, Y. & Sun, Y. (2015), ‘Hybrid analysis and optimization of hierarchical stiffened plates based on asymptotic homogenization method’, *Composite Structures* **132**, 136 – 147.
URL: <http://www.sciencedirect.com/science/article/pii/S0263822315003773>
- Wang, D., Abdalla, M. M. & Zhang, W. (2017), ‘Buckling optimization design of curved stiffeners for grid-stiffened composite structures’, *Composite Structures* **159**, 656–666.
- Wang, W., Wang, T. Y., Yang, Z., Liu, L., Tong, X., Tong, W., Deng, J., Chen, F. & Liu, X. (2013), ‘Cost-effective printing of 3d objects with skin-frame structures’, *ACM Transactions on Graphics* **32**(6), 1–10.
URL: <http://dl.acm.org/citation.cfm?doid=2508363.2508382>
- Wilson, S. (1990), ‘A new face of aerospace honeycomb’, *Materials & Design* **11**(6), 323–326.
- Wu, J., Aage, N., Westermann, R. & Sigmund, O. (2017), ‘Infill optimization for additive manufacturing—approaching bone-like porous structures’, *IEEE Transactions on Visualization and Computer Graphics* .
- Yamaura, K., Tada, M., Tanigami, T. & Matsuzawa, S. (1986), ‘Mechanical properties of films of poly(vinyl alcohol) derived from vinyl trifluoroacetate’, *Journal of Applied Polymer Science* **31**(2), 493–500.
URL: <https://onlinelibrary.wiley.com/doi/abs/10.1002/app.1986.070310216>
- Yang, Y.-L., Yang, Y.-J., Pottmann, H. & Mitra, N. J. (2011), ‘Shape space exploration of constrained meshes’, *ACM Trans. Graph.* **30**(6), 124:1–124:12.
- Zadravec, M., Schiftner, A. & Wallner, J. (2010), ‘Designing quad-dominant meshes with planar faces’, *Computer Graphics Forum* **29**(5), 1671–1679. Proc. Symp. Geometry Processing.
- Zengjie, G. & Wanji, C. (2003), ‘Refined triangular discrete Mindlin flat shell elements’, *Computational Mechanics* **33**(1), 52–60.
URL: <http://link.springer.com/10.1007/s00466-003-0499-z>
- Zhao, H., Xu, W., Zhou, K., Yang, Y., Jin, X. & Wu, H. (2016), ‘Stress-Constrained Thickness Optimization for Shell Object Fabrication: Stress-Constrained Thickness Optimization for Shell Object Fabrication’, *Computer Graphics Forum* .
URL: <http://doi.wiley.com/10.1111/cgf.12986>

Zhou, Q., Panetta, J. & Zorin, D. (2013), 'Worst-case structural analysis', *ACM Transactions on Graphics* **32**(4), 1.

URL: <http://dl.acm.org/citation.cfm?doid=2461912.2461967>

Zienkiewicz, O. C. & Taylor, R. L. (1991), *The finite element method*, 4th ed edn, London ; New York : McGraw-Hill.